Modeling of the plasmon resonance of metallic nanopaticles embedded in liquid crystal

Huan Wang

Thèse
de doctorat
de l'UTT

Huan WANG

Modélisation de l'accordabilité de la résonance plasmon de particules métalliques par des cristaux liquides

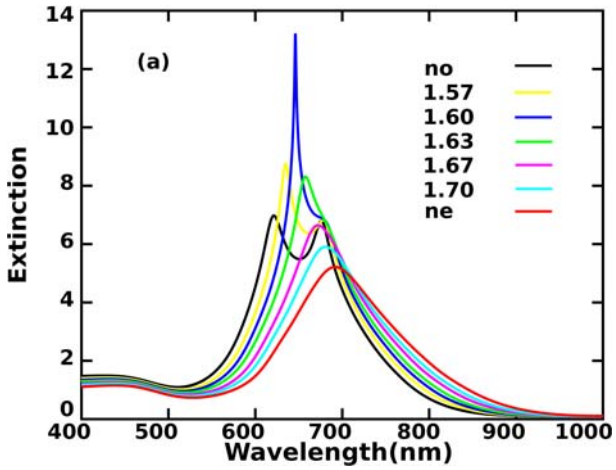

Spécialité :
Optique et Nanotechnologies

2014TROY0004

Année 2014

utt
université de technologie
Troyes

THESE

pour l'obtention du grade de

DOCTEUR de l'UNIVERSITE DE TECHNOLOGIE DE TROYES

Spécialité : OPTIQUE ET NANOTECHNOLOGIES

présentée et soutenue par

Huan WANG

le 7 février 2014

Modélisation de l'accordabilité de la résonance plasmon de particules métalliques par des cristaux liquides

JURY

M. R. BACHELOT	PROFESSEUR DES UNIVERSITES	Président
M. R. CAPUTO	RICERCATORE SCIENTIFICO DI RUOLO	Examinateur
M. N. FELIDJ	PROFESSEUR DES UNIVERSITES	Rapporteur
Mme E. LACAZE	DIRECTRICE DE RECHERCHE CNRS	Rapporteur
M. A. VIAL	PROFESSEUR UTT	Directeur de thèse

Acknowledgement

I would like to express my gratitude to all those who helped me during the writing of this thesis. My deepest gratitude goes first and foremost to Professor Alexandre VIAL, my supervisor who led me into the world of research, for his constant encouragement and guidance. He has walked me through all the stages of the writing of this thesis. Without his consistent and illuminating instruction, this thesis could not have reached its present form.

Second, I would like to express my heartfelt gratitude to Professor Renaud BACHELOT, who opens my eyes to the research. I am also greatly indebted to the PhD students at Laboratory of Nanotechnology, Instrumentation and Optics : Kun JIA, Loïc Le Cunff, and Xuan ZHOU, etc. who have instructed and helped me a lot in the past three years.

Last my thanks would go to my beloved family for their loving considerations and great confidence in me all through these years. I also owe my sincere gratitude to my friends and my fellow classmates who gave me their help and time in listening to me and helping me work out my problems during the difficult course of the thesis.

WANG Huan

CONTENTS

LIST OF TABLES

LIST OF FIGURES

Chapitre I

Introduction

I.1 Background

Over the past decades, with the increasing demand for faster, smaller and more highly integrated optical and electronic devices, accompanying with extremely sensitive detectors for biomedical and environmental applications, Nano-optics become a hot and rapidly evolving field.

The development of nano-optics is built on the achievements of classical optics. It is known that optical resolution can not be improved infinitely, the resolution theory was described by Abbe in 1873 [1] and Rayleigh in 1879 [2]. Different techniques were invented in order to stretch the diffraction limit, such as confocal microscopy, multi-photon microscopy and coherent anti-Stokes Raman scattering microscopy. Nevertheless, near-field optical microscopy provides a different method for spatial resolution in optical imaging. It is applied to image the features near the surface of a sample. For example, atomic force microscopy could figure out the complimentary information about the surface topology. Furthermore, scanning probe microscopy, photon scanning tunneling microscope and the near-field reflection microscope could state a confined photon flux between probe and sample. The photon flux must have a minimum intensity in order to be detectable. It is in some extent contradictory and a compromise between light confinement and light throughput has to be found.

In nano-optics, one of the key questions is how material structures have to be shaped to actually realize the theoretically possible field confinement. Another key issue is the question of what are the physical consequences of the presence of exponentially decaying and strongly confined fields [3].

Plasmonics is the way to concentrate and channel light using sub-wavelength struc-

tures. It is widely recognized after the pioneering work of Ritchie in the 1957 [4]. Surface plasmonics (SPs) are electromagnetic waves which propagate along the surface of conductor, the trapped light waves on the surface stem from the interactions between incident light and the electrons of the conductor [5]. This interaction can give rise to surface charge-density oscillations which can strongly enhance optical near-fields. In similarity, if the electrons are confined in a small particle, for example, a small metallic particles illuminated with electromagnetic waves, when the incident wave frequency is resonant with the collective oscillation of the electron gas, the SPs modes will appear at the particles' surface. Owing to the negative real part of the dielectric constant of noble metals, the SPs modes are localized to the particles surface, it is called localized surface plasmons (LSPs), such surface excitations are bound to geometries of metallic particles [6; 7]. The frequency of an LSP can be determined by a treatment neglecting retardation effects, electrostatic approximation is valid if the geometries size(a)is small compared with the LSP wavelength(λ). The dispersion relation for the LSPs frequencies is given by $\epsilon(\omega) = -\epsilon_0(\frac{l+1}{l})$ considering a metallic sphere embedded in a medium of dielectric constantϵ_0, where l is an integer (1, 2, 3, 4.....). For small spheres ($a \ll \lambda$), only the dipole-active excitation (l =1) dominates, with increasing the size of the sphere, higher multi-poles make more and more important contributions. If the size is big enough, as a result, the LSP frequency approaches that of a surface plasmon at a planar dielectric-metal interface [8].

The boundedness of LSPs results in a significant electromagnetic field enhancement at small metallic particles owing to the small volume of the LSPs modes [9]. This effect contributes to many phenomena, for example, light emission from STM tunnel junctions, second-harmonic generation and surface enhanced Raman scattering and the applications in apertureless scanning NF microscopy [10; 11; 12; 13]. The effects associated with LSPs also could be applied for low-light intensity active photonic devices [14].

Owing to the optical properties of noble nano-particles and their potential applications, nano-optics field has attracted many researchers' attentions. Both in the theory and experiments, the facts have been verified. They are that the Localized surface plasmon resonance frequency will be influenced by the size, shape and physical properties of metal nano-particles, as well as the period of the nano-particles array [15; 16; 17; 18; 19].

The materials surrounding the nano-particles can also modify the resonance position of LSPs. Furthermore, changing the dielectric properties in the vicinity of the noble nano-particles leads to a change of LSPR positions. As a result, nematic liquid crystals (LCs) have been explored to control the surface plasmon polarization and subsequent optical transmission [20; 21; 22]. So far, many researchers mixed LCs with metallic nano-particles. Indeed, by applying an external electric field, the environment of the particle can be modified, leading to a LSPR shift. Using LCs in conjunction with gold gratings or nano-particles, for example gold nanorods, gold nanodots and nanodisks, gold dimer, and nanohole arrays have been reported experimentally [21; 23; 24; 25; 22; 26].

Localized surface plasmon resonance (LSPR), as a result of collective oscillations of nano-particles' conduction band electrons, could be understand by Mie theory for a sphere, which was first described in 1908. However, for more complex geometries (e.g. cylinders, cubes, triangular prisms, etc.), more advanced electrodynamic numerical methods should be employed in order to correctly describe optical properties of metal nano-particles. Finite-difference time-domain method (FDTD) can give the effective numerical solution of electromagnetic propagation described by Maxwell equations. It was firstly introduced by Yee in 1966 [27], and the main algorithm is based on central differences and the Yee cell. This method is widely used in nano-technology and other electromagnetic communication.

I.2 Key issues in this thesis

In my thesis, four important issues should be completed, they are described as follows.

- Investigating the models of gold and the dispersive properties as well as the anchoring effects of nematic LCs.
- Building the structure.
- Writing the programs.
- Analyzing the results.

I.3 The problems studied in this thesis

In this work, we try to design a kind of structure that could provide the biggest LSPR shift. Herein, double resonances are observed clearly using a special structure. Furthermore, we have investigated the SERS gains responding the structures. These three problems have been listed :

- The LSPR shift of gold nano-particles, embedded in a LC cell, are investigated as a function the optical axis orientation of the LC molecules by taking anchoring effects into account.
- Double resonances, localized surface plasmon and cavity mode resonance peak positions, are studied using an ordered array of gold cylinder with elliptic basis embedded in a nematic liquid crystal (LC)
- Surface-Enhanced Raman Scattering(SERS) gain (G_{SERS}) is described using FDTD method.

I.4 The contribution of the thesis

By investigating the LSPR shift of gold nanostructures embedded in a LC cell, we have shown that anchoring effect, at the interfaces of LC cell and glass substrate, strongly reduce the LSPR tunability by comparison with the case of an isotropic medium or with LC with perfect alignment, but that modifications to the nano-structures shape and array or LC height could efficiently compensate it.

Furthermore, the double resonance are studied by electric distribution maps. Finally, the SERS gain is computed in the whole LCs cell using different Raman bands, which exhibits a double peak also. For two excitation wavelength (590 nm and 632.8 nm), SERS gains are compared. We anticipate that the work will offer an aid for the design and the fabrication of nano-sensors.

I.5 Conclusion

In this thesis, we firstly introduce the phase of matter and the classification of Liquid crystal. Physical properties as well as optics and electric field effects of nematic LCs will be described in chapter 2. Subsequently, in chapter 3, the regime of localized surface plasmon resonance is going to be presented, quasi-static approximation and LSPR damping are explained in detail ; one of the main applications of the LSPR, surface enhanced raman scattering, is divided from other applications, for example, sensors and photonic device. Furthermore, the numerical method we have used, finite-difference time domain, is introduced in the chapter 4. Herein, Yee algorithm and absorbing boundary conditions are introduced, the common models using for noble metal are illustrated also ; in addition, the techniques, how to deal with the dispersive property of gold and anisotropic character of nematic liquid crystals, are exhibited. In chapter 5, the localized surface plasmon resonance (LSPR) peak position of an ordered gold nano-particles array embedded in a nematic liquid crystal (LC) media is investigated using Finite-Difference Time Domain (FDTD) method. The influence of the anchoring effects between nematic LC molecules and glass substrate on the shift of LSPR wavelength is taken into account, and results are compared with the case of a perfect alignment of the LC molecules. The localized surface plasmon resonance positions and the Surface-Enhanced Raman Scattering (SERS) gain (G_{SERS}) of an ordered array of gold nano-cylinders with elliptic basis, embedded in a nematic liquid crystal (LC) media, are investigated also. Herein, structures are designed so that two resonances occur. The influence of the anchoring effects on the shift of the double resonance wavelengths is considered, and results are compared not only with the case of a perfect alignment of the LC molecules but also an isotropic material.

Chapitre II

Liquid Crystal

II.1 Introduction

Liquid crystal, existing in molecule level, has been a hot topic due to its anisotropic property and the switched orientation. Liquid crystal display(LCD) has been the main technology for large TV, laptops, cellular phones. A new field of nano-photonic LC-based is emerging for variety of non-display applications [28; 29; 30], such as the tuning of plasmonic nano-structures and nano-porous material.

We will present the phase of matter, classification of Liquid crystal phase, the physical and optical properties of nematic LCs separately.

II.1.1 Phase of matter

In physics, a phase is a thermodynamic system, throughout which all physical characters of a material are virtually uniform [31]. Physical characters include density, index of refraction, magnetization and chemical composition etc. Simply, a phase is a region of material that is uniform in chemicals, distinct in physics, and (often) mechanically separable.

Normally, states of matter can be observed by four phases. Such as solid, liquid, gas, plasma (See Fig. II.1). In addition, under some special cases, other phases exist also in certain types of materials, for example, supercritical fluids, degenerate gases, Bose-Einstein condensates etc.

The phase of matter can be inversed if the surrounding phenomenon varies, it usually either releases or takes up energy. Combining Fig. II.1, water for instance,

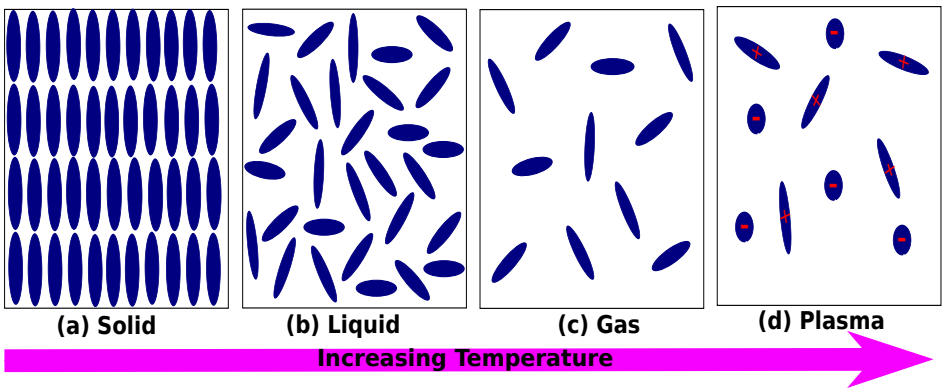

Fig. II.1 – Phases of matter.

when the temperature increases to 100^oC, water evaporates and becomes gas, the kinetic energy expends as the evaporating molecules escape the attractive forces of the liquid. Furthermore, the temperature increases up to 1000^oC, water molecules can become ionized as electrons which are disassociated from their respective nuclei ; this phase is named as plasma. The reverse process, when the temperature decreases to below 0^oC, water become to solid ice.

II.1.2 Liquid crystals

Mesophases are used to describe the state of matter between solid and liquid phase. Liquid crystal is matter in the state which has the properties of both liquid(fluidity, formation and coalescence of droplets, etc.) and solid crystal(optical anisotropy, electromagnetic properties, periodic arrangement of molecules in one spatial direction, etc.).

Examples of liquid crystals can be found both in the natural world and in technological applications. Most contemporary electronic displays use liquid crystals. Lyotropic liquid-crystalline phases are abundant in living systems. For example, many proteins and cell membranes are LCs. Other well-known LC examples are solutions of soap and various related detergents, as well as the tobacco mosaic virus.

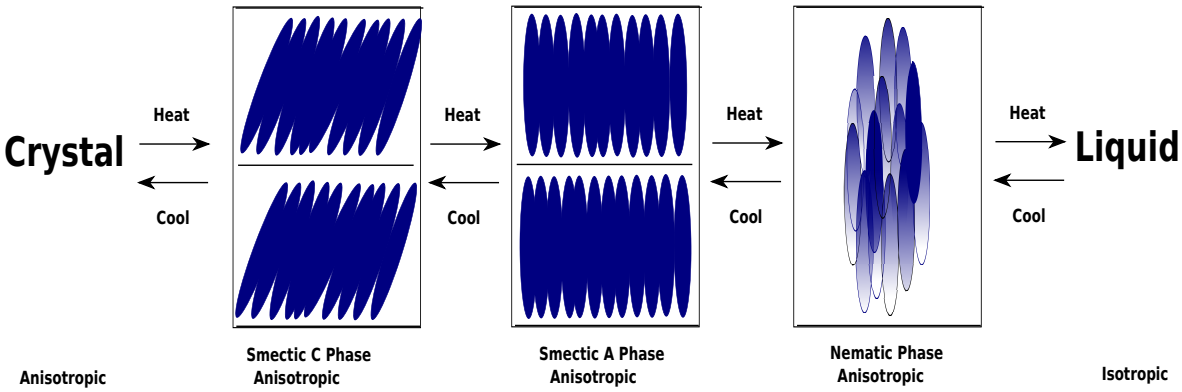

Fig. II.2 – Phases of LCs.

II.2 Classification of LCS

LC molecules show only long-range orientation order but not long-range position order. Based on the degree of positional disorder of LCs, three types of phases are introduced(See Fig. II.2), nematic phase, smectic A phase and smectic C phase. The properties of these three phases will be given in the next section.

According to the methods of phase transition, Liquid crystals(LCs) can be divided into thermotropic, lyotropic and metallotropic phases.

- Thermotropic LCs are formed by certain organic substances when the melting thermotropic threshold is met ; when another thermotropic threshold is achieved, they become "normal" liquids.
- Lyotropic LCs exhibit phase transitions of organic substances as a function of both temperature and concentration of the LC molecules in a solvent.
- Metallotropic LCs are mixtures of organic and inorganic molecules, their phases are affected not only by temperature and concentration, but also by the mixture ratio.

In terms of broad classifications, liquid crystal molecules are generally further distinguished according to the shape of constituent molecules as illustrated in Fig. II.3. They are, thermotropic LCs for instance, polyphilic phase, discotic phase, Bowl-type phase.

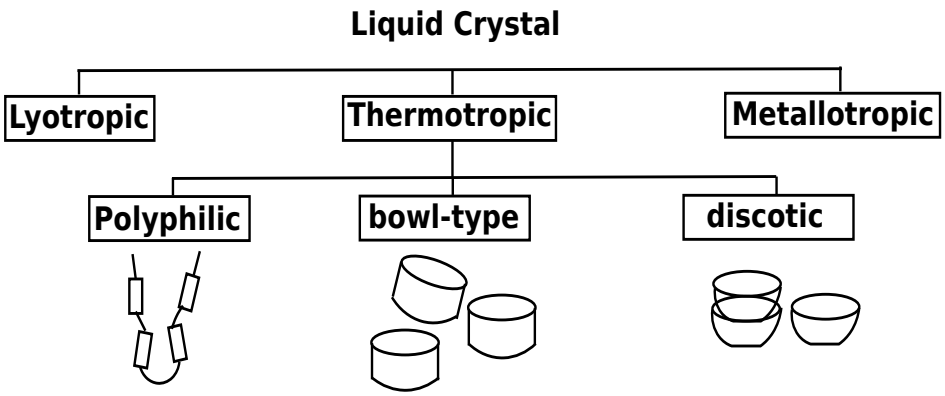

Fig. II.3 – Classification of LCs.

II.2.1 Nematic phase

The nematic phase owns the property of long-range orientation order. This means that the long axes of all the molecules tend to align along one direction. And in the local domain, the preferred direction may be varied, which happens also in the unstrained nematic. The orientation and dynamics of the preferred axes of the molecules induce to some interesting phenomenons.

* We assume the long planar molecule as ellipse (See Fig. II.4(c), (d)), the unit vector n is defined as its local orientation. No long-range order exists at the position of one molecule, but a certain amount of short-range order may appear in local domain, just like molecules in ordinary liquid. The molecules are able to rotate around their long axes and no preferential arrangement of the two ends of the molecules appears. Hence, in physics, there is no polarity, n=-n.
* Optically a nematic behaves as a uniaxial material with a center of symmetry.
* Translational symmetry. Owing to the possibility of the translational motion of the molecules in any direction, the density of molecules is not dependent on the coordinates. It responds to the fluidity of liquid crystals.
* The characteristic microscopic texture with crossed polarizers(See Fig. II.4(a)). The point disclinations and the nuclei of divergent threads can be observed in the texture.

Normally, nematics are non-polarity rod-like organic molecules on the order of 20 Angstroms in length. At least, polar nematic phases have not been found yet [32].

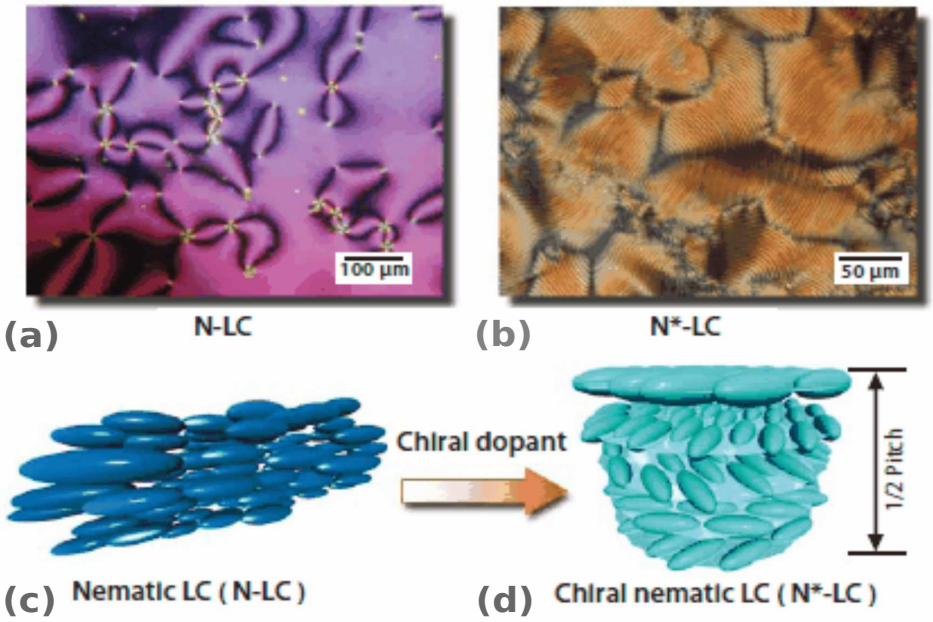

Fig. II.4 – Nematic phases (left) and chiral nematic phase (right). An illustration of the orientation of the molecules (below), and an optical micrograph of the schlieren texture (above) [33].

II.2.2 Chiral nematics (Cholesteric)

Cholesteric is a kind of phase which are naturally materials with a preference for twisted molecular stacking. However, the equivalent structure is also achieved using nematics without intrinsic chiral twist. By adding small concentration of chiral dopant molecules, nematic LCs will achieve chiral properties. The rotation of the director of chiral nematics and the texture with optical polarising microscopy are given in Fig. II.4(d), (b). The twisting power and the pitch could be modified when we vary the concentrations of dopant molecules.

Owing to no layer structure and local order identified in nematic phase, pitch is defined to describe the length scale of this phase, that is the distance of the director rotated an angle of 2π. Nevertheless, the no-polar property(n=-n) implies the periodicity is only half the pitch. The pitch of the common nematics is of the order of several hundreds nanometers, when it is approximately equal to the wavelength of incident light, selective reflection can occur. The optic axis of chiral nematics is aligned along the helix axis, which is different from that of nematics. The chiral nematic liquid crystals has lots of useful optical properties that are not found in nematic phase.

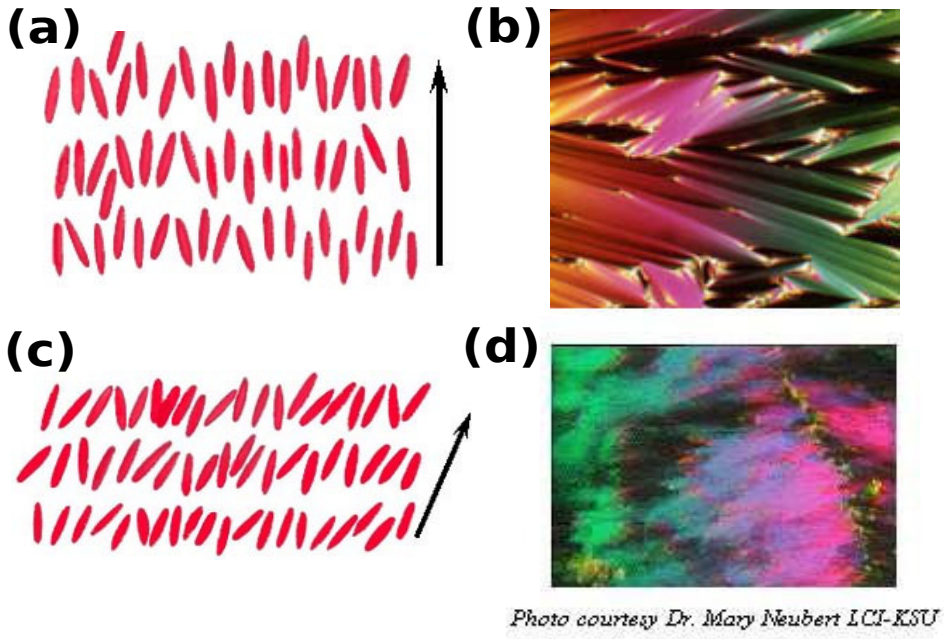

Fig. II.5 – Schematic of smectic-A and smectic-C.

II.2.3 Smectic LCs

Stratification is an important character of smectic phase, it is used to distinguish smectic phase from nematic phase. Smectics exhibit more degree of orientational order. Several different classes have been recognized to describe smectic phase, the two best know of them are Smectic A phase and Smectic C phase.

In Smetic A, the molecules are aligned perpendicular to the layer planes. No long-range order exists within one layer. And the layers are free to slide over one another. The schematic and a photo of the smectic A phase using polarizing microscope are presented in Fig. II.5 (a) and (b).

In Smectic C, the alignment of the molecules are at some arbitrary angle, which are not normal to the layers. Therefore, the phase has biaxial symmetry. The layers can slide over one another also. The structure and the typical textures formed by smectics C is described in Fig. II.5 (c) and (d).

In some smectic phases, the molecules are affected by the various layers above and below them [32]. Here we do not explain them in details.

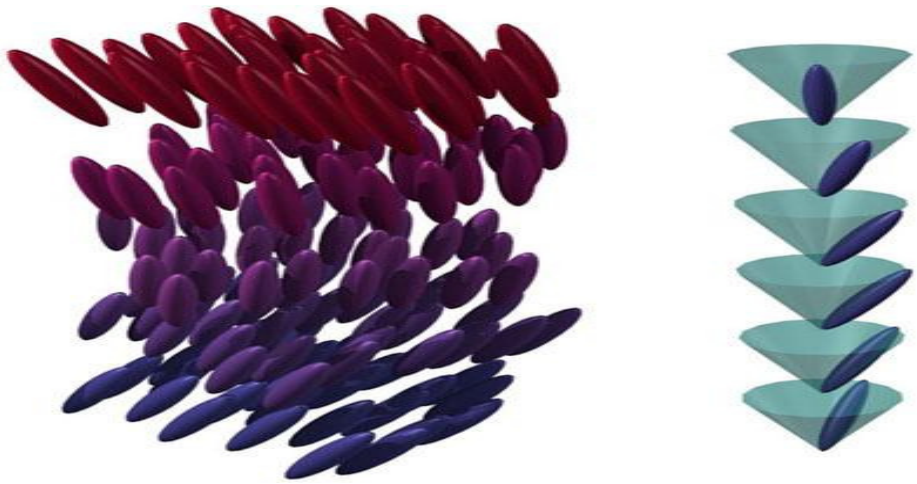

Fig. II.6 – Chiral smectic C phase. The director tilt of each layer precesses upwards around a circle.

II.2.4 Chiral smectic LCs

Helical smectic phases are also observed such as the chiral smectic C phase, which is similar to the chiral nematic phase. Within Chiral smectic phase, the molecules are tilted with an fixed angles which are different within the different layers according the helical axis.

Chiral Smectic C liquid crystals exhibit ferroelectric qualities and bistability, including fast switching speeds also. The schematic is given in Fig.II.6. In this Chapter, we mainly investigate nematic LCs. More informations could be found in the book Structure and Properties of Liquid Crystals written by Lev M. Blinov.

II.3 Physical properties of nematic LCs

II.3.1 Alignment of LC molecules and anchoring effects of nanostructured surfaces

The interaction between LCs and solid surfaces is studied owing to its importance on the behavior of LCs under the action of external fields. Alignment of LCs on solid surfaces depends not only on the chemical properties of the surface, but also on the geometrical structure on the nanoscale.

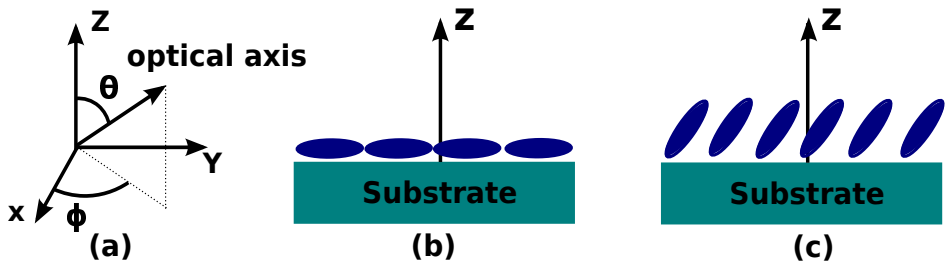

Fig. II.7 – Planar aligned nematic LCs under external applied electric voltage [26]. (a) Optical axis orientation of liquid crystals, (b) Side view of planar alignment parallel nematic LCs, (c) Side view of planar alignment tilted nematic LCs.

The anchoring energy is defined as the ability of anchoring to the boundaries of molecules, which has two parts.

a) Isotropic part : it is the surface tension.

b) Anisotropic part : it is influenced by the orientation of molecules.

θ is defined as the polar angle between z-coordinate and the orientation of liquid crystal molecules, ϕ is defined as the azimuth angle between x-coordinate and LC molecules orientation (See Fig. II.7). Thus, the surface anchoring energy consists of two parts (polar energy and azimuth energy) for any oriented nanostructure.

The surface anchoring energy is given by [34] :

$$F_a = F_0 + \Delta F_{ap} + \Delta F_{az}, \tag{II.1}$$

F_0 is constant energy when LCs are with free nematic surface (called "easy axis"), the orientation is described by θ_0 and ϕ_0. ΔF_{ap} responds to polar anchoring, ΔF_{az} responds to azimuthal anchoring, they are described by II.2.

$$\Delta F_{ap} = 0.5 W_{ap} sin^2(\theta - \theta_0); \quad \Delta F_{az} = 0.5 W_{az} sin^2(\phi - \phi_0) \tag{II.2}$$

W_{ap} and W_{az} are influenced by LC and substrate surface tensions.

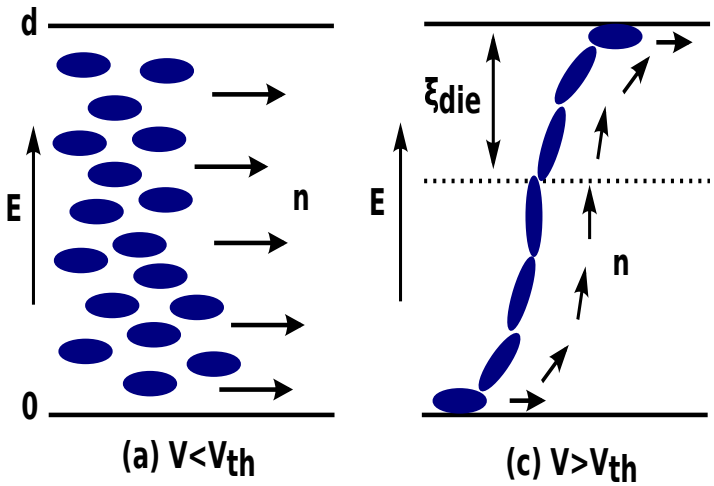

Fig. II.8 – Planar aligned nematic LCs under external applied electric voltage.

II.3.2 Alignment of molecules at the surface under the applied external field

The interaction at the interface between LC molecules and solid surface is the strongest, but decreases with the distance from the surface.

A planar aligned cell($\theta = pi/2$) for instance(see Fig. II.8), when the applied voltage is smaller than the threshold $V < V_{th}$, the cell maintains the planar alignment. when the applied voltage is bigger than threshold $V > V_{th}$, the molecules tend to align parallel to the applied external electric field direction. V_{th} is influenced by anchoring energy presented by Eq. II.1.

The molecules at the middle of the cell is affected strongly by the field owing to its far away from the interface so the anchoring torque influence them less. The molecules on the surface might orient toward the electric field direction, which depends on how strongly they are anchored to the surface. Therefore, the orientation of molecules is no longer parallel to the substrate and become distorted.

To investigate the strength of anchoring effect at the interface between the molecules and the substrate, we use the electric coherence length ξ_{die}, which is given as :

$$\xi_{die} = \frac{d}{\pi}\frac{V_{th}}{V}, \tag{II.3}$$

the electric coherence length ξ_{die} is used to describe the thickness near the surfaces,

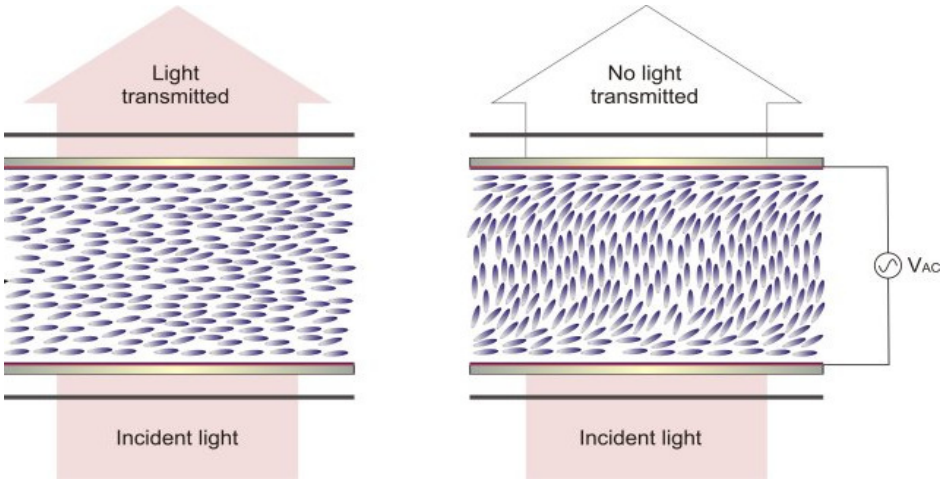

Fig. II.9 – Figures representing a liquid crystal cell acting as an intensity modulator when switching between a bright state (left) and a dark state (right) [37].

where the molecules are not parallel to the applied electric field.

Similarly, the magnetic coherence length is given as :

$$\xi_m = -\frac{d}{\pi}\frac{H_{th}}{H}, \tag{II.4}$$

where

H is the applied magnetic field,

H_{th} is the Frederick threshold field.

Owing to its strong influence on the optical characters of LC devices, this length could not be neglected. Hence, this layer will decrease with the applied field increases. For instance, if the thickness of molecules is $d = 10\mu m$, when applying a voltage 100 V, the electric coherence length $\xi_{die} \approx 30nm$; while if the applied voltage is 10 V, $\xi_{die} \approx 300nm$ [26].

For nematic LCs at different voltages, different phase modulations are achieved. Intensity modulation of transmitted light is easily achieved by simply placing a planar aligned liquid crystal cell between crossed polarisers, and modulating the applied voltage. See Fig. II.9(Further information will be find at http ://www-g.eng.cam.ac.uk/CMMPE/lcintro4.html)

II.4 Optical properties in nematic LCs

II.4.1 Extraordinary index of a birefringent layer of a dielectric ellipsoid

If an insulator is placed in the electric field, the stored electric energy density is described by g_{electr}, here the dielectric permittivity tensor is symmetric $\varepsilon_{ij} = \varepsilon_{ji}$. Normally, the tensor has six independent components, even for biaxial medium.

$$8\pi g_{electr} = \varepsilon_{x'x'}E_{x'}^2 + \varepsilon_{y'y'}E_{y'}^2 + \varepsilon_{z'z'}E_{z'}^2 + 2\varepsilon_{y'z'}E_{y'}E_{z'} + 2\varepsilon_{x'z'}E_{x'}E_{z'} + 2\varepsilon_{x'y'}E_{x'}E_{y'} \tag{II.5}$$

Eq. II.5 describe an ellipsoid arbitrary oriented with respect to any Cartesian frame [38]. If the principle axes of the ellipsoid are set along the coordinate axes, then the tensor becomes diagonal, and all the off-diagonal terms vanish.

$$8\pi g_{electr} = \varepsilon_{xx}E_x^2 + \varepsilon_{yy}E_y^2 + \varepsilon_{zz}E_z^2 \tag{II.6}$$

Eq. II.6 can be presented by the electric displacement vector components :

$$8\pi g_{electr} = \frac{D_x^2}{\varepsilon_{xx}} + \frac{D_y^2}{\varepsilon_{yy}} + \frac{D_z^2}{\varepsilon_{zz}} \tag{II.7}$$

We use space replacing vector r to substitute $\frac{D}{\sqrt{8\pi g_{electr}}}$, therefore the dielectric ellipsoid with three semi-axes equal to $\sqrt{\varepsilon_1}, \sqrt{\varepsilon_2}, \sqrt{\varepsilon_3}$ (Diagram in Fig. II.10)is expressed as :

$$\frac{x^2}{\varepsilon_1} + \frac{y^2}{\varepsilon_2} + \frac{z^2}{\varepsilon_3} = 1 \tag{II.8}$$

In this case, the electric permittivity in three semi-axes are $\varepsilon_1 = \varepsilon_{xx} \neq \varepsilon_2 = \varepsilon_{yy} \neq \varepsilon_3 = \varepsilon_{zz}$.

For a uniaxial phase(Nemetic LCs), at optical frequencies $\varepsilon = n^2$, "optical indicatrix" with semi-axes exactly equal to refraction indices n_1, n_2 and n_3 for the same

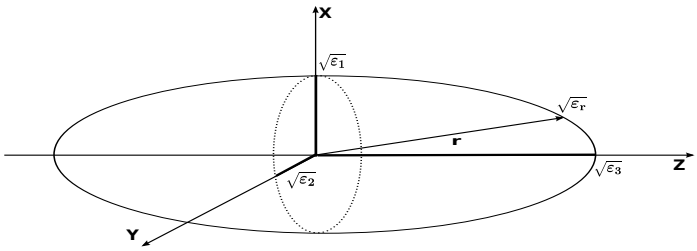

Fig. II.10 – Dielectric ellipsoid.

ellipsoid is given as :

$$\frac{x^2}{n_1^2} + \frac{y^2}{n_2^2} + \frac{z^2}{n_3^2} = 1 \tag{II.9}$$

Physically, electromagnetic waves with polarization vectors along x, y or z axes propagate with three different velocities $\frac{c}{n_1}$, $\frac{c}{n_2}$ and $\frac{c}{n_3}$. C is the light speed in vacuum.

If the uniaxial phases $n_1 = n_2 = n_\perp$ and $n_3 = n_\parallel$, there are two cases considering the ellipsoid cross-section in plane(n,k),Schematic is described in Fig. II.11 :

- When k is parallel to n and z, it corresponds to the normal incidence light illuminating onto LCs, which is homeotropically aligned. In this case, electromagnetic wave with any polarization propagates along the optical axis with the same velocity $c/n_\perp$, which is an ordinary ray.
- The angle between k and n is arbitrary, corresponding to the tilted orientation of LCs, the ordinary ray propagates with velocity c/n_0 with electric polarization vector $e \perp n$, which is independent on incidence angle. We will induce the extraordinary ray as a function of the tilt angle θ, considering the ellipsoid cross-section at the point P in Fig. II.11(a), the projection of the segment $n_e(\theta)$ on the semi-axes of the ellipse are :

$$\begin{aligned} X &= n_e(\theta) sin\theta, \\ Y &= 0, \\ Z &= n_e(\theta) cos\theta. \end{aligned} \tag{II.10}$$

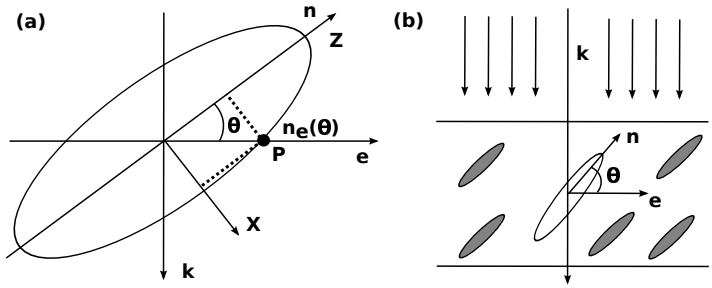

Fig. II.11 – Ellipse geometry for calculating the extraordinary refraction index.

From Eq. II.9, we can get :

$$\frac{n_e^2(\theta)sin^2\theta}{n_\perp^2} + \frac{n_e^2(\theta)cos^2\theta}{n_\parallel^2} = 1 \tag{II.11}$$

then, we get the refraction index for the extraordinary ray as a function of the tilt angle θ, it is given by :

$$n_e(\theta) = \frac{n_\parallel n_\perp}{\sqrt{n_\parallel^2 sin^2\theta + n_\perp^2 cos^2\theta}} \tag{II.12}$$

for the homeotropic orientation, $\theta = 0$ and $\theta_e(\theta) = n_\parallel$, for homegeneous planar alignment $\theta = \frac{\pi}{2}$, $\theta_e(\theta) = n_\perp$ [26].

II.4.2 Uniaxial anisotropic materials

For a general anisotropic dielectric substrate, when the optical axis lies either in the xz-plane, the relative permittivity tensor is given by :

$$\begin{pmatrix} \varepsilon_1 cos^2\theta + \varepsilon_2 sin^2\theta & 0 & (\varepsilon_1 - \varepsilon_2)cos\theta sin\theta \\ 0 & \varepsilon_1 & 0 \\ (\varepsilon_1 - \varepsilon_2)cos\theta sin\theta & 0 & \varepsilon_1 sin^2\theta + \varepsilon_2 cos^2\theta \end{pmatrix} \tag{II.13}$$

where ε_1 and ε_2 are the relative permittivities of uniaxial anisotroic dielectric.

For all uniaxial media, θ is the angle between the orientation and x-direction. Nematic LC E7 for instance, $\varepsilon_1 = n_o^2$, $\varepsilon_2 = n_e^2$, θ is the angle between the orientation of LC molecules and x-direction.

Whereas, if the optical axis is placed in the yz-plane, the relative permittivity tensor is given by :

$$\begin{pmatrix} \varepsilon_1 & 0 & 0 \\ 0 & \varepsilon_1 cos^2\phi + \varepsilon_2 sin^2\phi & (\varepsilon_1 - \varepsilon_2)cos\phi sin\phi \\ 0 & (\varepsilon_1 - \varepsilon_2)cos\phi sin\phi & \varepsilon_1 sin^2\phi + \varepsilon_2 cos^2\phi \end{pmatrix}, \tag{II.14}$$

where ϕ is the angle between the optical axis and y-direction [39].

This will be discussed further in the chapter 4 combined with the numerical method FDTD.

II.5 Conclusion

Owing to the all properties of LCs presented in this chapter, nematic LC will be linked to our plasmonic investigations, mainly based on its anisotropic properties and anchoring effects.

Liquid crystal is a perfect material for monitoring the optical response of plasmonic nano-structure. That creates amount of engineering application, nano-technology and biology for instance.

Chapitre III

Localized Surface Plasmon Resonance

III.1 Introduction

In this chapter, we will present the basic theory about localized surface plasmon. Localized surface plasmon resonance(LSPR) is a significant optical properties of metallic nano-particles, which can be enhanced when the incident wave frequency is resonant with the collective oscillation of the conduction electrons(see Fig. III.1). The size, shape, the periods of the metallic nano-particle arrays and the surrounding materials will influence the LSPR position and intensity.

Origination of the LSPR will be explained using cylinder. Quasi-static approximation, sphere and ellipsoidal particles for instance, are used to analyze this resonance phenomenon. We introduce LSPR damping also in this chapter, furthermore, the surface-enhanced Raman scattering is investigated. Lastly, the applications of LSPR are simply presented.

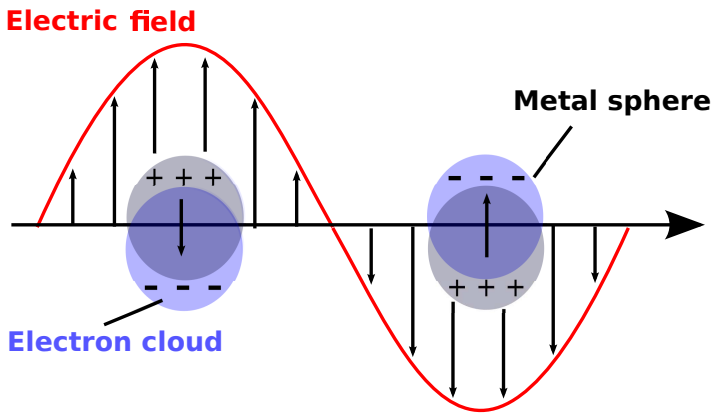

Fig. III.1 – Schematic of Localized surface plasmon resonance.

III.2 Quasi-Static Approximation

The interaction between a particle with size d and electromagnetic field can be investigated using the quasi-static approximation when $d \ll \lambda$, furthermore, the quasi-static approximation is suitable for the particle with dimensions that are less than 1% of the wavelength of incident wave in the surrounding medium [7].

In this regime, by assuming a particle in an electrostatic field, the harmonically oscillating electromagnetic field is time dependence and spacial independence over the particle volume. It can give quite well results by using the solution of the Laplace equation for the potential [40].

III.2.1 Quasi-static approximation for sphere particle

A small sphere with radius $a \ll \lambda$ for instance, under plane-wave illumination with $E(r,t) = E_0 e^{-i\omega t}$, an oscillating dipole moment is induced [41].

$$p(t) = \epsilon_0 \epsilon_d \alpha E_0 e^{-i\omega t}, \tag{III.1}$$

where $\alpha = 4\pi a^3 \dfrac{\epsilon_m - \epsilon_d}{\epsilon_m + 2\epsilon_d}$, and ϵ_m is the relative permittivity of particle, ϵ_d is the relative permittivity of surrounding medium,

The polarizability α implies a resonance enhancement when $|\epsilon_m + 2\epsilon_d|$ is a minimum, in the case, $Im[\epsilon_m]$ is small or slowly-varying, the resonance enhancement appears at

$$Re[\epsilon(m)] = -2\epsilon_d. \tag{III.2}$$

This is the Fröhlich condition, and the responding mode is dipole surface plasmon of metal nano particle. It is usually used for resonant wavelength as first order estimates for larger particles.

The higher multi-pole orders of resonance condition can be also appropriated using quasi-static regime. For the field propagating inside and outside particle, a continuous tangential electric field and a continuous normal displacement field must be satisfied.

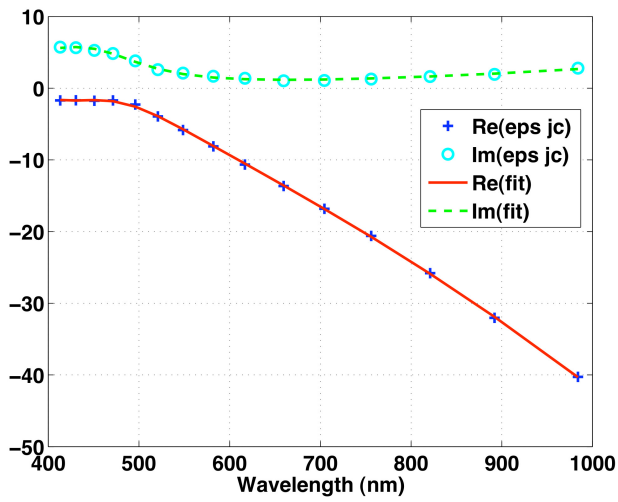

Fig. III.2 – Permittivity of gold with Drude-CP model.

Therefore, the resonance condition for each multi-pole order l,

$$Re[\epsilon(m)] \simeq -\frac{l+1}{l}\epsilon_d. \tag{III.3}$$

When l=1, Eq. III.3 reduced to Eq. III.2 responding to the dipole order.

For gold with the drude-CP model, owing to $Re[\epsilon(m) < 0$ and $\epsilon(m)$ decreases with frequency decreasing(See Fig. III.2), we can conclude that, as the multi-pole order increases, the resonance frequency increases, associated resonance wavelength decreases.

III.2.2 Quasi-static approximation for ellipsoidal particle

For the ellipsoidal particles(with semi-axes a_x, a_y, a_z) described as $\frac{x^2}{a_x^2}+\frac{y^2}{a_y^2}+\frac{z^2}{a_z^2}=1$.

Bohren and Huffman [42] have given the expression of polarizabilities α_i along the i-direction(i=x,y,z) for incident light polarized along the x-direction.

$$\alpha_i = 4\pi a_x a_y a_z \frac{\epsilon_m - \epsilon_d}{3\epsilon_d + 3A_i(\epsilon_m - \epsilon_d)}, \tag{III.4}$$

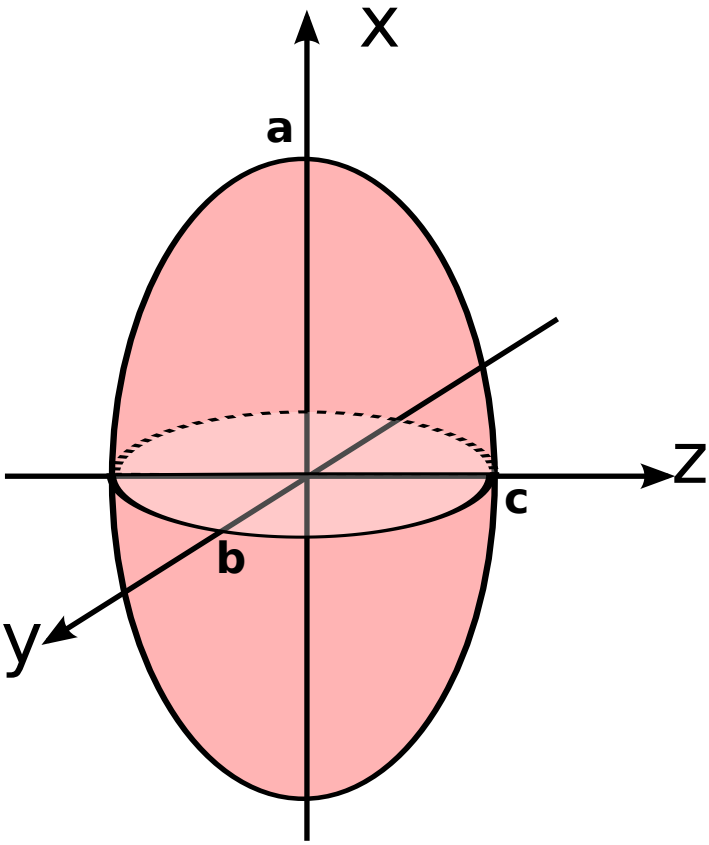

Fig. III.3 – Ellipsoidal particle.

A_i is a geometrical factor, given by

$$A_i = \frac{a_x a_y a_z}{2} \int_0^\infty \frac{ds}{(s + a_i^2) f(s)}, \tag{III.5}$$

where $f(s) = \sqrt{(s + a_x^2)(s + a_y^2)(s + a_z^2)}$. The geometrical factor are related by the equation

$$A_x + A_y + A_z = 1. \tag{III.6}$$

When the denominator in Eq. III.4 is minimum value, the resonance condition is

$$Re[\epsilon_m] \cong \epsilon_d (1 - \frac{1}{A_i}). \tag{III.7}$$

Thus localized SP resonance could occur on three separate spectra for a spheroidal

metal nano particles. Specially, the aspect ratio is defined as $r = b/a$, if b=c and $r < 1$, it is called the prolate spheroidal particles, otherwise oblate spheroids is defined if b=c and $r > 1$, for a=b=c and $r = 1$, the ellipsoidal particle reduces to sphere, which has been presented in the section above. The geometrical factor $A_i, i = x, y, z$ are plotted in Fig. III.4 by mathematical simulation [43], here the incident wave is polarized along the x-direction.

When the aspect ratio (also called axes ratio) increases, the geometrical factor along x-direction A_x decreases,which implies that the charges confined at the lower and upper surfaces of spheroid become more separated and the energy of resonance mode decreases, the localized surface plasmon resonance occurs at $Re[\epsilon_m]$ which is more negative, combining Fig. III.2, the resonance wavelength has a red-shift. In contrary, A_y and A_z increase with axes ratio increase, LSPR positions shift to short wavelength.

As a result, the LSPR wavelength increases if a particle is lengthened along the direction which is the polarized direction of incident light. Conversely, the LSPR wavelength decreases if a particle is lengthened along the direction which is perpendicular to the polarized direction of incident light.

The field, at the tip of the prolate spheroid for incident light polarized along the x-direction, can be approximated as a product of the induced dipole field and the enhancement from lighting-rod effect [44].

$$E_{tip} = ME_{dip} + E_{inc}, \tag{III.8}$$

here the new geometrical factor M is defined as

$$M = \frac{3}{2}(\frac{a_x}{a_y})^2(1 - A_x), \tag{III.9}$$

E_{dip} is dipole field at the tip of the spheroid, it is given by

$$E_{dip} = 2\frac{p}{R^3}, \tag{III.10}$$

p is the induced dipole moment, which is determined by integrating the polarization

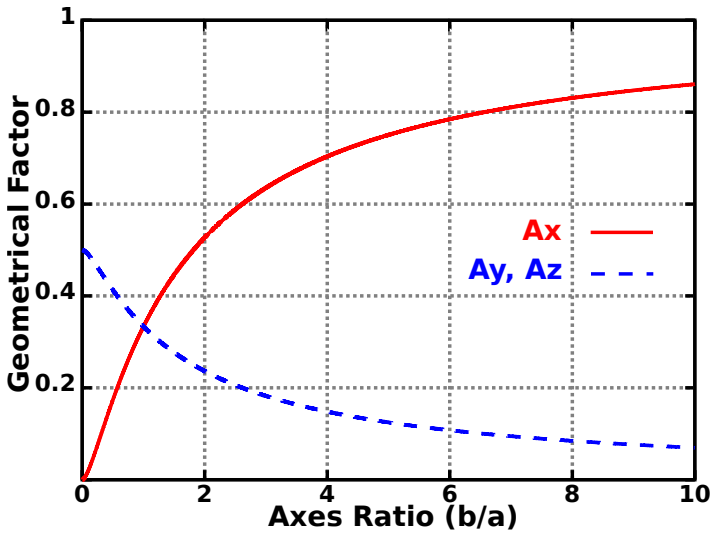

Fig. III.4 – Geometrical factor for prolate and oblate spheroidal particles with the minor axes equal in length(b=c).

of the ellipsoid over its volume.

$$p = (\frac{4\pi a_x a_y a_z}{3})\frac{1}{4\pi}[\frac{\epsilon_m - \epsilon_d}{\epsilon_d + (\epsilon_m - \epsilon_d)A_x}]E_{inc}. \tag{III.11}$$

In the quasi-static approximation, for prolate spheroids with $a_y/a_x \to 0$, $A_x \to 0$, then enhancement factor $M \to \frac{3}{2}(\frac{a_x}{a_y})^2$, which increases with axes ratio. Meanwhile, the field E_{dip}, induced by dipole moment, decreases. It is the reason for the field at the tip of ellipsoid having a maximum, and can not increase infinitely with axes ratio.

For oblate spheroids with $a_y/a_x \to \infty$, $A_x \to 1$, then field enhancement factor $M \to 0$.

To investigate the phase-changes of the incident wave over the particle volume, Mie theory is introduced in 1908 to describe the internal and scattered fields using a series of normal modes by vector harmonics. Nevertheless, Mie theory is only suitable for spherical particle, for non-regular structure, other methods are developed, for instance finite element method(FEM), finite difference time domain method(FDTD), generalized multi-pole technique.

III.3 Surface Enhanced Raman Scattering

In 1974, Fleischmann and coworkers [52] observed high-intensity Raman spectra from pyridine molecules adsorbed on anodized silver electrode surfaces. They attributed the enhancement Raman spectra to a large increase in the effective surface area due to the roughness. However, in 1977, Jeanmaire and Van Duyne and Albrecht and Creighton came to the conclusion that an intrinsic surface enhancement effect was due to an enormously increase in the Raman cross section of the pyridine molecules when they became adsorbed on the Ag surface. It is called Surface-enhanced Raman scattering.

Subsequently, the mechanism of the Raman amplification have been investigated. It is now well established that Surface-enhanced Raman scattering(SERS) is attributed to the electromagnetic enhancement due to the local field of a surface plasmon (SP) excited in a nano-particle by the incident light [53; 54]. SERS could provide the valuable information for studying vibrational spectra of the molecules absorbed by particles.

If we neglect the chemical interactions between the molecules and the metal, and assume that no-influence of induced dipole exists in the molecule on the polarization of metal particles, the intensity amplification of the Raman emitted photon may be defined by using the field E at the incident photon frequency ω_{exc} while calculated at the scattered frequency ω_{Rs} [55]. Thus the SERS gain is proportional to the local field enhancement at the incident and at the scattered Raman Stokes frequencies [56; 57], which is described as

$$G_{SERS} = |\frac{E_{loc}(\omega_{exc})E_{loc}(\omega_{Rs})}{E_{inc}(\omega_{exc})E_{inc}(\omega_{Rs})}|^2 = g(\omega_{exc})g(\omega_{RS}), \tag{III.12}$$

where

$E_{loc}(\omega_{exc})$: the local electric fields at the laser excitation angular frequencies ω_{exc},

$E_{loc}(\omega_{RS})$: the local electric fields at the Raman angular frequencies ω_{RS},

$E_{inc}(\omega_{exc})$: the amplitude of the incident fields at the laser excitation angular frequencies ω_{exc},

$E_{inc}(\omega_{RS})$: the amplitude of the incident fields at the Raman angular frequencies ω_{RS}.

Consequently, the overall gain appears to be described as the product of the gain at the laser angular frequency $g(\omega_{exc})$ times the gain $g(\omega_{RS})$ at the Raman angular frequency. Therefore, large SERS signals are expected when both the frequency of the incident and Raman scattered electromagnetic fields approach the LSPR.

Prolate spheroid particles for instance, with major axis 2a and minor axis 2b, the electromagnetic field E_0 is applied along major axis, the resulting field at the surface of the spheroid in spheroidal coordinate is given [58].

$$|E|^2 = |E_0|^2[|1-\Xi|^2 + \frac{2Re(1-\Xi)\Xi^* s^2}{Q_1(\Xi_0^2)(\Xi_0^2 - s^2)} + \frac{\Xi^2 s^2}{Q_1(\Xi_0)^2(\Xi_0^2-1)(\Xi_0^2-s^2)}], \tag{III.13}$$

where

$$\begin{aligned}
&\Xi = \frac{\epsilon_m - \epsilon_d}{\epsilon_m + \chi\epsilon_d}, \\
&\chi = -1 + 1/[(\Xi_0^2 - 1)Q_1(\Xi_0)], \\
&\Xi_0 = (1 - b^2/a^2)^{-1/2}, \\
&Q_1(\Xi_0) = 1/2\Xi_0 ln[(\Xi_0+1)/(\Xi_0-1)] - 1, \\
&s = cos\theta[(\Xi_0^2-1)/(\Xi_0^2 - cos^2\theta)]^{1/2},
\end{aligned} \tag{III.14}$$

ϵ_m and ϵ_d are the dielectric parameter inside and outside the spheroid, which are the same with section 3.

Eq. III.13 implies that SERS is influenced only by the size of particles b/a, but this conclusion is wrong in some cases. Induced dipoles in particles, which is larger than a few percent of the wavelength of light, can be substantially affected by the radiation damping [59; 60] and dynamic depolarization effects [61]. SERS has a large potential in analytical chemistry and in biological applications.

III.4 Application

Owing to the tunability of positions and intensity of localized surface plasmon resonance spectroscopy, LSPR becomes a powerful technique for engineering and sensors application. We will introduce two main applications in this section.

III.4.1 Sensors

Nanoparticle-based LSPR sensing, including refractive index sensing, molecular sensing. LSPR sensing can detect the target antigen, biotin-streptavidin interaction and antibody-antigen. LSPR has been used to detect other biomolecular interactions, including nucleic acid hybridization and protein-carbohydrate, aptamer-protein and cytochrome-inhibitor interaction. Furthermore, LSPR are suitable for the chemical sensing application because LSPR sensors are rapid, including gas sensors [62]and pH sensors [63]. Nano-particle sensor are mostly based on plasmonic resonance energy transfer [64].

Owing to low cost and based on simple extinction measurement, LSPR sensors will become biomolecular research tool and medical diagnostic tool. The biggest challenges are the sensitivities of single-particle, single-molecule detection, and the sensitivities of strong, nano-particle ensemble based substrates.

III.4.2 Photonic device

Near-field coupling of LSPR is being exploited for the application of nano-scale opticle and photonic devices [65; 5]. By modifying the sizes, shapes and the periods of the metal nano-particles arrays, LSPR can be used for the manufactures of super-lenses, optical data storage device [66], plasmon waveguides and nano-optics [43; 67]. The essence for Photonic device is the ability to concentrate and channel electromagnetic wave [5].

III.5 Conclusion

The basic physics of LSPR have been presented using the cylinder, spheric and ellipsoidal particle separately. SERS technology and the application of LSPR have also been introduced simply. These will provide the theoretical resistance for the structure we used and results analysis in the later chapters.

Chapitre IV

Numerical Method

Finite-difference time-domain method (FDTD) provide a accurate prediction of electromagnetic wave propagations. Owing to the remarkably advantages, in this chapter, we will review the developments of FDTD, and then introduce the main techniques we have used in our work, including the Yee algorithm, Courant stability condition, absorbing boundary conditions, numerical models for dispersive materials and anisotropic materials. In the end, combining nematic liquid crystal and gold nano-particles, we will give the code to simulate the extinction spectra of the structure we used.

IV.1 Review of FDTD

Accurate numerical calculation of full-vector electromagnetic wave interactions with arbitrary materials and structures are difficult. Proper numerical modelings are needed to approach this purpose, Finite-difference time-domain method is the preferred choice for electromagnetic wave penetration, scattering problems et al. [68; 69]. This method will be introduced in details subsequently.

IV.1.1 The introduction of FDTD

Maxwell's partial differential equations of electrodynamics describe an unification of electric and magnetic fields, which predict electromagnetic phenomena. For solving Maxwell's curl equations directly in the time domain on a space grid, finite-difference time-domain method (FDTD) is described by Yee in 1966 [27]. In this algorithm, by making the discretization of space and time, the temporal and spatial derivatives in Maxwell's equations are deduced for the electromagnetic fields at the "next" time

based on the values at "previous" time steps. The leapfrog is used for time evolution, meanwhile, for the spacial discretization, the staggered grid is chosen which is composed of Yee cells.

Initially, the FDTD method is introduced for isotropic and non-dispersive materials. To broaden the application domain, Luebbers et al. proposed an algorithm for dispersive-dependent materials ($(FD)^2TD$) [70]. This algorithm can be used to compute transient propagation in plasma when the plasma can be characterized by a complex frequency-dependent permittivity [71]. Meanwhile, Joseph et al. [72] introduced a FDTD modeling of frequency-dependent dielectric permittivity ; Nickisch and Franke have developed an algorithm based on FDTD for dispersive material [73]. Other researchers, Strikel and Taflove [74], and Beker et al [75] for instance, have published articles using FDTD with anisotropic materials.

The success of FDTD is partially owing to the emergency of absorbing boundary conditions(ABC), that is for absorbing energy propagating from the interior to the edge of the computational mesh. The first algorithm of ABC for Yee' grid is proposed by Mur in 1981, which is second-order accurate and numerically stable [76]. Later, Berenger introduced the highly effective, perfectly matched layer(PML) absorbing boundary conditions in 1994[77], subsequently, Gedney [78], Sacks and his co-workers [79] introduced a realizable and perfectly matched anisotropic-absorbing medium (UPML) for the truncation of FDTD lattices. As an advanced absorbing boundary condition, convolutional perfectly matched layer (CPML) is described by Roden in 2000 [80]. The application of CPML completely does not depend on the host medium, thus, no modifications are needed when applying CPML to inhomogeneous, anisotropic, lossy, dispersive, or nonlinear media.

Owing to the explicit nature of FDTD algorithms, it becomes one of the most effective and popular tools for the numerical solution of Maxwell's curl equations. We now cite some applications of FDTD computational electrodynamics modeling [69; 81; 82].

* Cellphone radiation interacting with the human head.

* Early-stage detection of breast cancer using an ultra wide band microwave radar.

* Waveguide and micro-strip circuits.

* Application to the calculation of dispersion characteristics of magnetized ferrite

* Photonic crystal micro-cavity laser

IV.1.2 Yee algorithm

Maxwell's equations

Considering a region with no charges ($\rho = 0$) and no currents ($\overrightarrow{J} = 0$), but with materials that absorb electromagnetic field energy. The time-dependent maxwell's equations are presented as :

$$\begin{aligned} Faraday's\ \ Law: &\quad \overrightarrow{\nabla} \times \overrightarrow{E} + \overrightarrow{M} = -\frac{\partial \overrightarrow{B}}{\partial t} \\ Ampere's\ \ Law: &\quad \overrightarrow{\nabla} \times \overrightarrow{H} - \overrightarrow{J} = \frac{\partial \overrightarrow{D}}{\partial t} \\ Gauss'\ Law\ for\ the\ electric\ field: &\quad \overrightarrow{\nabla} \bullet \overrightarrow{D} = 0 \\ Gauss'\ Law\ for\ the\ magnetic\ field: &\quad \overrightarrow{\nabla} \bullet \overrightarrow{B} = 0 \end{aligned} \tag{IV.1}$$

In the equations above, the symbols are defined as follows :

$\overrightarrow{E}$: elctric field(Volts/meter)

$\overrightarrow{H}$: magnetic field(amperes/meter)

$\overrightarrow{D}$: electric flux density(coulombs/meter^2)

$\overrightarrow{B}$: magnetic flux density(webers/meter^2)

$\overrightarrow{J}$: electric current density(amperes/meter^2)

$\overrightarrow{M}$: equivalent magnetic current density(volts/meter^2)

For the materials with relative permittivity ε_r and relative permeability μ_r, we can relate $\overrightarrow{D}$ and $\overrightarrow{E}$, $\overrightarrow{B}$ and $\overrightarrow{H}$ using

$$\begin{aligned} \overrightarrow{D} &= \varepsilon \overrightarrow{E} = \varepsilon_r \varepsilon_0 \overrightarrow{E} \\ \overrightarrow{B} &= \mu \overrightarrow{E} = \mu_r \mu_0 \overrightarrow{E} \end{aligned} \tag{IV.2}$$

We should note that $\overrightarrow{J}$ and $\overrightarrow{M}$ can act as independent sources of electric and magnetic field energy, $\overrightarrow{J}_{source}$ and $\overrightarrow{M}_{source}$. Thus electric and magnetic fields are attenuated via conversion to heat energy for materials with isotropic and non-dispersive. Hence, electric current density and equivalent magnetic current are given as

$$\begin{aligned} \overrightarrow{J} &= \overrightarrow{J}_{source} + \sigma \overrightarrow{E} \\ \overrightarrow{M} &= \overrightarrow{M}_{source} + \sigma^* \overrightarrow{H} \end{aligned} \tag{IV.3}$$

where

σ is electric conductivity(siemens/meter)

σ^* is equivalent magnetic loss(siemens/meter).

Yee cell

Any function u is described at a discrete point in the Yee lattice and at a discrete point in time as

$$u(i\Delta x, j\Delta y, k\Delta z, n\Delta t) = u^n_{i,j,k} \tag{IV.4}$$

where i, j, k, n are integers. To understand this easily, the Fig.IV.1 are presented.

Moreover, positions of the electric and magnetic field vector components about a cubic unit cell of the Yee space lattice is seen in Fig.IV.2. Here, $\Delta x, \Delta y$, and Δz are the lattice space increments at Cartesian coordinate system in the x, y and z coordinate directions. Δt is the time increment.

Space-time schematic of Yee algorithm for one-dimensional wave propagation is described in Fig. IV.3, it has shown the leapfrog for the time derivatives and the central differences for the space derivatives.

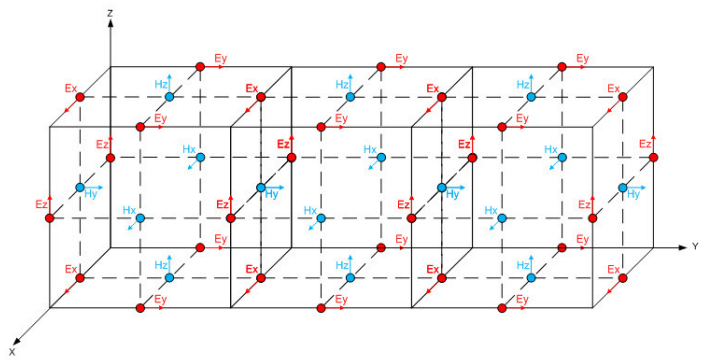

Fig. IV.1 – Schematic of Yee lattice.

Field Components		Space points			Time points
		X axis	Y axis	Z axis	
E	Ex	i+1/2	j	k	n
	Ey	i	j+1/2	k	
	Ez	i	j	k+1/2	
H	Hx	i	j+1/2	k+1/2	n+1/2
	Hy	i+1/2	j	k+1/2	
	Hz	i+1/2	j+1/2	k	

Fig. IV.2 – Positions of the electric and magnetic field vector components about a cubic unit cell of the Yee lattice.

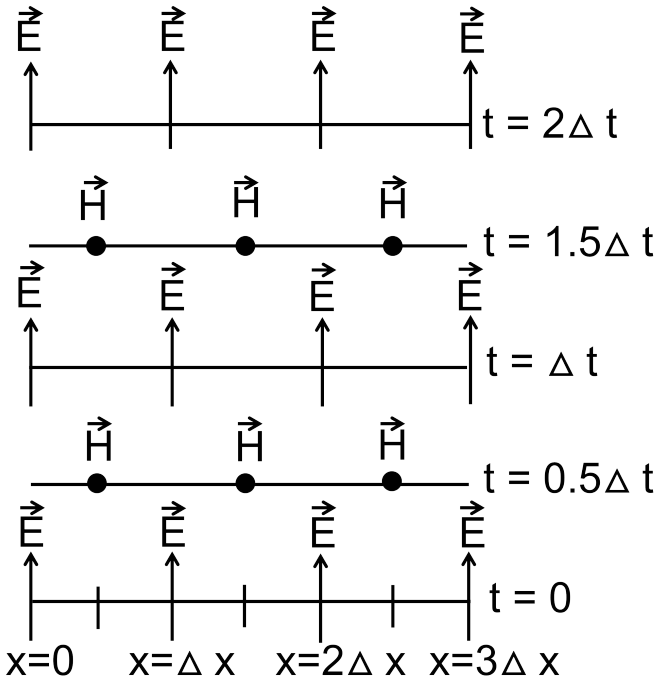

Fig. IV.3 – Space-time schematic of Yee algorithm for one-dimensional.

Initial conditions for both electric and magnetic fields are zero everywhere in the grid. Combining Eq. IV.1, Eq. IV.2, Eq. IV.3 and Eq. IV.4, the numerical approximation of Maxwell's curl equations in three dimensions can be given. For instance, E_x field-component equation can be written as follows :

$$\frac{\partial E_x}{\partial t} = \frac{1}{\varepsilon}[\frac{\partial H_z}{\partial y} - \frac{\partial H_y}{\partial z} - (J_{sourcex} + \sigma E_x)] \tag{IV.5}$$

Referring to Fig. IV.1 and Fig. IV.2, a typical time and space derivative at $E_x(i + 1/2, j, k, n)$ is presented as :

$$\begin{aligned}\frac{E_x|^{n+1/2}_{i+1/2,j,k} - E_x|^{n-1/2}_{i+1/2,j,k}}{\Delta t} =& \frac{1}{\varepsilon_{i+1/2,j,k}}\{\frac{H_z|^n_{i+1/2,j+1/2,k} - H_z|^n_{i+1/2,j-1/2,k}}{\Delta y} \\ &- \frac{H_y|^n_{i+1/2,j,k+1/2} - H_y|^n_{i+1/2,j,k-1/2}}{\Delta z} \\ &- J_{sourcex}|^n_{i+1/2,j,k} - \sigma_{i+1/2,j,k} E_x|^n_{i+1/2,j,k}\}\end{aligned} \tag{IV.6}$$

Owing to the E_x values at time-step n are not assumed to be stored in the computer's memory during the simulations, but the previous values of E_x at time-step n-1/2 are considered to be in the memory. Next, the term $E_x|^n_{i+1/2,j,k}$ on the right-hand side of Eq. IV.6 should be modified using semi-implicit approximation.

$$E_x|^n_{i+1/2,j,k} = \frac{E_x|^{n+1/2}_{i+1/2,j,k} + E_x|^{n-1/2}_{i+1/2,j,k}}{2} \tag{IV.7}$$

Semi-implicit approximation has been found to lead to numerically stable and accurate results for values of σ from zero to infinity. Thus, the explicit time-stepping relation for $E_x|^{n+1/2}_{i+1/2,j,k}$

$$\begin{aligned}E_x|^{n+1/2}_{i+1/2,j,k} =& (\frac{1 - \frac{\sigma_{i+1/2,j,k}\Delta t}{2\varepsilon_{i+1/2,j,k}}}{1 + \frac{\sigma_{i+1/2,j,k}\Delta t}{2\varepsilon_{i+1/2,j,k}}}) E_x|^{n-1/2}_{i+1/2,j,k} + \frac{\frac{\Delta t}{\varepsilon_{i+1/2,j,k}}}{1 + \frac{\sigma_{i+1/2,j,k}\Delta t}{2\varepsilon_{i+1/2,j,k}}}\{\frac{H_z|^n_{i+1/2,j+1/2,k} - H_z|^n_{i+1/2,j-1/2,k}}{\Delta y} \\ &- \frac{H_y|^n_{i+1/2,j,k+1/2} - H_y|^n_{i+1/2,j,k-1/2}}{\Delta z} - J_{sourcex}|^n_{i+1/2,j,k}\}\end{aligned} \tag{IV.8}$$

Correspondingly, the explicit time-stepping relation for $H_x|^{n+1}_{i,j+1/2,k+1/2}$

$$H_x|^{n+1}_{i,j+1/2,k+1/2} = \left(\frac{1-\dfrac{\sigma^*_{i,j+1/2,k+1/2}\Delta t}{2\mu_{i,j+1/2,k+1/2}}}{1+\dfrac{\sigma^*_{i,j+1/2,k+1/2}\Delta t}{2\mu_{i,j+1/2,k+1/2}}}\right)H_x|^{n}_{i,j+1/2,k+1/2} + \frac{\dfrac{\Delta t}{\mu_{i,j+1/2,k+1/2}}}{1+\dfrac{\sigma^*_{i,j+1/2,k+1/2}\Delta t}{2\mu_{i,j+1/2,k+1/2}}}$$
$$\left\{\frac{E_y|^{n+1/2}_{i,j+1/2,k+1} - E_z|^{n+1/2}_{i,j+1/2,k}}{\Delta z} - \frac{E_z|^{n+1/2}_{i,j+1,k+1/2} - E_z|^{n+1/2}_{i,j,k+1/2}}{\Delta y} - M_{sourcex}|^{n}_{i,j+1/2,k+1/2}\right\}$$

Similarly, the finite-difference expressions of E_y, E_z, H_y, and H_z can be derived using Yee's algorithm according to the unit cell.

IV.1.3 The stability and accuracy of FDTD

Where $\Delta x = \Delta y = \Delta z$ is the space increment, and Δt is the time increment. Any function of space and time is described as

$$F^n_{i,j,k} = F(i\Delta x, j\Delta y, k\Delta z, n\Delta t) \tag{IV.9}$$

The field vector, with complex-valued numerical angular frequency $\omega = \omega_{real} + j\omega_{imag}$, can be written as

$$\begin{aligned} F|^n_{i,j,k} &= F_0 e^{j[(\omega_{real}+j\omega_{imag})n\Delta t - k_x i\Delta x - k_y j\Delta y - k_z k\Delta z]} \\ &= F_0 e^{-\omega_{imag} n\Delta t} e^{j(\omega_{real} n\Delta t - k_x i\Delta x - k_y j\Delta y - k_z k\Delta z)} \end{aligned} \tag{IV.10}$$

where k_x, k_y, k_z are the three elements of wavenumber of the numerical sinusoidal traveling wave in Cartesian coordinates. Thus, the general form of numerical dispersion relation for the vector field using Yee algorithm in three dimensions is

$$[\frac{1}{c\Delta t}sin(\frac{\omega\Delta t}{2})]^2 = [\frac{1}{\Delta x}sin(\frac{k_x\Delta x}{2})]^2 + [\frac{1}{\Delta y}sin(\frac{k_y\Delta y}{2})]^2 + [\frac{1}{\Delta z}sin(\frac{k_z\Delta z}{2})]^2 \tag{IV.11}$$

Solving Eq. IV.11 for ω, we get

$$\omega = \frac{2}{\Delta t} sin^{-1}(\varsigma) \tag{IV.12}$$

with

$$\varsigma = c\Delta t \sqrt{[\frac{1}{\Delta x} sin(\frac{k_x \Delta x}{2})]^2 + [\frac{1}{\Delta y} sin(\frac{k_y \Delta y}{2})]^2 + [\frac{1}{\Delta z} sin(\frac{k_z \Delta z}{2})]^2} \tag{IV.13}$$

when the wave-vector components of propagating numerical wave fulfill the conditions as

$k_x = \pm\frac{\pi}{\Delta x}$, $k_y = \pm\frac{\pi}{\Delta y}$, $k_z = \pm\frac{\pi}{\Delta z}$

thus, the ς_{max} can be written as

$$\varsigma_{max} = c\Delta t \sqrt{\frac{1}{(\Delta x)^2} + \frac{1}{(\Delta y)^2} + \frac{1}{(\Delta z)^2}} \tag{IV.14}$$

We can observe $0 < \varsigma < \varsigma_{max}$. Obviously, depending on the choice of Δt, ς_{max} can exceed 1 , this leads to the complex values for ω which give rise to numerical instability. The courant stability enforced $\varsigma_{max} < 1$, hence

$$\Delta t < \frac{1}{c\sqrt{\frac{1}{(\Delta x)^2} + \frac{1}{(\Delta y)^2} + \frac{1}{(\Delta z)^2}}} \tag{IV.15}$$

If $\Delta x = \Delta y = \Delta z = \Delta$, we could get $\Delta t < \frac{\Delta}{\sqrt{3}c}$ [83].

IV.1.4 Absorbing boundary conditions

Three-dimensional time-domain Maxwell's equations for Berenger's split-field PML have been developed, in this way, Cartesian field vector components are split. For

instance, x elements for Ampere's law is given by

$$\begin{aligned}(\varepsilon\frac{\partial}{\partial t}+\sigma_y)E_{xy} &= \frac{\partial}{\partial y}(H_{zx}+H_{zy})\\ (\varepsilon\frac{\partial}{\partial t}+\sigma_z)E_{xz} &= -\frac{\partial}{\partial z}(H_{yx}+H_{yz})\end{aligned} \tag{IV.16}$$

Similarly, the modified Faraday's law is written by

$$\begin{aligned}(\mu\frac{\partial}{\partial t}+\sigma_y^*)H_{xy} &= -\frac{\partial}{\partial y}(E_{zx}+E_{zy})\\ (\mu\frac{\partial}{\partial t}+\sigma_z^*)H_{xz} &= -\frac{\partial}{\partial z}(E_{yx}+E_{yz})\end{aligned} \tag{IV.17}$$

If we define $w = x, y, z$, the matching condition at a normal-to-w PML interface in the FDTD lattice has the parameter pair (σ_w, σ_w^*).

For the normal incidence(θ =0) of the impinging wave, we have the reflection factor

$$\Gamma = \frac{\eta_1-\eta_2}{\eta_1+\eta_2} \tag{IV.18}$$

where η_1 and η_2 are the wave impedances in regions 1 and 2.

$$\begin{aligned}\eta_1 &= \sqrt{\frac{\mu_1}{\varepsilon_1}}\\ \eta_2 &= \sqrt{\frac{\mu_2(1+\sigma^*/jw\mu_2)}{\varepsilon_2(1+\sigma/jw\varepsilon_2)}}\end{aligned} \tag{IV.19}$$

When the following conditions are fulfilled, a reflectionless between region 1 and region 2 interface is implemented for normally impinging wave.

$$\begin{aligned}\varepsilon_1 &= \varepsilon_2\\ \mu_1 &= \mu_2\\ \sigma^*/\mu_1 &= \sigma/\varepsilon_1\end{aligned} \tag{IV.20}$$

The PML formulation is posed in the stretched coordinate space [84]. To describe Maxwell's equations into a complex coordinate space, the split-field equations are re-

posed in a nonsplit form. We suppose that the PML parameters s_ω are continuous functions along the axial directions. And the coordinate as follows are introduced.

$$\widetilde{x} \rightarrow \int_0^x s_x(x^{'})dx^{'}; \widetilde{y} \rightarrow \int_0^y s_y(y^{'})dy^{'}; \widetilde{z} \rightarrow \int_0^z s_z(z^{'})dz^{'}. \tag{IV.21}$$

The partial derivatives are then

$$\begin{aligned} \frac{\partial}{\partial \widetilde{x}} &= \frac{1}{s_x}\frac{\partial}{\partial x}; \\ \frac{\partial}{\partial \widetilde{y}} &= \frac{1}{s_y}\frac{\partial}{\partial y}; \\ \frac{\partial}{\partial \widetilde{z}} &= \frac{1}{s_z}\frac{\partial}{\partial z}. \end{aligned} \tag{IV.22}$$

the ∇ operator in this space is defined as

$$\begin{aligned} \widetilde{\nabla} &= \widehat{x}\frac{\partial}{\partial \widetilde{x}} + \widehat{y}\frac{\partial}{\partial \widetilde{y}} + \widehat{z}\frac{\partial}{\partial \widetilde{z}} \\ &= \widehat{x}\frac{1}{s_x}\frac{\partial}{\partial x} + \widehat{y}\frac{1}{s_y}\frac{\partial}{\partial y} + \widehat{z}\frac{1}{s_z}\frac{\partial}{\partial z} \end{aligned} \tag{IV.23}$$

The Ampere's law is thus specified as

$$\begin{aligned} j\omega\varepsilon\overrightarrow{E} + \sigma\overrightarrow{E} &= \widetilde{\nabla} \times \overrightarrow{H} \\ &= \widehat{x}(\frac{1}{s_y}\frac{\partial H_z}{\partial y} - \frac{1}{s_z}\frac{\partial H_y}{\partial z}) + \widehat{y}(\frac{1}{s_z}\frac{\partial H_x}{\partial z} - \frac{1}{s_x}\frac{\partial H_z}{\partial x}) + \widehat{z}(\frac{1}{s_x}\frac{\partial H_y}{\partial x} - \frac{1}{s_y}\frac{\partial H_x}{\partial y}) \end{aligned} \tag{IV.24}$$

Similarly, the Faraday's law is as follows

$$\begin{aligned} -j\omega\mu\overrightarrow{H} + \sigma^*\overrightarrow{H} &= \widetilde{\nabla} \times \overrightarrow{E} \\ &= \widehat{x}(\frac{1}{s_y}\frac{\partial E_z}{\partial y} - \frac{1}{s_z}\frac{\partial E_y}{\partial z}) + \widehat{y}(\frac{1}{s_z}\frac{\partial E_x}{\partial z} - \frac{1}{s_x}\frac{\partial E_z}{\partial x}) + \widehat{z}(\frac{1}{s_x}\frac{\partial E_y}{\partial x} - \frac{1}{s_y}\frac{\partial E_x}{\partial y}) \end{aligned} \tag{IV.25}$$

where s_w are the stretched-coordinate metrics, which was originally proposed by Berenger to be

$$s_w = 1 + \frac{\sigma_w}{jw\varepsilon_0}, \tag{IV.26}$$

here $w = x, y, z$.

We take x-projection of Ampere's law for instance, it is rewritten as follows.

$$j\omega\varepsilon E_x + \sigma E_x = \frac{1}{s_y}\frac{\partial H_z}{\partial y} - \frac{1}{s_z}\frac{\partial H_y}{\partial z} \tag{IV.27}$$

Eq. IV.27 is transformed into time-domain, owing to the frequency dependence of the stretched-coordinate metrics, this results is presented in a convolution form :

$$\varepsilon\frac{\partial E_x}{\partial t} + \sigma E_x = \overline{s}_y(t) * \frac{\partial H_z}{\partial y} - \overline{s}_z(t) * \frac{\partial H_y}{\partial z} \tag{IV.28}$$

here, on the right-hand side, $s(t)$ is the inverse Laplace transform of s(w).

The time-dependent form of the stretched-coordinate formulation of Maxwell's equations(Eq. IV.28) is the basis of CPML method. Owing to the tensor coefficient s_x has a pole at zero frequency, that means $s_x \to -j\infty$ when $\omega \to 0$. This problem can be solved if the pole can be shifted to the upper-half complex plane. Some researchers([80; 85]) have proposed the tensor coefficient s_w as

$$s_w = k_w + \frac{\sigma_w}{\alpha_w + j\omega\varepsilon_0} \tag{IV.29}$$

where s_w and σ_w are assumed to be positive real values, $k_w \geqslant 1$ and it is real also.

Using Laplace trnsform theory, we can shown that $\overline{s}_w$ has the formation of impulse

response

$$\begin{aligned}\overline{s}_w(t) &= \frac{\delta(t)}{k_w} - \frac{\sigma_w}{\varepsilon_0 k_w^2} e^{-(\frac{\sigma_w}{\varepsilon_0 k_w}+\frac{\alpha_w}{\varepsilon_0})t} u(t) \\ &= \frac{\delta_w}{k_w} + \xi_w(t)\end{aligned} \tag{IV.30}$$

where $\delta(t)$ means the unit impulse function and u(t) is the step function. Combining the Eq. IV.27 and Eq. IV.30, we could get

$$\varepsilon_r \varepsilon_0 \frac{\partial E_x}{\partial t} + \sigma E_x = \frac{1}{k_y}\frac{\partial H_z}{\partial y} - \frac{1}{k_z}\frac{\partial H_y}{\partial z} + \xi_y(t) * \frac{\partial H_z}{\partial y} - \xi_z(t) * \frac{\partial H_y}{\partial z} \tag{IV.31}$$

The convolution in the Eq. IV.31 can be efficient representation if we defined the discrete impulse response for $\xi_w(t)$ as

$$\begin{aligned}Z_w(m) &= \int_{m\Delta t}^{(m+1)\Delta t} \xi_w(\tau) d\tau \\ &= -\frac{\sigma_w}{\varepsilon_0 k_w^2} \int_{m\Delta t}^{(m+1)\Delta t} e^{-(\frac{\sigma_w}{\varepsilon_0 k_w}+\frac{\alpha_w}{\varepsilon_0})\tau} d\tau \\ &= c_w e^{-(\frac{\sigma_w}{\varepsilon_0 k_w}+\frac{\alpha_w}{\varepsilon_0})m\Delta t}\end{aligned} \tag{IV.32}$$

where

$$c_w = \frac{\sigma_w}{\sigma_w k_w + k_w^2 \alpha_w}(e^{-(\frac{\sigma_w}{k_w \varepsilon_0}+\frac{\alpha_w}{\varepsilon_0})\Delta t} - 1.0) \tag{IV.33}$$

Utilizing Eq. IV.32 and Eq. IV.33, Eq. IV.31 is discretized in both space and time

according to a staggered Yee scheme,

$$\begin{aligned}
&\varepsilon_r\varepsilon_0\frac{E_x|^{n+1/2}_{i+1/2,j,k}-E_x|^{n-1/2}_{i+1/2,j,k}}{\Delta t}+\sigma\frac{E_x|^{n+1/2}_{i+1/2,j,k}+E_x|^{n-1/2}_{i+1/2,j,k}}{2}=\\
&\frac{H_z|^{n}_{i+1/2,j+1/2,k}-H_z|^{n}_{i+1/2,j-1/2,k}}{k_y\Delta y}-\frac{H_y|^{n}_{i+1/2,j,k+1/2}-H_y|^{n}_{i+1/2,j,k-1/2}}{k_z\Delta z}\\
&+\sum_{m=0}^{N-1}Z_w(m)\frac{H_z|^{n-m}_{i+1/2,j+1/2,k}-H_z|^{n-m}_{i+1/2,j-1/2,k}}{\Delta y}\\
&+\sum_{m=0}^{N-1}Z_w(m)\frac{H_y|^{n-m}_{i+1/2,j,k+1/2}-H_y|^{n-m}_{i+1/2,j,k-1/2}}{\Delta z}
\end{aligned} \tag{IV.34}$$

Using the recursive convolution method [86; 87], the auxiliary expression ψ_w is introduced, and Eq. IV.34 is implemented as

$$\begin{aligned}
&\varepsilon_r\varepsilon_0\frac{E_x|^{n+1/2}_{i+1/2,j,k}-E_x|^{n-1/2}_{i+1/2,j,k}}{\Delta t}+\sigma\frac{E_x|^{n+1/2}_{i+1/2,j,k}+E_x|^{n-1/2}_{i+1/2,j,k}}{2}=\\
&\frac{H_z|^{n}_{i+1/2,j+1/2,k}-H_z|^{n}_{i+1/2,j-1/2,k}}{k_y\Delta y}-\frac{H_y|^{n}_{i+1/2,j,k+1/2}-H_y|^{n}_{i+1/2,j,k-1/2}}{k_z\Delta z}\\
&+\psi_{Exy}|^{n}_{i+1/2,j,k}-\psi_{Exz}|^{n}_{i+1/2,j,k}
\end{aligned} \tag{IV.35}$$

where

$$\begin{aligned}
&\psi_{Exy}|^{n}_{i+1/2,j,k}=b_y\psi_{Exy}|^{n-1}_{i+1/2,j,k}+c_y(\frac{H_z|^{n}_{i+1/2,j+1/2,k}-H_z|^{n}_{i+1/2,j-1/2,k}}{\Delta y})\\
&\psi_{Exz}|^{n}_{i+1/2,j,k}=b_z\psi_{Exz}|^{n-1}_{i+1/2,j,k}+c_z(\frac{H_y|^{n}_{i+1/2,j,k+1/2}-H_y|^{n}_{i+1/2,j,k-1/2}}{\Delta z})\\
&b_w=e^{-(\frac{\sigma_w}{k_w\varepsilon_0}+\frac{\alpha_w}{\varepsilon_0})\Delta t}
\end{aligned} \tag{IV.36}$$

Note that the discrete coefficients b_y and c_y are nonzero only in PML regions with y-normal interface boundaries. The explicit update for E_x is derived directly from

Eq. IV.34, comparing with Eq. IV.8, it is written as

$$
\begin{aligned}
E_x|^{n+1/2}_{i+1/2,j,k} = & \left(\frac{1-\dfrac{\sigma_{i+1/2,j,k}\Delta t}{2\varepsilon_{i+1/2,j,k}}}{1+\dfrac{\sigma_{i+1/2,j,k}\Delta t}{2\varepsilon_{i+1/2,j,k}}}\right)E_x|^{n-1/2}_{i+1/2,j,k} + \\
& \frac{\dfrac{\Delta t}{\varepsilon_{i+1/2,j,k}}}{1+\dfrac{\sigma_{i+1/2,j,k}\Delta t}{2\varepsilon_{i+1/2,j,k}}}\left\{\frac{H_z|^n_{i+1/2,j+1/2,k} - H_z|^n_{i+1/2,j-1/2,k}}{k_y\Delta y} - \frac{H_y|^n_{i+1/2,j,k+1/2} - H_y|^n_{i+1/2,j,k-1/2}}{k_z\Delta z}\right. \\
& \left. + \psi_{Exy}|^n_{i+1/2,j,k} - \psi_{Exz}|^n_{i+1/2,j,k} - J_{sourcex}|^n_{i+1/2,j,k}\right\}
\end{aligned}
\tag{IV.37}
$$

We can also derive equations for the H components. The x-projection of Faraday's law for instance, the explicit update is derived as

$$
\begin{aligned}
H_x|^{n+1}_{i,j+1/2,k+1/2} = & \left(\frac{1-\dfrac{\sigma^*_{i,j+1/2,k+1/2}\Delta t}{2\mu_{i,j+1/2,k+1/2}}}{1+\dfrac{\sigma^*_{i,j+1/2,k+1/2}\Delta t}{2\mu_{i,j+1/2,k+1/2}}}\right)H_x|^n_{i,j+1/2,k+1/2} - \\
& \frac{\dfrac{\Delta t}{\mu_{i,j+1/2,k+1/2}}}{1+\dfrac{\sigma^*_{i,j+1/2,k+1/2}\Delta t}{2\mu_{i,j+1/2,k+1/2}}}\left\{\frac{E_z|^{n+1/2}_{i,j+1,k+1/2} - E_z|^{n+1/2}_{i,j,k+1/2}}{k_y\Delta y} - \frac{E_y|^{n+1/2}_{i,j+1/2,k+1} - H_y|^n_{i,j+1/2,k}}{k_z\Delta z}\right. \\
& \left. + \psi_{Hxy}|^{n+1/2}_{i,j+1/2,k+1/2} - \psi_{Hxz}|^{n+1/2}_{i,j+1/2,k+1/2} - M_{sourcex}|^{n+1/2}_{i,j+1/2,k+1/2}\right\}
\end{aligned}
\tag{IV.38}
$$

where ψ_{Hxy} and ψ_{Hxz} are discrete unknowns stored only in PML regions with y-normal and z-normal interface boundary. These unknowns are updated as follows :

$$
\begin{aligned}
\psi_{Hxy}|^{n+1/2}_{i,j+1/2,k+1/2} &= b_y\psi_{Hxy}|^{n-1/2}_{i,j+1/2,k+1/2} + c_y\left(\frac{E_z|^{n+1/2}_{i,j+1,k+1/2} - E_z|^{n+1/2}_{i,j,k+1/2}}{\Delta y}\right) \\
\psi_{Hxz}|^{n-1/2}_{i,j+1/2,k+1/2} &= b_z\psi_{Hxz}|^{n-1/2}_{i,j+1/2,k+1/2} + c_z\left(\frac{E_y|^{n+1/2}_{i,j+1/2,k+1} - E_y|^{n+1/2}_{i,j+1/2,k}}{\Delta z}\right)
\end{aligned}
\tag{IV.39}
$$

IV.2 Dispersive Materials

The finite-difference time-domain method is originally suitable for constant permittivity, permeability and conductivity. However, for many materials of interest, they are dispersive. The parameters above vary with the frequency. Subsequently, the analytical laws of dispersion appeared.

The generic material dispersive methods include recursive convolution method(RC) [88; 89], Piecewise-linear recursive convolution(PLRC) [90], Z-transform method [91], trapezoidal recursive convolution method [92] and the auxiliary differential equation method(ADE) [93], all of these method are presented to deal with the convolution integral of Maxwell's equations in time-domain. For description of dispersive materials, typical models are used, they are Drude model [70], Lorentz model [89], Critical Points model [94] and any combination of these models [**?** 95].

In this part, the Recursive Convolution Method is firstly introduced in conjuction with the FDTD algorithm. Then the dispersive models coefficients with recursive convolution are described precisely.

IV.2.1 Recursive Convolution Method

The main concept used is that all the information in frequency domain is Fourier transformed to a time-domain function. The convolution is incorporated necessarily into the FDTD formulation. For instance, in the frequency domain, we consider the electric flux density can be expressed as follows

$$\begin{aligned}\overrightarrow{D}(w) &= \varepsilon_0\varepsilon_\infty\overrightarrow{E}(\omega) + \overrightarrow{P}(\omega)\\ &= \varepsilon_0(\varepsilon_\infty + \chi_e(\omega))\overrightarrow{E}(\omega)\end{aligned} \tag{IV.40}$$

where

ε_0 : free-space frequency permittivities.

ε_∞ : Relative infinite frequency permittivities.

P : Polarization.

χ_e : Electric susceptibility.

After Fourier transformation :

$$\overrightarrow{D}(t) = \varepsilon_0\varepsilon_\infty \overrightarrow{E}(t) + \varepsilon_0\chi_e(t) * \overrightarrow{E}(t) \tag{IV.41}$$

where

$$\begin{aligned} \chi_e(t) * \overrightarrow{E}(t) &= \int_{-\infty}^{+\infty} \overrightarrow{E}(t-\tau)\chi(\tau)d\tau \\ &= \int_{-\infty}^{+\infty} \overrightarrow{E}(\tau)\chi(t-\tau)d\tau \end{aligned} \tag{IV.42}$$

Owing to $\overrightarrow{E}(t) = 0$ when $t < 0$, we can get

$$\overrightarrow{D}(t) = \varepsilon_0\varepsilon_\infty \overrightarrow{E}(t) + \varepsilon_0 \int_0^t \overrightarrow{E}(t-\tau)\chi(\tau)d\tau \tag{IV.43}$$

With the Yee's notation, we define $t = n\Delta t$ in Eq. IV.43, thus each vector component of $\overrightarrow{D}(t)$ can be presented as

$$\begin{aligned} \overrightarrow{D}(t) \approx \overrightarrow{D}(n\Delta t) &= \overrightarrow{D}^n \\ &= \varepsilon_0\varepsilon_\infty \overrightarrow{E}^n + \varepsilon_0 \int_0^{n\Delta t} \overrightarrow{E}(n\Delta t-\tau)\chi(\tau)d\tau \end{aligned} \tag{IV.44}$$

One supposition is proposed, all field components are constant over each time interval Δt. the Eq. IV.44 can be written as

$$\overrightarrow{D}^n = \varepsilon_0\varepsilon_\infty \overrightarrow{E}^n + \varepsilon_0 \sum_{m=0}^{n-1} \overrightarrow{E}^{n-m} \int_{m\Delta t}^{(m+1)\Delta t} \chi(\tau)d\tau \tag{IV.45}$$

$$\begin{aligned}\int_0^3 &= \int_0^1 + \int_1^2 + \int_2^3 \\ \overrightarrow{E}^{n-m} &= constant\end{aligned} \tag{IV.46}$$

Similarly, the value of electric flux $\overrightarrow{D}$ at the next time step is

$$\overrightarrow{D}^{n+1} = \varepsilon_0\varepsilon_\infty \overrightarrow{E}^{n+1} + \varepsilon_0 \sum_{m=0}^{n} \overrightarrow{E}^{n+1-m} \int_{m\Delta t}^{(m+1)\Delta t} \chi(\tau)d\tau \tag{IV.47}$$

where

$$\begin{aligned}&\varepsilon_0 \sum_{m=0}^{n} \overrightarrow{E}^{n+1-m} \int_{m\Delta t}^{(m+1)\Delta t} \chi(\tau)d\tau \\ &= \varepsilon_0 \overrightarrow{E}^{n+1} \int_0^{\Delta t} \chi(\tau)d\tau + \varepsilon_0 \sum_{m=1}^{n} \overrightarrow{E}^{n+1-m} \int_{m\Delta t}^{(m+1)\Delta t} \chi(\tau)d\tau \\ &= \varepsilon_0 \overrightarrow{E}^{n+1} \int_0^{\Delta t} \chi(\tau)d\tau + \varepsilon_0 \sum_{k=0}^{n-1} \overrightarrow{E}^{n-k} \int_{(k+1)\Delta t}^{(k+2)\Delta t} \chi(\tau)d\tau \\ &= \varepsilon_0 \overrightarrow{E}^{n+1} \int_0^{\Delta t} \chi(\tau)d\tau + \varepsilon_0 \sum_{m=0}^{n-1} \overrightarrow{E}^{n-m} \int_{(m+1)\Delta t}^{(m+2)\Delta t} \chi(\tau)d\tau\end{aligned} \tag{IV.48}$$

Subtraction is used between Eq. IV.47 and Eq. IV.45, we find

$$\begin{aligned}\overrightarrow{D}^{n+1} - \overrightarrow{D}^{n} = \varepsilon_\infty\varepsilon_0(\overrightarrow{E}^{n+1} - \overrightarrow{E}^{n}) + \varepsilon_0 \overrightarrow{E}^{n+1} \int_0^{\Delta t} \chi(\tau)d\tau \\ + \varepsilon_0 \sum_{m=0}^{n-1} \overrightarrow{E}^{n-m} \int_{(m+1)\Delta t}^{(m+2)\Delta t} \chi(\tau)d\tau - \int_{m\Delta t}^{(m+1)\Delta t} \chi(\tau)d\tau\end{aligned} \tag{IV.49}$$

To simplify the notation, we let

$$\chi_m = \int_{m\Delta t}^{(m+1)\Delta t} \chi(\tau)d\tau \tag{IV.50}$$

With the definition $\Delta\chi_m = \chi_m - \chi_{m+1}$, and using FDTD algorithm, the Ampere's Law described again as follows

$$\triangledown \times \overrightarrow{H} = \frac{\partial \overrightarrow{D}}{\partial t} + \sigma \overrightarrow{E} = \frac{D^{n+1} - D^n}{\Delta t} + \sigma \overrightarrow{E} \tag{IV.51}$$

Combining the Eq. IV.49, Eq. IV.50 and Eq. IV.51, we find

$$\begin{aligned}\Delta t \triangledown \times \overrightarrow{H}|^{n+\frac{1}{2}} &= (\varepsilon_0\varepsilon_\infty + \varepsilon_0\chi_0)\overrightarrow{E}^{n+1} - \varepsilon_0\varepsilon_\infty \overrightarrow{E}^n - \varepsilon_0 \sum_{m=0}^{n-1} \overrightarrow{E}^{n-m}\Delta\chi_m + \sigma\Delta t \overrightarrow{E}^{n+1} \\ &= (\varepsilon_0\varepsilon_\infty + \varepsilon_0\chi_0 + \sigma\Delta t)\overrightarrow{E}^{n+1} - \varepsilon_0\varepsilon_\infty \overrightarrow{E}^n - \varepsilon_0 \sum_{m=0}^{n-1} \overrightarrow{E}^{n-m}\Delta\chi_m\end{aligned} \tag{IV.52}$$

solving for $\overrightarrow{E}|^{n+1}$, we can get

$$\begin{aligned}\overrightarrow{E}|^{n+1} =& \frac{\varepsilon_\infty}{\varepsilon_\infty + \chi_0 + \frac{\sigma\Delta t}{\varepsilon_0}} \overrightarrow{E}^n + \frac{1}{\varepsilon_\infty + \chi_0 + \frac{\sigma\Delta t}{\varepsilon_0}} \sum_{m=0}^{n-1} \overrightarrow{E}^{n-m}\Delta\chi_m \\ &+ \frac{\Delta t}{\varepsilon_0(\varepsilon_\infty + \chi_0 + \frac{\sigma\Delta t}{\varepsilon_0})} \triangledown \times \overrightarrow{H}|^{n+\frac{1}{2}}\end{aligned} \tag{IV.53}$$

If we propose the relative permittivity ε_r is frequency-independent, for all m, $\chi(\tau) = 0, \varepsilon_\infty = \varepsilon_r, \chi_m = 0$. It is the original Yee formulation.

The solution above is valid for electric dispersive materials. The corresponding solution for magnetically dispersive media is similarly with this.

In Eq. IV.53, we define

$$\overrightarrow{\psi}^n = \sum_{m=0}^{n-1} \overrightarrow{E}^{n-m}\Delta\chi_m \tag{IV.54}$$

Thus at the previous time step, $\overrightarrow{\psi}^{n-1}$ can be presented as

$$\overrightarrow{\psi}^{n-1} = \sum_{m=0}^{n-2} \overrightarrow{E}^{n-1-m} \Delta\chi_m \tag{IV.55}$$

Then, the value of $\overrightarrow{\psi}^{n}$ at present time is evaluated using the value at previous time step by

$$\begin{aligned}
\overrightarrow{\psi}^{n} &= \overrightarrow{E}^{n} \Delta\chi_0 + \sum_{m=1}^{n-1} \overrightarrow{E}^{n-m} \Delta\chi_m \\
&\overset{m-1=k}{=} \overrightarrow{E}^{n} \Delta\chi_0 + \sum_{k=0}^{n-2} \overrightarrow{E}^{n-k-1} \Delta\chi_{k+1} \\
&= \overrightarrow{E}^{n} \Delta\chi_0 + \sum_{m=0}^{n-2} \overrightarrow{E}^{n-m-1} \Delta\chi_{m+1} \\
&= \overrightarrow{E}^{n} \Delta\chi_0 + \frac{\Delta\chi_{m+1}}{\Delta\chi_m} \overrightarrow{\psi}^{n-1}
\end{aligned} \tag{IV.56}$$

Here, $\overrightarrow{\psi}$ can be efficiently evaluated through the use of an recursive accumulator, for easily notation, it can be described as

$$\overrightarrow{\psi}|^{n} = \Delta\chi^{0} \overrightarrow{E}|^{n} + C_{rec} \overrightarrow{\psi}|^{n-1} \tag{IV.57}$$

the coefficient $\Delta\chi^0$ and C_{rec} to be explicated later, they are related to the model we used to the dispersive materials.

IV.2.2 Dispersive models and their numerical implementation

In this part, the Debye, Drude, Lorentz and Critical Points(CP) models and the combination of them are introduced in conjunction with the FDTD algorithm through the recursive convolution method.

IV.2.2.1 Debye model

Debye media are described by a complexional frequency-domain susceptibility function $\chi(\omega)$, at seperate frequency, it has one or more real poles. For a single-pole Debye medium, the susceptibility function $\chi(\omega)$:

$$\chi_p(\omega) = \frac{\varepsilon_{s,p} - \varepsilon_{\infty,p}}{1 - i\omega\tau_p} = \frac{\Delta\varepsilon_p}{1 - i\omega\tau_p} \tag{IV.58}$$

where

$\varepsilon_{s,p}$: the zero-frequency or the static relative permittivity,

$\varepsilon_{\infty,p}$: the infinite frequency relative permittivity,

$\Delta\omega_p$: the change in relative permittivity due to the Debye pole,

τ_p : the pole relaxation time.

In response, the real-valued time-domain susceptibility function $\chi(t)$ is given by inverse Fourier transformation of Eq. IV.58, producing the decaying exponential function

$$\chi_p(t) = \frac{\Delta\varepsilon_p}{\tau_p} e^{-t/\tau_p} U(t) \tag{IV.59}$$

where $U(t)$ is the unit step, and

$$\begin{aligned} \chi_p^0 &= \Delta\varepsilon_p(1 - e^{-\Delta t/\tau_p}) \\ \Delta\chi_p^0 &= \Delta\varepsilon_p(1 - e^{-\Delta t/\tau_p})^2 \\ C_{rec} &= e^{-\Delta t/\tau_p} \end{aligned} \tag{IV.60}$$

Moreover, for a Debye medium with P poles, we express the relative permittivity as

$$\varepsilon(\omega) = \varepsilon_\infty + \sum_{p=1}^{P} \frac{\Delta\varepsilon_p}{1 - i\omega\tau_p} \tag{IV.61}$$

IV.2.2.2 Drude model

At the macroscopic scale, the Drude model has become widely used for treating electromagnetic wave interactions with metals using a dispersive formulation to properly account for the physics of internal electron motion, for a single-pole Drude medium, we have

$$\chi_p(\omega) = -\frac{\omega_p^2}{\omega^2 + i\omega\gamma_p} = -\frac{\omega_p^2/\gamma_p}{\gamma_p - i\omega} - \frac{\omega_p^2/\gamma_p}{i\omega} = -\frac{\omega_p^2/\gamma^2}{1 - i\omega/\gamma_p} + i\frac{\omega_p^2/\gamma_p}{\omega} \tag{IV.62}$$

where

ω_p : the Drude pole frequency,

γ_p : the inverse of the pole relaxation time,

$\chi(t)$ is the real-valued time-domain susceptibility function,

$\chi(t)$ is described by

$$\chi_p(t) = \frac{\omega_p^2}{\gamma_p}(1 - e^{-\gamma_p t})U(t) \tag{IV.63}$$

Consequently ;

$$\begin{aligned} \chi_p^0 &= -\frac{\omega_p^2}{\gamma_p^2}(1 - e^{-\gamma_p \Delta t}) \\ \Delta\chi_p^0 &= -\frac{\omega_p^2}{\gamma_p^2}(1 - e^{-\gamma_p \Delta t})^2 \\ C_{rec} &= e^{-\gamma_p \Delta t} \end{aligned} \tag{IV.64}$$

For a Drude medium with P poles, we express the relative permittivity as

$$\varepsilon(\omega) = \varepsilon_\infty - \sum_{p=1}^{P} \frac{\omega_p^2}{\omega^2 + i\omega\gamma_p} \tag{IV.65}$$

IV.2.2.3 Lorentz model

This model corresponds to inter-band electric transitions, for a Lorentz medium characterized by a single pole pair, the complex-valued, frequency-domain susceptibility function $\chi(\omega)$ can be written as

$$\chi_p(\omega) = \frac{\Delta\varepsilon_p \omega_p^2}{\omega_p^2 - 2i\omega\delta_p - \omega^2} \tag{IV.66}$$

where

$\Delta\varepsilon_p = \varepsilon_{s,p} - \varepsilon_{\infty,p}$: the change in relative permitivity due to the Lorentz pole pair,

ω_p : the frequency of the pole pair,

δ_p : the damping coefficient.

The real-valued time-domain susceptibility function $\chi(t)$ is given by

$$\chi_p(t) = \frac{\Delta\varepsilon_p \omega_p^2}{\sqrt{\omega_p^2 - \delta_p^2}} e^{-\delta_p t} sin(\sqrt{\omega_p^2} t) U(t) \tag{IV.67}$$

After introducing $\alpha = \Gamma_L/2$, $\beta = \sqrt{\Omega_L^2 - \alpha^2}$ and $\eta = \Delta\varepsilon_p \Omega_L^2/\beta$, here Γ_L is the damping coefficient. Ω_L is the polarization frequency(undamped resonant frequency of the medium). Then we can write

$$\chi(t) = \eta e^{-\alpha t} sin(\beta t) U(t) \tag{IV.68}$$

$\chi(t)$ does not have the right properties to be used in the recursive accumulator method, hence we need to define a new quantity $\hat{\chi}(t)$ with the required properties.

$$\hat{\chi}(t) = -i\eta e^{(-\alpha + i\beta)t} U(t) \tag{IV.69}$$

It can be verified that $\chi(t) = R(\hat{\chi}(t))$, we finally get

$$\begin{aligned}
\hat{\chi}^0 &= -i\frac{\eta}{\alpha - i\beta}(1 - e^{(-\alpha+i\beta)\Delta t}), \\
\Delta\hat{\chi}^0 &= -i\frac{\eta}{\alpha - i\beta}(1 - e^{(-\alpha+i\beta)\Delta t})^2, \\
C_{rec} &= e^{(-\alpha+i\beta)\Delta t}
\end{aligned} \tag{IV.70}$$

For a Lorentz medium with P pole pairs, we express the relative permittivity as

$$\varepsilon(\omega) = \varepsilon_\infty + \sum_{p=1}^{P} \frac{\Delta\varepsilon_p \omega_p^2}{\omega_p^2 - 2i\omega\delta_p - \omega^2} \tag{IV.71}$$

IV.2.2.4 Critical Points Model

Critical points model are characterized by a complex-valued, frequency-domain susceptibility function$\chi(\omega)$. And it is defined as

$$\chi(\omega) = \varepsilon(\omega) - \varepsilon_\infty = A\Omega(\frac{e^{i\phi}}{\Omega - \omega - i\Gamma} + \frac{e^{-i\phi}}{\Omega + \omega + i\Gamma}) \tag{IV.72}$$

The real-valued time-domain susceptibility function $\chi(t)$ is described as

$$\begin{aligned}
\chi(t) &= 2A\Omega(cos\phi e^{-\Gamma t} sin(\Omega t) - sin\phi e^{-\Gamma t} cos(\Omega t))U(t) \\
&= 2A\Omega e^{-\Gamma t} sin(\Omega t - \phi)U(t)
\end{aligned} \tag{IV.73}$$

Eq. IV.73 has a form closed to the Fourier transform of a Lorentz term in Eq. IV.68, therefore, a similar procedure is used as those with Lorentz model.

To modify an existing algorithm based on the Lorentz model, the constants α, β and η, as defined as in the Lorentz model, are changed simply by $\alpha = \Gamma$, $\beta = \Omega$ and $\eta = 2A\Omega e^{-i\phi}$.

IV.2.2.5 Combination models

The models previously described may be used in combination with each others, For example, if we use a combination of Drude and Lorentz models, the permittivity is defined as

$$\varepsilon_{DL}(\omega) = \varepsilon_\infty - \frac{\omega_D^2}{\omega^2 + i\gamma\omega} + \sum_m A_m \frac{\Omega_m^2}{\Omega_m^2 - \omega^2 - i\Gamma_m\omega} \tag{IV.74}$$

Similarly, we can combine the Drude and Critical Points models

$$\varepsilon_{DCP}(\omega) = \varepsilon_\infty - \frac{\omega_D^2}{\omega^2 + i\gamma\omega} + \sum_m A_m\Omega_m\left(\frac{e^{i\phi_m}}{\Omega_m - \omega - i\Gamma_m} + \frac{e^{-i\phi_m}}{\Omega_m + \omega + i\Gamma_m}\right) \tag{IV.75}$$

here, $\overrightarrow{\psi}$ in Eq. IV.57 has to be redefined and updated using

$$\chi^0 = \chi_D^0 + R\left(\sum_m \hat{\chi}_m^0\right) \tag{IV.76}$$

The update equation for $\overrightarrow{E}$ can be finally written as

$$\begin{aligned}\overrightarrow{E}|^{n+1} =& \frac{\varepsilon_\infty}{\varepsilon_\infty + \chi^0 + \frac{\sigma\Delta t}{\varepsilon_0}}\overrightarrow{E}|^n + \frac{\Delta t}{\varepsilon_0(\varepsilon_\infty + \chi^0 + \frac{\sigma\Delta t}{\varepsilon_0})}\overrightarrow{\nabla} \times \overrightarrow{H}|^{n+1/2} \\ &+ \frac{1}{\varepsilon_\infty + \chi^0 + \frac{\sigma\Delta t}{\varepsilon_0}}\left(\overrightarrow{\psi}_D|^n + R\sum_m \hat{\overrightarrow{\psi}}_m|^n\right)\end{aligned} \tag{IV.77}$$

Depending on the material to study and the range of wavelengths of interest, the model and the number of terms could be chosen arbitrarily. The important condition should be noted in order to make sure the convergence of the FDTD algorithm.

$$\left|\frac{\varepsilon_\infty}{\varepsilon_\infty + \chi^0 + \frac{\sigma\Delta t}{\varepsilon_0}}\right| < 1 \tag{IV.78}$$

where χ^0 is defined by the Eq. IV.76.

The Yee equation for H will be unchanged for non-magnetic media. And in our work, the Drude-2CP model is used to describe the dispersive properties of gold nanoparticles.

IV.3 FDTD algorithm for anisotropic materials

In the sections before, we have investigated the original FDTD algorithm and the derivative forms for dispersive materials. In this part, we will present the FDTD algorithm we used for anisotropic materials.

IV.3.1 The deduction of FDTD algorithm

For a region with no charges (ρ= 0) and no currents ($\overrightarrow{J}$ = 0), but having materials that absorb electric or magnetic field energy, Maxwell's equations reduce to :

$$\begin{aligned}
\overrightarrow{\nabla} \times \overrightarrow{E} &= -\frac{\partial \overrightarrow{B}}{\partial t} \\
\overrightarrow{\nabla} \times \overrightarrow{H} &= \frac{\partial \overrightarrow{D}}{\partial t} \\
\overrightarrow{\nabla} \bullet \overrightarrow{D} &= 0 \\
\overrightarrow{\nabla} \bullet \overrightarrow{B} &= 0
\end{aligned} \tag{IV.79}$$

As we consider nematic liquid crystals as non-magnetic materials, the anisotropic properties can be realized by relationships of the electric field versus electric flux with the permittivity tensor $\widetilde{\varepsilon}$. Constitutive relations can be written as

$$\overrightarrow{B} = \mu_0 \overrightarrow{H} \tag{IV.80}$$

$$\overrightarrow{D} = \widetilde{\varepsilon} \overrightarrow{E} \tag{IV.81}$$

where μ_0 is the permeability of free space. $\widetilde{\varepsilon}$ is the permittivity tensor, which can be written as follows

$$\widetilde{\varepsilon} = \begin{bmatrix} \varepsilon_{xx} & \varepsilon_{xy} & \varepsilon_{xz} \\ \varepsilon_{yx} & \varepsilon_{yy} & \varepsilon_{yz} \\ \varepsilon_{zx} & \varepsilon_{zy} & \varepsilon_{zz} \end{bmatrix} \tag{IV.82}$$

For this case, the Maxwell's curl equations are described as

$$\bigtriangledown \times \overrightarrow{E} = -\mu_0 \frac{\partial \overrightarrow{H}}{\partial t} \tag{IV.83}$$

$$\bigtriangledown \times \overrightarrow{H} = \widetilde{\varepsilon} \frac{\partial \overrightarrow{E}}{\partial t} \tag{IV.84}$$

It is convenient to introduce the inverse of the permittivity tensor as $\widetilde{\zeta} = \widetilde{\varepsilon}^{-1}$,

$$\widetilde{\zeta} = \begin{bmatrix} \zeta_{xx} & \zeta_{xy} & \zeta_{xz} \\ \zeta_{yx} & \zeta_{yy} & \zeta_{yz} \\ \zeta_{zx} & \zeta_{zy} & \zeta_{zz} \end{bmatrix} \tag{IV.85}$$

Thus, in nonconductor anisotropic media, the Maxwell's curl equations can be written as [96]

$$\bigtriangledown \times \overrightarrow{E} = -\mu_0 \frac{\partial \overrightarrow{H}}{\partial t} \tag{IV.86}$$

$$\widetilde{\zeta} \bigtriangledown \times \overrightarrow{H} = \frac{\partial \overrightarrow{E}}{\partial t} \tag{IV.87}$$

In Cartesian coordinates, we write out the vector components of the curl operators of Faraday's law (Eq. IV.86) as follows.

$$\begin{aligned}\frac{\partial H_x}{\partial t} &= \frac{1}{\mu_0}(\frac{\partial E_y}{\partial z} - \frac{\partial E_z}{\partial y})\\ \frac{\partial H_y}{\partial t} &= \frac{1}{\mu_0}(\frac{\partial E_z}{\partial x} - \frac{\partial E_x}{\partial z})\\ \frac{\partial H_z}{\partial t} &= \frac{1}{\mu_0}(\frac{\partial E_x}{\partial y} - \frac{\partial E_y}{\partial x})\end{aligned} \tag{IV.88}$$

For Ampere's law(Eq. IV.87), it can be written as

$$\begin{aligned}\frac{\partial E_x}{\partial t} &= \zeta_{xx}(\frac{\partial H_z}{\partial y} - \frac{\partial H_y}{\partial z}) + \zeta_{xy}(\frac{\partial H_x}{\partial z} - \frac{\partial H_z}{\partial x}) + \zeta_{xz}(\frac{\partial H_y}{\partial x} - \frac{\partial H_x}{\partial y})\\ \frac{\partial E_y}{\partial t} &= \zeta_{yx}(\frac{\partial H_z}{\partial y} - \frac{\partial H_y}{\partial z}) + \zeta_{yy}(\frac{\partial H_x}{\partial z} - \frac{\partial H_z}{\partial x}) + \zeta_{yz}(\frac{\partial H_y}{\partial x} - \frac{\partial H_x}{\partial y})\\ \frac{\partial E_z}{\partial t} &= \zeta_{zx}(\frac{\partial H_z}{\partial y} - \frac{\partial H_y}{\partial z}) + \zeta_{zy}(\frac{\partial H_x}{\partial z} - \frac{\partial H_z}{\partial x}) + \zeta_{zz}(\frac{\partial H_y}{\partial x} - \frac{\partial H_x}{\partial y})\end{aligned} \tag{IV.89}$$

On the right-hand side of Eq. IV.89, for each components(x, y, z), three derivatives exist. which we separately call first, second, and third class derivatives.

x-components of Eq. IV.89 for example.

First class derivatives : $\frac{\partial H_z}{\partial y}$ and $\frac{\partial H_y}{\partial z}$, they are multiplied by ζ_{xx}, which is the diagonal element of ζ, it is the same as the one in the isotropic materials or ζ with diagonal.

Second class derivatives : $\frac{\partial H_x}{\partial z}$ and $\frac{\partial H_z}{\partial x}$, they are multiplied by ζ_{xy}, which are the derived magnetic components in z or x-direction.

Third class derivatives : $\frac{\partial H_y}{\partial x}$ and $\frac{\partial H_x}{\partial y}$, they are multiplied by ζ_{xz}, which are the derived magnetic components in x or y-direction.

Using the FDTD algorithm and considering the absorbing boundary conditions, for the non-magnetic materials LCs, $\sigma^* = 0$. Assuming magnetic current source $M_{source} =$

0. x-component of Eq. IV.88 for instance is

$$\begin{aligned} H_x|^{n+1/2}_{i,j+1/2,k+1/2} &= H_x|^{n-1/2}_{i,j+1/2,k+1/2} \\ &- \frac{dt}{\mu_0}\Big(\frac{E_z|^n_{i,j+1,k+1/2} - E_z|^n_{i,j,k+1/2}}{k_{y|i,j+1/2,k+1/2}dy} - \frac{E_y|^n_{i,j+1/2,k+1} - E_y|^n_{i,j+1/2,k}}{k_{z|i,j+1/2,k+1/2}dz} \\ &+ \psi_{H_{xy}}|^n_{i,j+1/2,k+1/2} - \psi_{H_{xz}}|^n_{i,j+1/2,k+1/2}\Big) \end{aligned} \tag{IV.90}$$

where

$$\begin{aligned} \psi_{H_{xy}}|^n_{i,j+1/2,k+1/2} &= b_{y|i,j+1/2,k+1/2}\psi_{H_{xy}}|^{n-1}_{i,j+1/2,k+1/2} + c_{y|i,j+1/2,k+1/2}\Big(\frac{E_z|^n_{i,j+1,k+1/2} - E_z|^n_{i,j,k+1/2}}{dy}\Big) \\ \psi_{H_{xz}}|^n_{i,j+1/2,k+1/2} &= b_{z|i,j+1/2,k+1/2}\psi_{H_{xz}}|^{n-1}_{i,j+1/2,k+1/2} + c_{z|i,j+1/2,k+1/2}\Big(\frac{E_y|^n_{i,j+1/2,k+1} - E_y|^n_{i,j+1/2,k}}{dz}\Big) \end{aligned} \tag{IV.91}$$

$$\begin{aligned} b_w &= e^{-(\frac{\sigma_w}{\varepsilon_0 k_w} + \frac{a_w}{\varepsilon_0})dt} \\ c_w &= \frac{\sigma_w}{\sigma_w k_w + k_w^2 a_w}\Big(e^{-(\frac{\sigma_w}{\varepsilon_0 k_w} + \frac{a_w}{\varepsilon_0})dt} - 1\Big) \end{aligned} \tag{IV.92}$$

Here, CPML is used for the absorbing boundary conditions. That is introduced in 1.1.4. We can compare the Eq. IV.38 with Eq. IV.90.

Note that the discrete coefficients b_w and c_w are non-zero only in PML regions with w-normal interface boundaries.

For non-conductive materials LCs $\sigma = 0$, no electric current sources$J = 0$; x-component of Eq. IV.89 using the FDTD algorithm and CPML bondary conditions at

points $(i\Delta x,\, j\Delta y,\, k\Delta z)$ and the times $t = (n + 1/2)\Delta t$

$$
\begin{aligned}
E_x|^{n+1}_{i+1/2,j,k} &= E_x|^{n}_{i+1/2,j,k} \\
&+ dt\zeta_{xx}\Big(\frac{H_z|^{n+1/2}_{i+1/2,j+1/2,k} - H_z|^{n+1/2}_{i+1/2,j-1/2,k}}{k_y dy} - \frac{H_y|^{n+1/2}_{i+1/2,j,k+1/2} - H_y|^{n+1/2}_{i+1/2,j,k-1/2}}{k_z dz} \\
&+ \psi_{E_{xxy}|^{n}_{i+1/2,j,k}} - \psi_{E_{xxz}|^{n}_{i+1/2,j,k}}\Big) \\
&+ dt\zeta_{xy}\Big(\frac{H_x|^{n+1/2}_{i+1/2,j,k+1/2} - H_x|^{n+1/2}_{i+1/2,j,k-1/2}}{k_z dz} - \frac{H_z|^{n+1/2}_{i+1,j,k} - H_z|^{n+1/2}_{i,j,k}}{k_x dx} \\
&+ \psi_{E_{xyz}|^{n}_{i+1/2,j,k}} - \psi_{E_{xyx}|^{n}_{i+1/2,j,k}}\Big) \\
&+ dt\zeta_{xz}\Big(\frac{H_y|^{n+1/2}_{i+1,j,k} - H_y|^{n+1/2}_{i,j,k}}{k_x dx} - \frac{H_x|^{n+1/2}_{i+1/2,j+1/2,k} - H_x|^{n+1/2}_{i+1/2,j-1/2,k}}{k_y dy} \\
&+ \psi_{E_{xzx}|^{n}_{i+1/2,j,k}} - \psi_{E_{xzy}|^{n}_{i+1/2,j,k}}\Big)
\end{aligned}
\tag{IV.93}
$$

where

$$
\begin{aligned}
\psi_{E_{xxy}}|^{n}_{i+1/2,j,k} &= b_{y|i+1/2,j,k}\psi_{E_{xxy}}|^{n-1}_{i+1/2,j,k} + c_{y|i+1/2,j,k}\Big(\frac{H_z|^{n+1/2}_{i+1/2,j+1/2,k} - H_z|^{n+1/2}_{i+1/2,j-1/2,k}}{dy}\Big) \\
\psi_{E_{xxz}}|^{n}_{i+1/2,j,k} &= b_{z|i+1/2,j,k}\psi_{E_{xxz}}|^{n-1}_{i+1/2,j,k} + c_{z|i+1/2,j,k}\Big(\frac{H_y|^{n+1/2}_{i+1/2,j,k+1/2} - H_y|^{n+1/2}_{i+1/2,j,k-1/2}}{dz}\Big) \\
\psi_{E_{xyz}}|^{n}_{i+1/2,j,k} &= b_{z|i+1/2,j,k}\psi_{E_{xyz}}|^{n-1}_{i+1/2,j,k} + c_{z|i+1/2,j,k}\Big(\frac{H_x|^{n+1/2}_{i+1/2,j,k+1/2} - H_x|^{n+1/2}_{i+1/2,j,k-1/2}}{dz}\Big) \\
\psi_{E_{xyx}}|^{n}_{i+1/2,j,k} &= b_{x|i+1/2,j,k}\psi_{E_{xyx}}|^{n-1}_{i+1/2,j,k} + c_{x|i+1/2,j,k}\Big(\frac{H_z|^{n+1/2}_{i+1,j,k} - H_z|^{n+1/2}_{i,j,k}}{dx}\Big) \\
\psi_{E_{xzx}}|^{n}_{i+1/2,j,k} &= b_{x|i+1/2,j,k}\psi_{E_{xzx}}|^{n-1}_{i+1/2,j,k} + c_{x|i+1/2,j,k}\Big(\frac{H_y|^{n+1/2}_{i+1,j,k} - H_y|^{n+1/2}_{i,j,k}}{dx}\Big) \\
\psi_{E_{xzy}}|^{n}_{i+1/2,j,k} &= b_{z|i+1/2,j,k}\psi_{E_{xzy}}|^{n-1}_{i+1/2,j,k} + c_{z|i+1/2,j,k}\Big(\frac{H_x|^{n+1/2}_{i+1/2,j+1/2,k} - H_x|^{n+1/2}_{i+1/2,j-1/2,k}}{dy}\Big)
\end{aligned}
\tag{IV.94}
$$

Here, b_w and $c_w, w = x, y, z$ follows the definition in Eq. IV.92. They are non-zero only in PML regions with w-normal interface boundaries also.

In the derivative Eq. IV.93 and Eq. IV.94, only the first class derivative elements actually are present in Yee's grid(see Fig. IV.2), using basic centered differentiation operator, $H_x|^{n+1/2}_{i+1/2,j,k+1/2} = \dfrac{H_x|^{n+1/2}_{i+1,j,k+1/2} + H_x|^{n+1/2}_{i,j,k+1/2}}{2}$

Other elements are described as

$$
\begin{aligned}
H_x|^{n+1/2}_{i+1/2,j,k+1/2} &= \frac{1}{4}(H_x|^{n+1/2}_{i+1,j+1/2,k+1/2} + H_x|^{n+1/2}_{i+1,j-1/2,k+1/2} + H_x|^{n+1/2}_{i,j+1/2,k+1/2} + H_x|^{n+1/2}_{i,j-1/2,k+1/2}) \\
H_x|^{n+1/2}_{i+1/2,j,k-1/2} &= \frac{1}{4}(H_x|^{n+1/2}_{i+1,j+1/2,k-1/2} + H_x|^{n+1/2}_{i+1,j-1/2,k-1/2} + H_x|^{n+1/2}_{i,j+1/2,k-1/2} + H_x|^{n+1/2}_{i,j-1/2,k-1/2}) \\
H_z|^{n+1/2}_{i+1,j,k} &= \frac{1}{4}(H_z|^{n+1/2}_{i+3/2,j+1/2,k} + H_z|^{n+1/2}_{i+3/2,j-1/2,k} + H_z|^{n+1/2}_{i+1/2,j+1/2,k} + H_z|^{n+1/2}_{i+1/2,j-1/2,k}) \\
H_z|^{n+1/2}_{i,j,k} &= \frac{1}{4}(H_x|^{n+1/2}_{i+1/2,j+1/2,k} + H_z|^{n+1/2}_{i+1/2,j-1/2,k} + H_z|^{n+1/2}_{i-1/2,j+1/2,k} + H_z|^{n+1/2}_{i-1/2,j-1/2,k}) \\
H_y|^{n+1/2}_{i+1,j,k} &= \frac{1}{4}(H_y|^{n+1/2}_{i+3/2,j,k+1/2} + H_y|^{n+1/2}_{i+3/2,j,k-1/2} + H_y|^{n+1/2}_{i+1/2,j,k+1/2} + H_y|^{n+1/2}_{i+1/2,j,k-1/2}) \\
H_y|^{n+1/2}_{i,j,k} &= \frac{1}{4}(H_y|^{n+1/2}_{i+1/2,j,k+1/2} + H_y|^{n+1/2}_{i+1/2,j,k-1/2} + H_y|^{n+1/2}_{i-1/2,j,k+1/2} + H_y|^{n+1/2}_{i-1/2,j,k-1/2}) \\
H_x|^{n+1/2}_{i+1/2,j+1/2,k} &= \frac{1}{4}(H_x|^{n+1/2}_{i+1,j+1/2,k+1/2} + H_x|^{n+1/2}_{i+1,j+1/2,k-1/2} + H_x|^{n+1/2}_{i,j+1/2,k+1/2} + H_x|^{n+1/2}_{i,j+1/2,k-1/2}) \\
H_x|^{n+1/2}_{i+1/2,j-1/2,k} &= \frac{1}{4}(H_x|^{n+1/2}_{i+1,j-1/2,k+1/2} + H_x|^{n+1/2}_{i+1,j-1/2,k-1/2} + H_x|^{n+1/2}_{i,j-1/2,k+1/2} + H_x|^{n+1/2}_{i,j-1/2,k-1/2})
\end{aligned}
\tag{IV.95}
$$

Similarly, the other elements Hy and Hz can be written as follows. y-component of Eq. IV.88 is

$$
\begin{aligned}
H_y|^{n+1/2}_{i+1/2,j,k+1/2} &= H_y|^{n-1/2}_{i+1/2,j,k+1/2} \\
&- \frac{dt}{\mu_0}(\frac{E_x|^n_{i+1/2,j,k+1} - E_x|^n_{i+1/2,j,k}}{k_{z|i+1/2,j,k+1/2}dz} - \frac{E_z|^n_{i+1,j,k+1/2} - E_z|^n_{i,j,k+1/2}}{k_{x|i+1/2,j,k+1/2}dx} \\
&+ \psi_{H_{yz}}|^n_{i+1/2,j,k+1/2} - \psi_{H_{yx}}|^n_{i+1/2,j,k+1/2})
\end{aligned}
\tag{IV.96}
$$

where

$$
\begin{aligned}
\psi_{H_{yz}}|^n_{i+1/2,j,k+1/2} &= b_{z|i+1/2,j,k+1/2}\psi_{H_{yz}}|^{n-1}_{i+1/2,j,k+1/2} + c_{z|i+1/2,j,k+1/2}(\frac{E_x|^n_{i+1/2,j,k+1} - E_x|^n_{i+1/2,j,k}}{dz}) \\
\psi_{H_{yx}}|^n_{i+1/2,j,k+1/2} &= b_{x|i+1/2,j,k+1/2}\psi_{H_{yx}}|^{n-1}_{i+1/2,j,k+1/2} + c_{x|i+1/2,j,k+1/2}(\frac{E_z|^n_{i+1,j,k+1/2} - E_z|^n_{i,j,k+1/2}}{dx})
\end{aligned}
\tag{IV.97}
$$

z-component of Eq. IV.88 is

$$
\begin{aligned}
H_z|^{n+1/2}_{i+1/2,j+1/2,k} &= H_z|^{n-1/2}_{i+1/2,j+1/2,k} \\
&- \frac{dt}{\mu_0}\Big(\frac{E_y|^n_{i+1,j+1/2,k} - E_y|^n_{i,j+1/2,k}}{k_{x|i+1/2,j+1/2,k}dx} - \frac{E_x|^n_{i+1/2,j+1,k} - E_x|^n_{i+1/2,j,k}}{k_{y|i+1/2,j+1/2,k}dy} \\
&+ \psi_{H_{zx}}|^n_{i+1/2,j+1/2,k} - \psi_{H_{zy}}|^n_{i+1/2,j+1/2,k}\Big)
\end{aligned}
\tag{IV.98}
$$

where

$$
\begin{aligned}
\psi_{H_{zx}}|^n_{i+1/2,j+1/2,k} &= b_{x|i+1/2,j+1/2,k}\psi_{H_{zx}}|^{n-1}_{i+1/2,j+1/2,k} + c_{x|i+1/2,j+1/2,k}\Big(\frac{E_y|^n_{i+1,j+1/2,k} - E_y|^n_{i,j+1/2,k}}{dx}\Big) \\
\psi_{H_{zy}}|^n_{i+1/2,j+1/2,k} &= b_{x|i+1/2,j+1/2,k}\psi_{H_{zy}}|^{n-1}_{i+1/2,j+1/2,k} + c_{y|i+1/2,j+1/2,k}\Big(\frac{E_x|^n_{i+1/2,j+1,k} - E_x|^n_{i+1/2,j,k}}{dy}\Big)
\end{aligned}
\tag{IV.99}
$$

y-component of Eq. IV.89 is

$$
\begin{aligned}
E_y|^{n+1}_{i,j+1/2,k} &= E_y|^n_{i,j+1/2,k} \\
&+ dt\zeta_{yx}\Big(\frac{H_z|^{n+1/2}_{i,j+1,k} - H_z|^{n+1/2}_{i,j,k}}{k_y dy} - \frac{H_y|^{n+1/2}_{i,j+1/2,k+1/2} - H_y|^{n+1/2}_{i,j+1/2,k-1/2}}{k_z dz} \\
&+ \psi_{E_{yxy}|^n_{i,j+1/2,k}} - \psi_{E_{yxz}|^n_{i,j+1/2,k}}\Big) \\
&+ dt\zeta_{yy}\Big(\frac{H_x|^{n+1/2}_{i,j+1/2,k+1/2} - H_x|^{n+1/2}_{i,j+1/2,k-1/2}}{k_z dz} - \frac{H_z|^{n+1/2}_{i+1/2,j+1/2,k} - H_z|^{n+1/2}_{i-1/2,j+1/2,k}}{k_x dx} \\
&+ \psi_{E_{yyz}|^n_{i,j+1/2,k}} - \psi_{E_{yyx}|^n_{i,j+1/2,k}}\Big) \\
&+ dt\zeta_{yz}\Big(\frac{H_y|^{n+1/2}_{i+1/2,j+1/2,k} - H_y|^{n+1/2}_{i-1/2,j+1/2,k}}{k_x dx} - \frac{H_x|^{n+1/2}_{i,j+1,k} - H_x|^{n+1/2}_{i,j,k}}{k_y dy} \\
&+ \psi_{E_{yzx}|^n_{i,j+1/2,k}} - \psi_{E_{yzy}|^n_{i,j+1/2,k}}\Big)
\end{aligned}
\tag{IV.100}
$$

where

$$
\begin{aligned}
\psi_{E_{yxy}}|^{n}_{i,j+1/2,k} &= b_{y|i,j+1/2,k}\psi_{E_{yxy}}|^{n-1}_{i,j+1/2,k} + c_{y|i,j+1/2,k}(\frac{H_z|^{n+1/2}_{i,j+1,k} - H_z|^{n+1/2}_{i,j,k}}{dy}) \\
\psi_{E_{yxz}}|^{n}_{i,j+1/2,k} &= b_{z|i,j+1/2,k}\psi_{E_{yxz}}|^{n-1}_{i,j+1/2,k} + c_{z|i,j+1/2,k}(\frac{H_y|^{n+1/2}_{i,j+1/2,k+1/2} - H_y|^{n+1/2}_{i,j+1/2,k-1/2}}{dz}) \\
\psi_{E_{yyz}}|^{n}_{i,j+1/2,k} &= b_{z|i,j+1/2,k}\psi_{E_{yyz}}|^{n-1}_{i,j+1/2,k} + c_{z|i,j+1/2,k}(\frac{H_x|^{n+1/2}_{i,j+1/2,k+1/2} - H_x|^{n+1/2}_{i,j+1/2,k-1/2}}{dz}) \\
\psi_{E_{yyx}}|^{n}_{i,j+1/2,k} &= b_{x|i,j+1/2,k}\psi_{E_{yyx}}|^{n-1}_{i,j+1/2,k} + c_{x|i,j+1/2,k}(\frac{H_z|^{n+1/2}_{i+1/2,j+1/2,k} - H_z|^{n+1/2}_{i-1/2,j+1/2,k}}{dx}) \\
\psi_{E_{yzx}}|^{n}_{i,j+1/2,k} &= b_{x|i,j+1/2,k}\psi_{E_{yzx}}|^{n-1}_{i,j+1/2,k} + c_{x|i,j+1/2,k}(\frac{H_y|^{n+1/2}_{i+1/2,j+1/2,k} - H_y|^{n+1/2}_{i-1/2,j+1/2,k}}{dx}) \\
\psi_{E_{yzy}}|^{n}_{i,j+1/2,k} &= b_{z|i,j+1/2,k}\psi_{E_{yzy}}|^{n-1}_{i,j+1/2,k} + c_{z|i,j+1/2,k}(\frac{H_x|^{n+1/2}_{i,j+1,k} - H_x|^{n+1/2}_{i,j,k}}{dy})
\end{aligned}
\tag{IV.101}
$$

Using basic centered differentiation operator for the elements in Eq. IV.100 and Eq. IV.101 which are not described in Fig. IV.2

$$
\begin{aligned}
H_z|^{n+1/2}_{i,j+1,k} &= \frac{1}{4}(H_z|^{n+1/2}_{i+1/2,j+3/2,k} + H_z|^{n+1/2}_{i+1/2,j+1/2,k} + H_z|^{n+1/2}_{i-1/2,j+3/2,k} + H_z|^{n+1/2}_{i-1/2,j+1/2,k}) \\
H_z|^{n+1/2}_{i,j,k} &= \frac{1}{4}(H_x|^{n+1/2}_{i+1/2,j+1/2,k} + H_z|^{n+1/2}_{i+1/2,j-1/2,k} + H_z|^{n+1/2}_{i-1/2,j+1/2,k} + H_z|^{n+1/2}_{i-1/2,j-1/2,k}) \\
H_y|^{n+1/2}_{i,j+1/2,k+1/2} &= \frac{1}{4}(H_y|^{n+1/2}_{i+1/2,j+1,k+1/2} + H_y|^{n+1/2}_{i+1/2,j,k+1/2} + H_y|^{n+1/2}_{i-1/2,j+1,k+1/2} + H_y|^{n+1/2}_{i-1/2,j,k+1/2}) \\
H_y|^{n+1/2}_{i,j+1/2,k-1/2} &= \frac{1}{4}(H_y|^{n+1/2}_{i+1/2,j+1,k-1/2} + H_y|^{n+1/2}_{i+1/2,j,k-1/2} + H_y|^{n+1/2}_{i-1/2,j+1,k-1/2} + H_y|^{n+1/2}_{i-1/2,j,k-1/2}) \\
H_y|^{n+1/2}_{i+1/2,j+1/2,k} &= \frac{1}{4}(H_y|^{n+1/2}_{i+1/2,j+1,k+1/2} + H_y|^{n+1/2}_{i+1/2,j+1,k-1/2} + H_y|^{n+1/2}_{i+1/2,j,k+1/2} + H_y|^{n+1/2}_{i+1/2,j,k-1/2}) \\
H_y|^{n+1/2}_{i-1/2,j+1/2,k} &= \frac{1}{4}(H_y|^{n+1/2}_{i-1/2,j+1,k+1/2} + H_y|^{n+1/2}_{i-1/2,j+1,k-1/2} + H_y|^{n+1/2}_{i-1/2,j,k+1/2} + H_y|^{n+1/2}_{i-1/2,j,k-1/2}) \\
H_x|^{n+1/2}_{i,j+1,k} &= \frac{1}{4}(H_x|^{n+1/2}_{i,j+3/2,k+1/2} + H_x|^{n+1/2}_{i,j+3/2,k-1/2} + H_x|^{n+1/2}_{i,j+1/2,k+1/2} + H_x|^{n+1/2}_{i,j+1/2,k-1/2}) \\
H_x|^{n+1/2}_{i,j,k} &= \frac{1}{4}(H_x|^{n+1/2}_{i,j+1/2,k+1/2} + H_x|^{n+1/2}_{i,j+1/2,k-1/2} + H_x|^{n+1/2}_{i,j-1/2,k+1/2} + H_x|^{n+1/2}_{i,j-1/2,k-1/2})
\end{aligned}
\tag{IV.102}
$$

z-component of Eq. IV.89 is

$$
\begin{aligned}
E_z|_{i,j,k+1/2}^{n+1} &= E_y|_{i,j,k+1/2}^{n} \\
&+ dt\zeta_{zx}\Big(\frac{H_z|_{i,j+1/2,k+1/2}^{n+1/2} - H_z|_{i,j-1/2,k+1/2}^{n+1/2}}{k_y dy} - \frac{H_y|_{i,j,k+1}^{n+1/2} - H_y|_{i,j,k}^{n+1/2}}{k_z dz} \\
&+ \psi_{E_{zxy}|_{i,j,k+1/2}^{n}} - \psi_{E_{zxz}|_{i,j,k+1/2}^{n}}\Big) \\
&+ dt\zeta_{zy}\Big(\frac{H_x|_{i,j,k+1}^{n+1/2} - H_x|_{i,j,k}^{n+1/2}}{k_z dz} - \frac{H_z|_{i+1/2,j,k+1/2}^{n+1/2} - H_z|_{i-1/2,j,k+1/2}^{n+1/2}}{k_x dx} \\
&+ \psi_{E_{zyz}|_{i,j,k+1/2}^{n}} - \psi_{E_{zyx}|_{i,j,k+1/2}^{n}}\Big) \\
&+ dt\zeta_{zz}\Big(\frac{H_y|_{i+1/2,j,k+1/2}^{n+1/2} - H_y|_{i-1/2,j,k+1/2}^{n+1/2}}{k_x dx} - \frac{H_x|_{i,j+1/2,k+1/2}^{n+1/2} - H_x|_{i,j-1/2,k+1/2}^{n+1/2}}{k_y dy} \\
&+ \psi_{E_{zzx}|_{i,j,k+1/2}^{n}} - \psi_{E_{zzy}|_{i,j,k+1/2}^{n}}\Big)
\end{aligned}
\tag{IV.103}
$$

where

$$
\begin{aligned}
\psi_{E_{zxy}}|_{i,j,k+1/2}^{n} &= b_{y|i,j,k+1/2}\psi_{E_{zxy}}|_{i,j,k+1/2}^{n-1} + c_{y|i,j,k+1/2}\Big(\frac{H_z|_{i,j+1/2,k+1/2}^{n+1/2} - H_z|_{i,j-1/2,k+1/2}^{n+1/2}}{dy}\Big) \\
\psi_{E_{zxz}}|_{i,j,k+1/2}^{n} &= b_{z|i,j,k+1/2}\psi_{E_{zxz}}|_{i,j,k+1/2}^{n-1} + c_{z|i,j,k+1/2}\Big(\frac{H_y|_{i,j,k+1}^{n+1/2} - H_y|_{i,j,k}^{n+1/2}}{dz}\Big) \\
\psi_{E_{zyz}}|_{i,j,k+1/2}^{n} &= b_{z|i,j,k+1/2}\psi_{E_{zyz}}|_{i,j,k+1/2}^{n-1} + c_{z|i,j,k+1/2}\Big(\frac{H_x|_{i,j,k+1}^{n+1/2} - H_x|_{i,j,k}^{n+1/2}}{dz}\Big) \\
\psi_{E_{zyx}}|_{i,j,k+1/2}^{n} &= b_{x|i,j,k+1/2}\psi_{E_{zyx}}|_{i,j,k+1/2}^{n-1} + c_{x|i,j,k+1/2}\Big(\frac{H_z|_{i+1/2,j,k+1/2}^{n+1/2} - H_z|_{i-1/2,j,k+1/2}^{n+1/2}}{dx}\Big) \\
\psi_{E_{zzx}}|_{i,j,k+1/2}^{n} &= b_{x|i,j,k+1/2}\psi_{E_{zzx}}|_{i,j,k+1/2}^{n-1} + c_{x|i,j,k+1/2}\Big(\frac{H_y|_{i+1/2,j,k+1/2}^{n+1/2} - H_y|_{i-1/2,j,k+1/2}^{n+1/2}}{dx}\Big) \\
\psi_{E_{zzy}}|_{i,j,k+1/2}^{n} &= b_{z|i,j,k+1/2}\psi_{E_{zzy}}|_{i,j,k+1/2}^{n-1} + c_{z|i,j,k+1/2}\Big(\frac{H_x|_{i,j+1/2,k+1/2}^{n+1/2} - H_x|_{i,j-1/2,k+1/2}^{n+1/2}}{dy}\Big)
\end{aligned}
\tag{IV.104}
$$

Using basic centered differentiation operator for the elements in Eq. IV.103 and Eq. IV.104 which are not described in Fig. IV.2

$$
\begin{aligned}
H_z|_{i,j+1/2,k+1/2}^{n+1/2} &= \frac{1}{4}(H_z|_{i+1/2,j+1/2,k+1}^{n+1/2} + H_z|_{i+1/2,j+1/2,k}^{n+1/2} + H_z|_{i-1/2,j+1/2,k+1}^{n+1/2} + H_z|_{i-1/2,j+1/2,k}^{n+1/2}) \\
H_z|_{i,j-1/2,k+1/2}^{n+1/2} &= \frac{1}{4}(H_x|_{i+1/2,j-1/2,k+1}^{n+1/2} + H_z|_{i+1/2,j-1/2,k}^{n+1/2} + H_z|_{i-1/2,j-1/2,k+1}^{n+1/2} + H_z|_{i-1/2,j-1/2,k}^{n+1/2}) \\
H_y|_{i,j,k+1}^{n+1/2} &= \frac{1}{4}(H_y|_{i+1/2,j,k+3/2}^{n+1/2} + H_y|_{i+1/2,j,k+1/2}^{n+1/2} + H_y|_{i-1/2,j+1,k+3/2}^{n+1/2} + H_y|_{i-1/2,j,k+1/2}^{n+1/2}) \\
H_y|_{i,j,k}^{n+1/2} &= \frac{1}{4}(H_y|_{i+1/2,j,k+1/2}^{n+1/2} + H_y|_{i+1/2,j,k-1/2}^{n+1/2} + H_y|_{i-1/2,j,k+1/2}^{n+1/2} + H_y|_{i-1/2,j,k-1/2}^{n+1/2}) \\
H_x|_{i,j,k+1}^{n+1/2} &= \frac{1}{4}(H_x|_{i,j+1/2,k+3/2}^{n+1/2} + H_x|_{i,j+1/2,k+1/2}^{n+1/2} + H_x|_{i,j-1/2,k+3/2}^{n+1/2} + H_x|_{i,j-1/2,k+1/2}^{n+1/2}) \\
H_x|_{i,j,k}^{n+1/2} &= \frac{1}{4}(H_x|_{i,j+1/2,k+1/2}^{n+1/2} + H_x|_{i,j+1/2,k-1/2}^{n+1/2} + H_x|_{i,j-1/2,k+1/2}^{n+1/2} + H_x|_{i,j-1/2,k-1/2}^{n+1/2}) \\
H_z|_{i+1/2,j,k+1/2}^{n+1/2} &= \frac{1}{4}(H_z|_{i+1/2,j+1/2,k+1}^{n+1/2} + H_z|_{i+1/2,j+1/2,k}^{n+1/2} + H_z|_{i+1/2,j-1/2,k+1}^{n+1/2} + H_z|_{i+1/2,j-1/2,k}^{n+1/2}) \\
H_z|_{i-1/2,j,k+1/2}^{n+1/2} &= \frac{1}{4}(H_z|_{i-1/2,j+1/2,k+1}^{n+1/2} + H_z|_{i-1/2,j+1/2,k}^{n+1/2} + H_z|_{i-1/2,j-1/2,k+1}^{n+1/2} + H_z|_{i-1/2,j-1/2,k}^{n+1/2})
\end{aligned}
\tag{IV.105}
$$

IV.3.2 FDTD algorithm responding to my code

In the particular case of an optical axis of the nematic liquid crystal molecules in the X-Z plane, we define θ as the angle between the optical axis and $\overrightarrow{x}$. The Fig. IV.4 described the orientation of LC molecules.

The permittivity tensor elements are given by Eq. IV.106

$$
\begin{aligned}
\varepsilon_{xx} &= \varepsilon_o(n_o^2 \sin^2\theta + n_e^2 \cos^2\theta) \\
\varepsilon_{yy} &= \varepsilon_o n_o^2 \\
\varepsilon_{zz} &= \varepsilon_o(n_o^2 \cos^2\theta + n_e^2 \sin^2\theta) \\
\varepsilon_{xz} &= \varepsilon_{zx} = \varepsilon_o(n_o^2 - n_e^2)\sin\theta\cos\theta \\
\varepsilon_{xy} &= \varepsilon_{yx} = \varepsilon_{yz} = \varepsilon_{zy} = 0
\end{aligned}
\tag{IV.106}
$$

In response, the inverse of the permittivity tensor

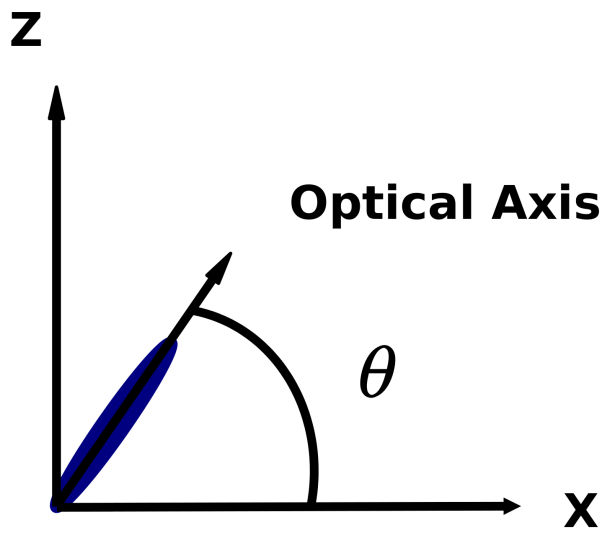

Fig. IV.4 – Orientation of LC molecules

$$
\begin{aligned}
\zeta_{xx} &= \frac{n_o^2 \cos^2\theta + n_e^2 \sin^2\theta}{\varepsilon_0 n_o^2 n_e^2} \\
\zeta_{yy} &= \frac{1}{\varepsilon_0 n_o^2} \\
\zeta_{zz} &= \frac{n_o^2 \sin^2\theta + n_e^2 \cos^2\theta}{\varepsilon_0 n_o^2 n_e^2} \\
\zeta_{xz} = \zeta_{zx} &= -\frac{(n_o^2 - n_e^2)\sin\theta\cos\theta}{\varepsilon_0 n_o^2 n_e^2} \\
\zeta_{xy} = \zeta_{yx} = \zeta_{yz} &= \zeta_{zy} = 0
\end{aligned}
\tag{IV.107}
$$

Combining the dispersive properties of gold nano-particles and anisotropic characters of LCs, the FDTD algorithm for electric field x-component is

$$
\begin{aligned}
E_x|^{n+1}_{i+1/2,j,k} &= C_1 E_x|^{n}_{i+1/2,j,k} \\
&+ C_2\Big(\frac{H_z|^{n+1/2}_{i+1/2,j+1/2,k} - H_z|^{n+1/2}_{i+1/2,j-1/2,k}}{k_y dy} - \frac{H_y|^{n+1/2}_{i+1/2,j,k+1/2} - H_y|^{n+1/2}_{i+1/2,j,k-1/2}}{k_z dz} \\
&+ \psi_{E_{xxy}|^{n}_{i+1/2,j,k}} - \psi_{E_{xxz}|^{n}_{i+1/2,j,k}}\Big) + C_3 \Psi|^{n} \\
&+ dt\zeta_{xy}\Big(\frac{H_x|^{n+1/2}_{i+1/2,j,k+1/2} - H_x|^{n+1/2}_{i+1/2,j,k-1/2}}{k_z dz} - \frac{H_z|^{n+1/2}_{i+1,j,k} - H_z|^{n+1/2}_{i,j,k}}{k_x dx} \\
&+ \psi_{E_{xyz}|^{n}_{i+1/2,j,k}} - \psi_{E_{xyx}|^{n}_{i+1/2,j,k}}\Big) \\
&+ dt\zeta_{xz}\Big(\frac{H_y|^{n+1/2}_{i+1,j,k} - H_y|^{n+1/2}_{i,j,k}}{k_x dx} - \frac{H_x|^{n+1/2}_{i+1/2,j+1/2,k} - H_x|^{n+1/2}_{i+1/2,j-1/2,k}}{k_y dy} \\
&+ \psi_{E_{xzx}|^{n}_{i+1/2,j,k}} - \psi_{E_{xzy}|^{n}_{i+1/2,j,k}}\Big)
\end{aligned}
\tag{IV.108}
$$

where $\psi|^n$ owns to CPML boundary conditions, $\Psi|^n$ is for the dispersive properties of gold. Coefficients C_1, C_2, C_3 depend on the materials we investigated and the model we used.

For the magnetic field x-component, it is as the same as Eq. IV.90, we rewrite it here as follows.

$$
\begin{aligned}
H_x|^{n+1/2}_{i,j+1/2,k+1/2} &= H_x|^{n-1/2}_{i,j+1/2,k+1/2} \\
&- \frac{dt}{\mu_0}\Big(\frac{E_z|^{n}_{i,j+1,k+1/2} - E_z|^{n}_{i,j,k+1/2}}{k_{y|i,j+1/2,k+1/2} dy} - \frac{E_y|^{n}_{i,j+1/2,k+1} - E_y|^{n}_{i,j+1/2,k}}{k_{z|i,j+1/2,k+1/2} dz} \\
&+ \psi_{H_{xy}}|^{n}_{i,j+1/2,k+1/2} - \psi_{H_{xz}}|^{n}_{i,j+1/2,k+1/2}\Big)
\end{aligned}
\tag{IV.109}
$$

Eq. IV.91, Eq. IV.92, Eq. IV.94 and Eq. IV.95 are suitable for this case also.

The numerical description for other electromagnetic elements can be similarly derived by this method.

IV.4 Conclusion

In this chapter, we have reviewed the Yee algorithm, the stability of FDTD method and absorbing boundary conditions CPML, subsequently, the FDTD method are

extended to dispersive materials and anisotropic materials using recursive convolution method and central differential approximation in Cartesian coordinates. Finally, combining the materials we used, nematic LCs and gold for instance, we have given the numerical equations.

Chapitre V

Results

The localized surface plasmon resonance positions and the surface-enhanced raman scattering (SERS) gain (G_{SERS}) of an ordered array of gold nano-cylinders, embedded in a nematic liquid crystal (LC) media, are investigated using finite-difference time domain (FDTD) method. Structures are designed so that the maximum tunability of localized surface plasmon resonance (LSPR) is achieved. Two resonances, and even three may occur when the schematic is specially planned. The influence of the anchoring effects, between nematic LC molecules and glass substrates, on the shift of resonance wavelengths as well as $SERS$ gain are studied, and results are compared with the case of a perfect alignment of the LC molecules and an isotropic material.

V.1 Introduction

In this section, state of art is introduced firstly, including LSPR, liquid crystals (LCs) and anchoring effect of LC molecules. The numerical parameters we used are given subsequently.

V.1.1 LSPR

Localized surface plasmon resonances, due to the specific optical properties of metallic nano-particles, has been the focus of intense research [97; 3; 98]. The electromagnetic enhancement as a result of localized surface plasmon contributes to the surface-enhanced raman scattering [52; 10; 99; 100] effect, and provide valuable observation of chemical species and even single molecules [101; 102; 103; 104; 105]. Meanwhile, the electromagnetic and chemical mechanisms are encompassed to understand the surface-enhanced spectroscopy in theory and experiment [106; 107; 58; 108; 57]. Moreover,

SERS substrates become an popular topic also [109; 110; 111; 108; 112; 105]. Nevertheless, the LSPRs of metallic nano-particles strongly depend on their shape, size and arrangement [113; 18; 114; 45] as well as on the surrounding materials [113; 115; 116].

V.1.2 Liquid crystals

Changing the dielectric properties in the vicinity of the noble nano-particles leads to a change of LSPR positions [115; 116; 117]. As a result, nematic liquid crystals(LCs) have been explored to control the surface plasmon polarization and subsequent optical transmission [118; 119; 120; 25]. Liquid crystals (LCs) are an outstanding material as a surrounding environment for metallic nanoparticles owing to their anisotropy. Indeed, by applying an external electric field, the environment of the particle can be modified, thus LSPR is shifted [121].

So far, many researchers have conjuncted LCs with metallic nanoparticles [25; 26]. For example, gold gratings [122], gold nanorods [123; 124], gold nanodots and nanodisks [125; 126; 120], gold dimer [127], and nanohole arrays [119; 117] have been reported experimentally.

Conjunction of LCs with metallic nanoparticle is mainly applied to electrically controlled and light-driven swiched devices, in our case, we study the tunability of LSPR using liquid crystals.

V.1.3 Anchoring effect

Indeed, some papers have reported numerical investigation of metallic arrays or particles covered by nematic LCs [128; 129; 130; 131; 132]. But all of these works neglect the anchoring phenomenon at the interface of LC molecules and glass substrates, or consider that a weak anchoring condition is met.

On the contrary, we theoretically study strong anchoring effects on the localized surface plasmon resonance (LSPR) peak position of an ordered gold nano-particles array deposited on a glass substrate. A schematic of the setup is depicted on Fig. V.1.

Strong anchoring is considered at the lower and upper interface of LC cell. By

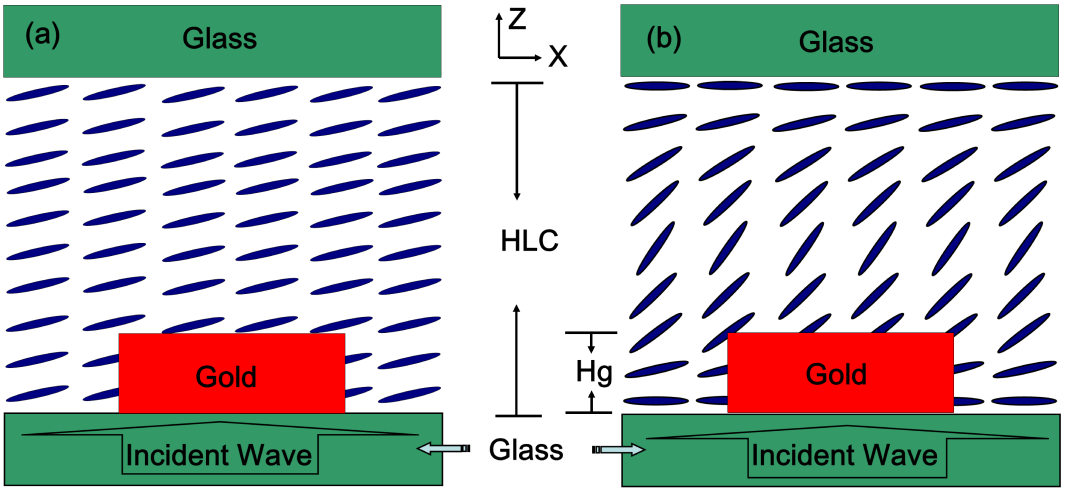

Fig. V.1 – Schematic of the study : gold nanostructures embedded in LC cell are sandwiched between two silica layers. Weak anchoring (left) and strong anchoring (right).

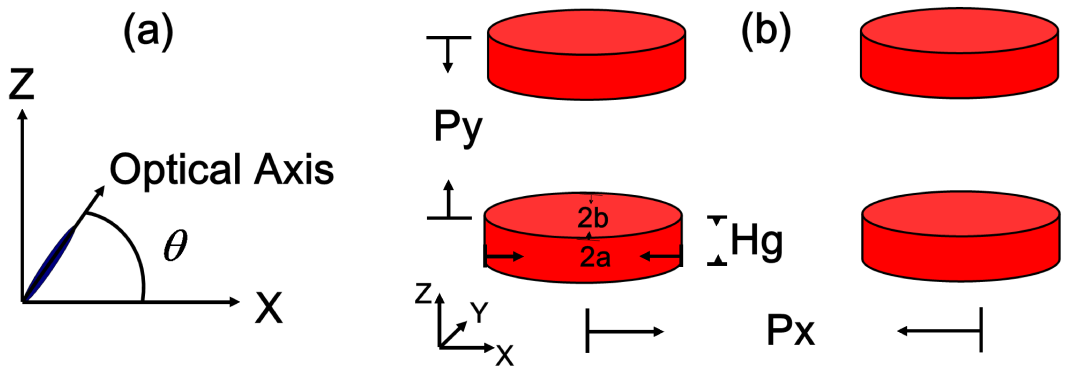

Fig. V.2 – (a) Orientation of optical axis of LC molecule, (b) Array of gold nanoparticles parameters.

comparing the results of perfect alignment and strong anchoring using different structure parameters, the contribution of the LC anchoring effect on LSPR tunability and surface-enhanced raman scattering gain(G_{SERS}) can be checked.

In the simulations, we assume that the optical axis (or director) of LC rotates around the y-axis in $x-z$ plane, and θ is defined as the angle between the optical axis and the x-axis (see Fig. V.2) (a).

The director's change of orientation is obtained by the minimization of the LC molecules' free energy under the influence of an external static electric field, and the alignment of LC molecules on the substrate depends on the anchoring energy.

The LC molecules, at the middle of the cell, respond strongly to the external field

for the reason that they are far away from the glass substrate, so the anchoring torque affects them less. The maximum tilted angle appears in the middle of LCs layer and is defined as θ_{max}. Therefore, in order to describe the variation of the optical axis orientation of LC molecules in z direction, we will use the function [32].

$$\theta(z) = \theta_{max} \sin(\frac{\pi}{H_{LC}} z), \tag{V.1}$$

where H_{LC} is the LC thickness.

The tilted angle θ_{max} can be varied by changing the external electric field. The ordinary and extraordinary refractive index are $n_o = 1.53$ and $n_e = 1.74$, respectively [128].

The incident light propagates along the z-direction from the bottom of the structure in normal incident, with a linear polarization along the x-axis.

V.1.4 Numerical paramaters

The finite-difference time-domain (FDTD) method is used in our simulations [69] for computing extinction spectra. Absorption boundary condition CPML (convolution perfectly matched layer) is used at the lower and upper boundaries of the computational window in order to avoid non-physical reflections [69; 80; 77]. Periodic boundary conditions are used in the x and y directions.

The permittivity of gold is described by Drude-Critical Point model with the recursive convolution method in the FDTD code, this model yields to accurate results in the spectra from 200 nm to 1000 nm [133; 95]. The anisotropic characters of LCs is implemented in the code using a method which has been presented in chapter 4.

Space and time discretization are chosen as $\Delta x = \Delta y = \Delta z = 2\,\text{nm}$, and $\Delta t = \Delta z/(2c)$, respectively. Here, c is the velocity of light in vacuum. Incident light propagates from the bottom of the structure, with a linear polarization along the x-axis.

V.2 Gold cylinder with circular basis

V.2.1 Introduction

Gold cylinders with circular basis are investigated in this part due to their symmetry. LSPR of nano-particles are studied by simulating the optical response of particles surrounded by isotropic material and liquid crystal, respectively. The influence of anchoring effects on LSPR shift are presented as well as the influence of nanoparticle size, interval and periods.

V.2.2 Structure

In this part, first of all, we use gold nano-cylinder with circular basis, the diameter is 100 nm, corresponding to the schematic in Fig. V.2, $2a = 2b = 100$ nm. The periods, both in x-direction and in y-direction, are $P_x = P_y = 200$ nm. The interval among nano-particles is 100 nm. Further more, for gold nano-particles surrounded by LC, the influence of geometrical structure on LSPR is investigated by modifying the nano-particle size, interval and array period.

V.2.3 Gold nano-particles surrounded by isotropic materials

Gold nano-particles are separately surrounded by different isotropic material cell and sandwiched between glass substrates. The index, for instance, is 1.333 (water), 1.53 (ordinary index of nematic LC n_o), 1.74 (extraordinary index of nematic LC n_e) and 2.01 (SiN4), respectively. The height of isotropic material layer maintains 200 nm. The gold nano-particle height H_g varies from 25 nm to 200 nm with the interval of 25 nm.

Extinction spectra are described as a function of wavelength on Fig. V.3(a) for water (index n = 1.333), on Fig. V.3(b) for n_o (index n = 1.53), on Fig. V.3(c) for n_e (index n = 1.74) and on Fig. V.3(d) for SiN4 (index n = 2.01).

The extinction spectra imply that the resonance peak position has a blue shift with the increasing height of gold nano-particle [134]. Meanwhile, the resonance peak is

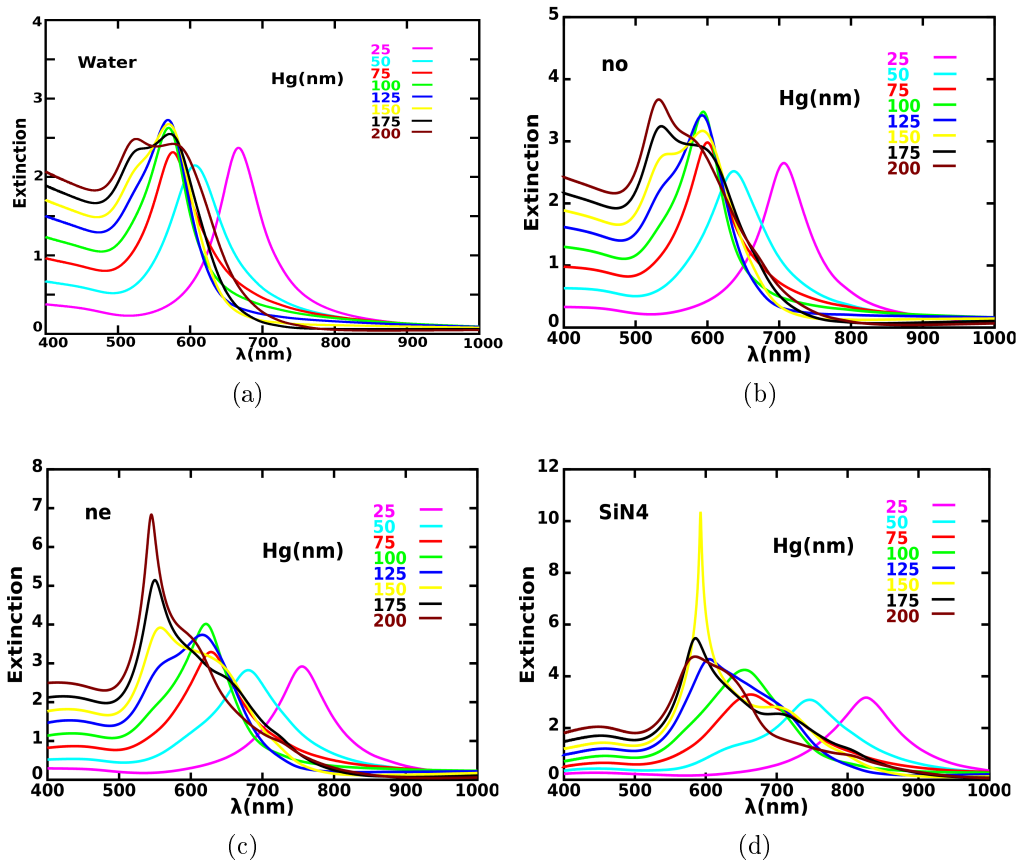

Fig. V.3 – Extinction spectra of different heights of gold nano-particles(H_g varies from 25 nm to 200 nm), surrounded by isotropic materials which are (a) water (n = 1.333), (b) ordinary index of nematic LC n_o (n = 1.53), (c) extraordinary index of nematic LC n_e (n = 1.74) and (d) SiN4 (n = 2.01),respectively.

divided into double resonances, extinction spectrum of $H_g = 150$ nm for instance on Fig. V.3(d). Double resonances will be explained detailedly in later sections.

V.2.4 Gold nano-particles surrounded by LCs

In order to get LSPR shift without varying the gold height or replacing the materials surrounding gold nano-particles, in this section, anisotropic material, nematic LC, is chosen to calculate extinction spectra using FDTD method.

In the first set of computations, the metallic nano-particles are gold cylinders with circular basis (see Fig. V.1), the diameter is $2a = 2b = 100$ nm, and the height varies from $H_g = 25$ nm to $H_g = 100$ nm, the periods of the array are $P_x = P_y = 200$ nm in

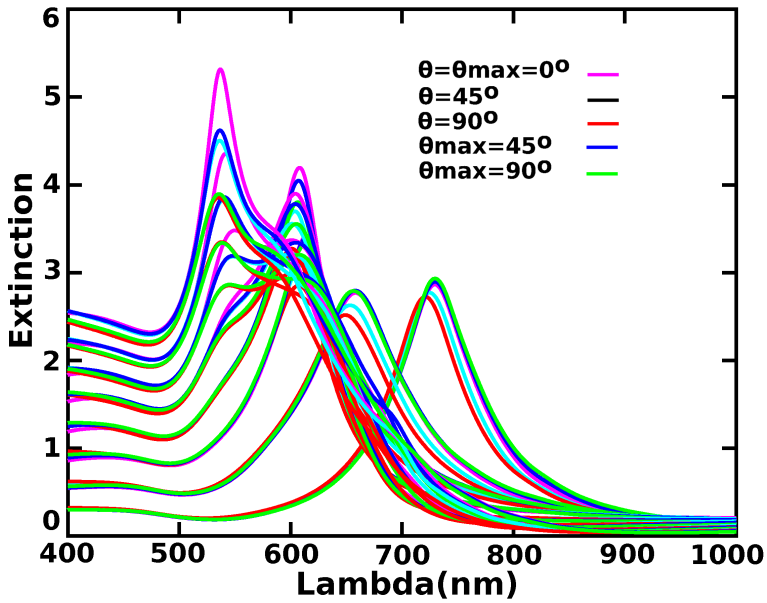

Fig. V.4 – Extinction spectra as a function of orientation of LC molecules. Gold nano-particle height (H_g) varies from 25 nm to 200 nm with interval of 25 nm. Other parameters are fixed as : diameter $2a = 2b = 100$ nm, periods $P_x = P_y = 200$ nm and thickness of LCs cell $H_{LC} = 200$ nm.

both x and y directions, and the thickness of the LC layer is $H_{LC} = 200$ nm. Extinction spectra are described on Fig. V.4

From the extinction spectra shown on Fig. V.4, we can conclude that the spectra, using anisotropic materials LCs as surrounding materials, are very consistent with those of isotropic materials. The main shift is caused by the modification of gold height H_g. Double resonances are achieved also when H_g increases. To easily understand, in this section, we only focus on gold nano-particles with the heights varying from 25 nm to 100 nm. The spectra are described on Fig. V.5.

The influence of anchoring effect of LC molecules on the LSPR can be observed on Fig. V.5, the extinction spectra are as a function of θ (LCs with perfect alignment) and θ_{max} (LCs with anchoring effect) for different heights(25 nm - 100 nm).

The main shift is due to the height modification which induces a blue shift [134], whatever the orientation of the LC molecules, as it is emphasized on Fig. V.6.

The shift of the LSPR for a fixed height is better seen on Fig. V.7, with $H_g = 50$ nm

The blue curve describes the LSPR for a constant θ and has the behavior previously

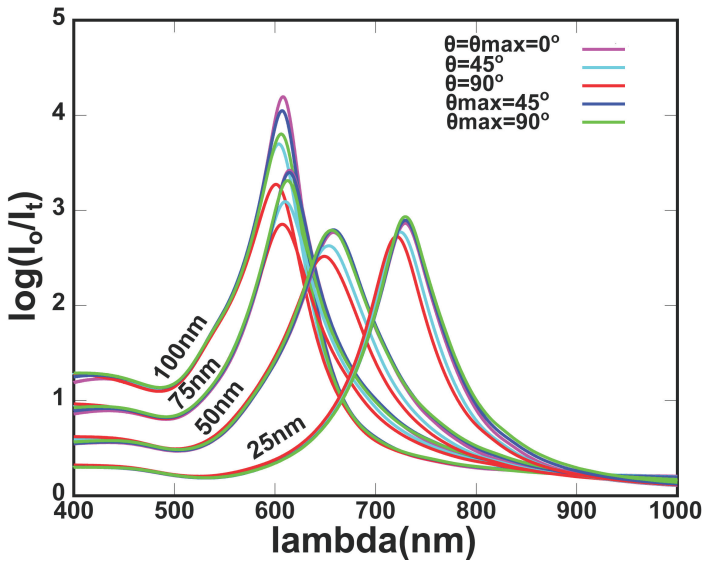

Fig. V.5 – Extinction spectra as a function of θ and θ_{max} for different gold structures heights.

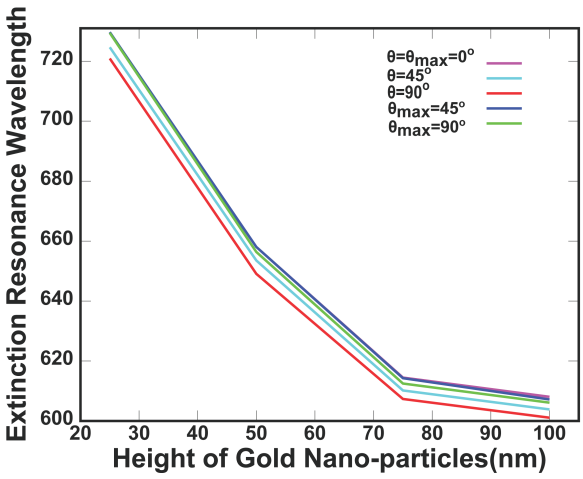

Fig. V.6 – LSPR shift as a function of the height of the gold structures for different LC orientations.

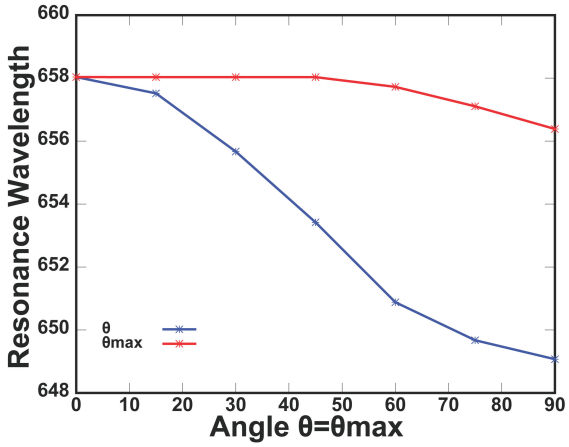

Fig. V.7 – LSPR shift as a function of θ (blue curve) or θ_{max} (red line) for $H_g = 50\,\text{nm}$.

described [128]. The red curve shows the LSPR shift as a function of θ_{max}, that is with anchoring effects taken into account. It is clear here that the tunability of the resonance is strongly affected, as it is lower than 2 nm, whereas it was around 9 nm without the anchoring.

Thereby, we can conclude that the sensitivity $S = \dfrac{d\lambda}{dn}$ [130] will also be strongly lowered.

We can check how the sensitivity depends on the height of gold cylinders for $H_g =$ 25 nm, 50 nm, 75 nm and 100 nm. All other parameters are the same as in the first set of computations.

The calculated shifts $\Delta\lambda_\theta$ and $\Delta\lambda_{\theta_{max}}$ are given in Tab. V.1. λ_0 is defined as the resonance wavelength position, $\Delta\lambda_\theta$ is the tunability of LSPR in the case perfect alignment of all LC molecules, $\Delta\lambda_{\theta_{max}}$ stands for the tunability with LCs anchoring effect taken into account.

Without the anchoring effect, the highest value of $\Delta\lambda_\theta$ is achieved for 50 nm. On the other hand, $\Delta\lambda_{\theta_{max}}$ highest value is achieved for 75 nm, but the dependence on the height of the structure is very weak. For the smallest height $H_g = 25\,\text{nm}$, no change on the resonant position could be observed. This can be explained by the fact that the top of the structure is located at a position where the rotation of the LC molecules is really small, whereas it is slightly bigger for other heights. Nevertheless, the calculated shifts are all very small. The fact that the biggest shift $\Delta\lambda_{\theta_{max}}$ appears at $H_g = 75\,\text{nm}$ due

Tab. V.1 – Gold nano-cylinders with circular basis. Periods are $P_x = P_y = 200\,\text{nm}$, gold height H_g varies from 25 nm to 100 nm, diameter is $2a = 2b = 100\,\text{nm}$, height of LC cell is 200 nm. λ_0 is defined as the resonance wavelength position. $\Delta\lambda_\theta$ is the tunability of LSPR in the case perfect alignment of all LC molecules. $\Delta\lambda_{\theta_{max}}$ stands for the tunability with LCs anchoring effect taken into account.

H_g (nm)	25	50	75	100
λ_0(nm)	729.7	657.8	614.6	607.9
$\Delta\lambda_\theta$(nm)	8.53	8.96	7.11	6.97
$\Delta\lambda_{\theta_{max}}$(nm)	0	1.65	1.97	1.93

Tab. V.2 – Gold nano-cylinders with circular basis. Periods are fixed as $P_x = 150\,\text{nm}$ and $P_y = 200\,\text{nm}$, gold height H_g varies from 25 nm to 100 nm, diameter is $2a = 2b = 100\,\text{nm}$, height of LC cell is $H_{LC} = 200\,\text{nm}$. $\Delta\lambda_\theta$ is the tunability of LSPR in the case perfect alignment of all LC molecules. $\Delta\lambda_{\theta_{max}}$ stands for the tunability with LCs anchoring effect taken into account.

H_g (nm)	25	50	75	100
λ_0(nm)	767.91	687.82	632.82	623.22
$\Delta\lambda_\theta$(nm)	19.73	12.41	13.46	11.81
$\Delta\lambda_{\theta_{max}}$(nm)	0.84	5.15	5.68	5.14

to both contributions of the size of gold nano-particles and the rotation of LC optical axis.

V.2.5 Influence of gold array period P_x on the LSPR

To improve the tunability of LSPR, modification of the period in x-direction P_x are completed from 150 nm to 300 nm. G_{SERS} is computed using excitation wavelength fixed at 590 nm and 632.8 nm with the interval 50 nm. Other parameters are the same with those above. The shift of LSPR are separately described in the Tab. V.2, Tab. V.3 and Tab. V.4. In detail, Tab. V.2 for $P_x = 150\,\text{nm}$, Tab. V.3 for $P_x = 250\,\text{nm}$ and Tab. V.4 for $P_x = 300\,\text{nm}$.

Comparing the results with P_x modified, the main blue shift is achieved with the increasing H_g. The shift of LSPR is improved to around $\Delta\lambda_{\theta_{max}} = 6\,\text{nm}$(see in Tab. V.2) when $H_g = 50\,\text{nm}$, which seems like weak although three times higher than the result in Tab. V.1.

Tab. V.3 – Gold nano-cylinders with circular basis. Periods are fixed as $P_x = 250\,\text{nm}$ and $P_y = 200\,\text{nm}$, gold height H_g varies from 25 nm to 100 nm, diameter is $2a = 2b = 100\,\text{nm}$, height of LC cell is $H_{LC} = 200\,\text{nm}$. $\Delta\lambda_\theta$ is the tunability of LSPR in the case perfect alignment of all LC molecules. $\Delta\lambda_{\theta_{max}}$ stands for the tunability with LCs anchoring effect taken into account.

H_g (nm)	25	50	75	100
λ_0(nm)	722.68	653.52	613.38	606.46
$\Delta\lambda_\theta$(nm)	6.17	5.65	6.04	5.73
$\Delta\lambda_{\theta_{max}}$(nm)	1.75	0.41	0.90	0.53

Tab. V.4 – Gold nano-cylinders with circular basis. Periods are fixed as $P_x = 300\,\text{nm}$ and $P_y = 200\,\text{nm}$, gold height H_g varies from 25 nm to 100 nm, diameter is $2a = 2b = 100\,\text{nm}$, height of LC cell is $H_{LC} = 200\,\text{nm}$. $\Delta\lambda_\theta$ is the tunability of LSPR in the case perfect alignment of all LC molecules. $\Delta\lambda_{\theta_{max}}$ stands for the tunability with LCs anchoring effect taken into account.

H_g (nm)	25	50	75	100
λ_0(nm)	722.41	657.00	619.18	610.88
$\Delta\lambda_\theta$(nm)	3.22	2.87	2.00	4.24
$\Delta\lambda_{\theta_{max}}$(nm)	0.01	1.65	0.55	0.36

V.2.6 Influence of gold array with proportionate variation on the LSPR

Subsequently, simulations are completed with the variation not only of the periods but also the size of the metallic particles. Firstly, the results are exhibited in Tab. V.5 using the parameters $P_x = P_y = 100\,\text{nm}$, 2a = 2b = 50 nm, $H_{LC} = 200\,\text{nm}$, gold height H_g varies from 25 nm to 100 nm. Then, for the parameters $P_x = P_y = 300\,\text{nm}$, $2a = 2b = 150\,\text{nm}$, $H_{LC} = 200\,\text{nm}$, gold height H_g varies from 25 nm to 100 nm also, the results are exhibited in Tab. V.6.

From Tab. V.5 and Tab. V.6, we can conclude that the tunability does not increase with the proportionate variation of gold nano-particles as well as array period.

V.2.7 Conclusion

In this section, LSPR of gold cylinders with circular basis are studied by simulating the extinction spectra. Herein, influence of materials surrounding gold nanoparticles on

Tab. V.5 – Gold nano-cylinders with circular basis. Periods are fixed as $P_x = P_y =$ 100 nm, diameter is $2a = 2b = 50$ nm, gold height H_g varies from 25 nm to 100 nm, height of LC cell is $H_{LC} = 200$ nm. $\Delta\lambda_\theta$ is the tunability of LSPR in the case perfect alignment of all LC molecules. $\Delta\lambda_{\theta_{max}}$ stands for the tunability with LCs anchoring effect taken into account.

H_g (nm)	25	50	75	100
λ_0(nm)	642.90	589.92	572.99	542.18
$\Delta\lambda_\theta$(nm)	12.18	3.46	17.60	2.65
$\Delta\lambda_{\theta_{max}}$(nm)	0.98	3.34	2.99	0.14

Tab. V.6 – Gold nano-cylinders with circular basis. Periods are fixed as $P_x = P_y =$ 300 nm, diameter is $2a = 2b = 150$ nm, gold height H_g varies from 25 nm to 100 nm, height of LC cell is $H_{LC} = 200$ nm. $\Delta\lambda_\theta$ is the tunability of LSPR in the case perfect alignment of all LC molecules. $\Delta\lambda_{\theta_{max}}$ stands for the tunability with LCs anchoring effect taken into account.

H_g (nm)	25	50	75	100
λ_0(nm)	642.90	589.92	572.99	542.18
$\Delta\lambda_\theta$(nm)	0	11	13	12
$\Delta\lambda_{\theta_{max}}$(nm)	0	0.8	6.5	6.1

LSPR are calculated using isotropic materials(The index, for instance, is 1.333 (water), 1.53 (ordinary index of nematic LC n_o), 1.74 (extraordinary index of nematic LC n_e) and 2.01 (SiN4).) and anisotropic materials(LCs), respectively.

We got that the spectra, using LCs, are very consistent with those of isotropic materials. LSPR has a blue-shift with increasing gold height. The anchoring effect of LC molecules strongly decrease the tunability of resonance. By modifying gold nanoparticle size, interval and array periods, the maximum shift of LSPR is as small as $\Delta\lambda_{\theta_{max}}$ = 5.68 nm(see Tab. V.2) with anchoring effect considered, $\Delta\lambda_\theta$ is around 18 nm(see Tab. V.5) for perfect alignment of LCs.

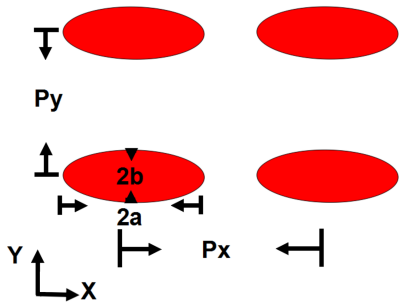

Fig. V.8 – Major axis orientation of gold cylinder with elliptic basis along x-coordinate.

V.3 Gold cylinder of elliptical basis with major axis orientation along x coordinate

V.3.1 Introduction

According to the analysis in the section above, in order to increase the tunability $\Delta\lambda_{\theta_{max}}$, in this part, we will check the influence of gold nano-structure shape on the LSPR shift, as it was proposed in previous works [130]. Therefore, gold-cylinders of elliptical basis are studied.

V.3.2 Structure

For different gold heights from 25 nm to 100 nm with interval of 25 nm, gold cylinders of elliptical basis with the orientation of major axis along x-coordinate are investigated. The schematic is described in Fig. V.8.

A few sets of simulations have been made for gold cylinders with different parameters including inter-particles distance, major axis and minor axis. Resonance wavelength and tunability will be given in the sections as follows.

V.3.3 Gold cylinder of elliptical basis with variation of period P_x

In the first set of simulation, the period in x direction (P_x) increases from 125 nm to 200 nm, gold height H_g varies from 25 nm to 100 nm, both of them are with interval of 25 nm. Other parameters remain constant : LC height H_{LC} (200 nm), major axis of

Tab. V.7 – Gold nano-cylinders with elliptical basis. P_x and H_g increase from 125 nm to 200 nm and 25 nm to 100 nm with interval 25 nm, respectively. Other parameters are fixed as : major axis $2a = 100$ nm, minor axis $2b = 50$ nm, the period $P_y = 200$ nm and $H_{LC} = 200$ nm. λ_0 is defined as the resonance wavelength position. $\Delta\lambda_\theta$ is the tunability of LSPR in the case perfect alignment of all LC molecules. $\Delta\lambda_{\theta_{max}}$ stands for the tunability with LCs anchoring effect taken into account.

P_x(nm)	H_g(nm)	25	50	75	100
	λ_0(nm)	925.9	858.8	790.2	758.5
$125nm$	$\Delta\lambda_\theta$(nm)	30.8	33.5	39.3	30.3
	$\Delta\lambda_{\theta_{max}}$(nm)	3.3	13.8	20.0	12.9
	λ_0(nm)	851.8	775.0	726.2	699.1
$150nm$	$\Delta\lambda_\theta$(nm)	17.6	23.3	22.4	14.6
	$\Delta\lambda_{\theta_{max}}$(nm)	1.4	6.3	14.7	8.3
	λ_0(nm)	821.8	749.0	707.1	681.3
$175nm$	$\Delta\lambda_\theta$(nm)	5.1	14.7	14.9	8.7
	$\Delta\lambda_{\theta_{max}}$(nm)	3.9	4.8	9.9	4.4
	λ_0(nm)	810.3	739.0	695.8	673.9
$200nm$	$\Delta\lambda_\theta$(nm)	11.7	12.3	7.3	8.1
	$\Delta\lambda_{\theta_{max}}$(nm)	3.1	8.2	5.0	3.0

gold cylinder with elliptic basis $2a$ (100 nm), minor axis $2b$ (50 nm), period of array in y direction P_y (200 nm).

The resonant wavelength and tunability are presented in Tab. V.7.

The maximum shift $\Delta\lambda_{\theta_{max}}$ is equal to 20 nm for $P_x = 125$ nm and $H_g = 75$ nm. With the perfect alignment of LCs, the maximum tunability $\Delta\lambda_\theta$ is around 40 nm. This corresponds to a distance between nano-particles in x-direction of 25 nm.

V.3.4 Gold cylinder of elliptical basis with variation of major axis $2a$

Subsequently, the major axis and height of gold cylinder are increased from 100 nm to 175 nm and from 25 nm to 100 nm, respectively. Values of LC height H_{LC}(200 nm), minor axis $2b$(50 nm) and the periods in x and y direction(200 nm) are fixed. The resonant wavelength and tunability are given in Tab. V.8.

The maximum shift $\Delta\lambda_{\theta_{max}}$ is up to 24.7 nm when $P_x = 175$ nm and $H_g = 75$ nm. Correspondingly, with perfect alignment of LCs, the maximum tunability $\Delta\lambda_\theta$ is around

Tab. V.8 – Gold nano-cylinders with elliptical basis. Major axis $2a$ and gold height H_g increase from 100 nm to 175 nm and from 25 nm to 100 nm with interval 25 nm, respectively. Other parameters are fixed as : minor axis $2b = 50$ nm, the periods $P_x = P_y = 200$ nm and $H_{LC} = 200$ nm. λ_0 is defined as the resonance wavelength position. $\Delta\lambda_\theta$ is the tunability of LSPR in the case perfect alignment of all LC molecules. $\Delta\lambda_{\theta_{max}}$ stands for the tunability with LCs anchoring effect taken into account.

$2a$(nm)	H_g(nm)	25	50	75	100
100	λ_0(nm)	811.0	738.4	695.3	673.9
	$\Delta\lambda_\theta$(nm)	8.7	11.3	6.8	8.1
	$\Delta\lambda_{\theta_{max}}$(nm)	0.6	3.2	2.8	3.0
125	λ_0(nm)	921.4	825.0	769.9	724.2
	$\Delta\lambda_\theta$(nm)	12.7	17.2	17.2	14.2
	$\Delta\lambda_{\theta_{max}}$(nm)	0.8	3.8	8.9	6.4
150	λ_0(nm)	1050.7	932.9	861.6	787.8
	$\Delta\lambda_\theta$(nm)	17.6	25.8	27.4	21.3
	$\Delta\lambda_{\theta_{max}}$(nm)	1.2	6.6	14.6	7.6
175	λ_0(nm)	1251.3	1119.1	1030.1	893.5
	$\Delta\lambda_\theta$(nm)	32.7	45.8	47.3	33.4
	$\Delta\lambda_{\theta_{max}}$(nm)	1.5	13.6	24.7	13.5

47 nm. The interval of nano-particles in x-direction is 25 nm as well.

V.3.5 Gold cylinder of elliptical basis with variation of minor axis $2b$

Finally, the minor axis $2b$ and gold height are varied from 50 nm to 125 nm and from 25 nm to 100 nm with interval of 25 nm,respectively. The other parameters are constant ($2a = 100$ nm, $P_x = P_y = 200$ nm, $H_{LC} = 200$ nm). The resonant wavelength and tunability are given in Tab. V.9.

From Tab. V.9, we can observe that the maximum shift $\Delta\lambda_{\theta_{max}}$ remains around 24 nm when $H_g = 75$ nm no matter whatever the minor axis is. Therefore, we can conclude that the variation of minor axis affects weakly the tunability owing to the incident wave with x-polarization.

In short, for all modifications of the period in x-direction, or modifications of the major axis or minor axis of gold ellipsoid, the anchoring effect strongly reduces the LSPR shift. The resonance wavelength exhibits a blue shift when the gold height in-

Tab. V.9 – Gold nano-cylinders with elliptical basis. Minor axis $2b$ and gold height H_g increase from 50 nm to 125 nm and from 25 nm to 100 nm with interval 25 nm, respectively. Other parameters are fixed as : major axis $2a = 100$ nm, the periods $P_x = P_y = 200$ nm and $H_{LC} = 200$ nm. λ_0 is defined as the resonance wavelength position. $\Delta\lambda_\theta$ is the tunability of LSPR in the case perfect alignment of all LC molecules. $\Delta\lambda_{\theta_{max}}$ stands for the tunability with LCs anchoring effect taken into account.

$2b$(nm)	H_g(nm)	25	50	75	100
	λ_0(nm)	1251.3	1119.1	1030.1	893.5
50	$\Delta\lambda_\theta$(nm)	32.7	45.8	47.3	33.4
	$\Delta\lambda_{\theta_{max}}$(nm)	1.5	13.6	24.7	13.5
	λ_0(nm)	1147.2	1017.1	915.8	885.6
75	$\Delta\lambda_\theta$(nm)	32.9	44.3	43.4	40.7
	$\Delta\lambda_{\theta_{max}}$(nm)	1.3	13.6	24.1	13.9
	λ_0(nm)	1087.7	950.2	817.9	707.8
100	$\Delta\lambda_\theta$(nm)	36.5	42.7	38.9	13.5
	$\Delta\lambda_{\theta_{max}}$(nm)	3.4	14.4	24.1	5.0
	λ_0(nm)	1034.1	887.9	747.9	702.3
125	$\Delta\lambda_\theta$(nm)	37.4	40.2	31.7	34.8
	$\Delta\lambda_{\theta_{max}}$(nm)	5.1	14.1	11.6	28.0

creases. The maximum shift is achieved at $H_g = 75$ nm when the interval between gold nano-particles is 25 nm in x-direction. For instance, $\Delta\lambda_{\theta_{max}} = 20$ nm when $P_x = 125$ nm in Tab.V.7 and $\Delta\lambda_{\theta_{max}} = 24.7$ nm when $2a = 175$ nm in Tab.V.8. Tab.V.9 implies that the modification of minor axis has negligible influence on the tunability when the anchoring effect is considered.

If the gold particle size remains the same, resonance peak position is blue-shifted as the period increases in x-direction (see Tab. V.7). Correspondingly, if the period and other parameters are fixed, resonance peaks are red-shifted as the major axis increases (see in Tab. V.8). In contrast, blue shift is observed if minor axis $2b$ increases(see in Tab V.9). The LSPR wavelength λ_0 has a large tunability (for instance, from around 670 nm to 1250 nm in Tab. V.8) when one modify the nano-particle size and the inter-particles distance in x direction. This is in agreement with results of previous works [42; 43; 135; 136; 137; 138].

Tab. V.10 – Gold nano-cylinders with elliptical basis. $2a = 100\,\text{nm}, 2b = 50\,\text{nm}, P_x = P_y = 200\,\text{nm}$.

H_g(nm)		25	50	75	100
	λ_0(nm)	810.96	738.43	695.34	673.89
H_{LC}=200 nm	$\Delta\lambda_\theta$(nm)	8.68	11.27	6.85	8.13
	$\Delta\lambda_{\theta_{max}}$(nm)	0	3.11	2.76	3.02
	λ_0(nm)	810.34	738.95	695.81	673.89
$H_{LC} = 2H_g$	$\Delta\lambda_\theta$(nm)	11.73	12.29	7.31	8.13
	$\Delta\lambda_{\theta_{max}}$(nm)	3.12	8.24	5.04	3.02

V.3.6 Influence of H_{LC} on the shift of LSPR

As it was already suggested previously, the position of the top part of the gold structures has an influence on the LSPR shift possibilities. Therefore in the following, we still use gold cylinders with ellipsoid basis with the same parameters as above except LC height $H_{LC} = 2H_g$, which implies that the upper part of the nanostructure will always be at the position of the maximum rotation of the LC axis. The results will be compared with $H_{LC} = 200\,\text{nm}$.

Here, we let major axis $2a = 100\,\text{nm}$, minor axis $2b = 50\,\text{nm}$, the periods of gold nano-particle array $P_x = P_y = 200\,\text{nm}$, H_g varies from 25 nm to 100 nm. The extinction spectra are presented in Tab.V.10.

$\Delta\lambda_\theta$ and $\Delta\lambda_{\theta_{max}}$ exhibit in this case a small increase, but the anchoring effect still strongly reduces the LSPR shift. We see that for this configuration, it is possible to increase the LSPR peak shift $\Delta\lambda_{\theta_{max}}$ up to 8.24 nm, which is a little bigger than the results 3.11 nm obtained using $H_{LC} = 200\,\text{nm}$.

Therefore a systematic study using different parameters should even lead to higher values for $\Delta\lambda_{\theta_{max}}$.

Based on the results in the section above, we have made a series of numerical experiments using cylinders with elliptic basis, changing the periodicity and the shape of gold nanoparticles arrays.

Firstly, the calculations are performed for the same size of gold nano-particles as previously defined ($2a = 100\,\text{nm}$, $2b = 50\,\text{nm}$), but we decrease the period in x-direction

Tab. V.11 – Gold nano-cylinders with elliptical basis. $2a$= 100 nm, $2b$ = 50 nm, P_x = 125 nm, P_y = 200 nm.

H_g(nm)		25	50	75	100
H_{LC}=200 nm	λ_0 (nm)	925.90	858.78	790.19	758.46
	$\Delta\lambda_\theta$(nm)	30.83	33.46	39.33	30.29
	$\Delta\lambda_{\theta_{max}}$(nm)	3.26	13.84	20.02	12.94
$H_{LC} = 2H_g$	λ_0(nm)	925.90	859.49	790.48	758.46
	$\Delta\lambda_\theta$(nm)	32.35	34.49	39.36	30.29
	$\Delta\lambda_{\theta_{max}}$(nm)	20.39	24.30	24.54	12.94

Tab. V.12 – Gold nano-cylinders with elliptical basis. $2a$ = 175 nm, 2b = 50 nm, $P_x = P_y$ = 200 nm.

H_g (nm)		25	50	75	100
H_{LC}=200nm	λ_0(nm)	1251.28	1119.08	1030.04	893.55
	$\Delta\lambda_\theta$(nm)	32.72	45.82	47.31	33.35
	$\Delta\lambda_{\theta_{max}}$(nm)	1.49	13.57	24.69	13.50
$H_{LC} = 2H_g$	λ_0(nm)	1248.31	1118.48	1030.54	893.55
	$\Delta\lambda_\theta$(nm)	36.08	45.77	48.27	33.35
	$\Delta\lambda_{\theta_{max}}$(nm)	21.18	27.92	30.95	13.50

by simply using P_x = 125 nm [130] and maintaining P_y = 200 nm, the thickness of LC are respectively 200 nm and $2H_g$.

Results are described in Tab. V.11.

We observe that the best spectral tunability $\Delta\lambda_{\theta_{max}}$ increases up to 24.54 nm for H_g = 75 nm with $H_{LC} = 2H_g$. With H_{LC} = 200 nm, $\Delta\lambda_{\theta_{max}}$ increase is less pronounced. Comparing with the results in Tab. V.10, we also observe that the resonance wavelength is red-shifted for a given height of the particles, e.g. λ_0 increases from around 695 nm to 790 nm for H_g = 75 nm, due to the variation of the distance between nano-particles.

A step further, keeping the distance of nanoparticles in x-direction equal to 25 nm, but increasing major axis from 100 nm to 175 nm and still using $2b$ = 50 nm, $P_x = P_y$ = 200 nm, the same calculations are done and results are presented in Tab. V.12.

By comparison with the results in Tab. V.11, for a fixed H_g, a new red-shift of the resonance wavelength λ_0 is observed, due to the modification of the aspect ratio. Moreover, $\Delta\lambda_{\theta_{max}}$ has been improved up to 30.95 nm for H_g = 75 nm, which is around

Tab. V.13 – Gold nano-cylinders with elliptical basis. $2a = 175\,\text{nm}$, $2b = 100\,\text{nm}$, $P_x = P_y = 200\,\text{nm}$.

H_g(nm)		25	50	75	100
H_{LC}=200nm	λ_0(nm)	1087.61	950.23	817.93	707.78
	$\Delta\lambda_\theta$(nm)	36.53	42.76	38.89	13.36
	$\Delta\lambda_{\theta_{max}}$(nm)	3.37	14.42	24.15	4.98
$H_{LC} = 2H_g$	λ_0(nm)	1083.80	949.80	817.61	707.78
	$\Delta\lambda_\theta$(nm)	38.88	43.90	39.44	13.36
	$\Delta\lambda_{\theta_{max}}$(nm)	23.56	27.97	30.09	4.98

16 times higher than the value achieved in Tab. V.1.

From the three previous series of computations in Tab. V.10, V.11 and V.12 , it is seen that $\Delta\lambda_{\theta_{max}}$ and $\Delta\lambda_\theta$ are always greater in the case $H_{LC} = 2H_g$ than in the case $H_{LC} = 200\,\text{nm}$, which confirms the assumption that the position of the upper part of nanoparticles relatively to the maximal rotation of the LC molecules has influence on the LSPR shift. Meanwhile, the resonance peak position λ_0 only weakly depends on H_{LC}, whereas $\Delta\lambda_{\theta_{max}}$ is more strongly modified. Up to now, all our attempts to increase $\Delta\lambda_{\theta_{max}}$ have led to a red shift of the resonance position also.

We now show that it is also possible to keep a high value for $\Delta\lambda_{\theta_{max}}$ while the resonance is blue-shifted. A new set of calculation is performed using the parameters $2a = 175\,\text{nm}$, $2b = 100\,\text{nm}$, $P_x = P_y = 200\,\text{nm}$. Results are presented in Tab. V.13.

The LSPR shifts slightly by comparison with results from Tab. V.12, but no perceptible modification of $\Delta\lambda_{\theta_{max}}$ is observed.

V.3.7 Conclusion

In this section, we have investigated LSPR shift of gold nanostructures embedded in a LC cell as a function the optical axis orientation of the LC molecules by taking anchoring effects into account. We have shown that these effects strongly reduce the LSPR tunability also, but that modifications to the nanostructures shape or LC height could efficiently compensate it. Maximum tunability of LSPR is observed as $\Delta\lambda_{\theta_{max}} = 30.95\,\text{nm}$ for $H_g = 75\,\text{nm}$ (see Tab. V.12) with anchoring effect considered.

Nevertheless, most of the interesting shifts were achieved for $H_g = 75\,\text{nm}$. Further

work is still required to fully optimize the configuration in order to get a greater tunability.

V.4 Gold cylinder with elliptical basis with orthogonal major axis orientation.

V.4.1 Introduction

Up to now, the influence of shape, size of nano-particles and their interval on the shift of LSPR was checked. To improve the tunability of LSPR comparing the previous section, in this part, the major axis orientation of gold nano-cylinder with elliptic basis will be investigated.

The influence of the anchoring effect of LC molecules on LSPR are investigated comparing with those of the perfect alignment of LCs also. Herein, double resonance peaks even three occur by modifying the major axis orientation of gold nano-particle. Meanwhile, the tunability of LSPR is improved obviously.

V.4.2 Structure

In our simulations, gold nano-cylinders with elliptic basis array are embedded in a LC cell and then sandwiched between two glass substrates (see Fig. V.9). Orientation of LC molecule is assumed in the xz-plane and they may rotate around y-axis, θ is defined as the angle between orientation of LC molecules and x-axis.

The alignment of LC molecules at the surface of glass substrate depends on the anchoring energy. The maximum tilted angle θ_{max} is achieved at the middle of the LC cell owing to the weak influence of anchoring torque. Hence, the function given by (Eq.V.1) will be used to describe the optical axis orientation of LC molecules as a function of z [32], which has been given in previous part.

According to the different major axis orientation of gold nano-cylinder with elliptic basis, the metallic particle arrays we study are classified into three cases : major axis orientation of gold particle is along x-axis (see Fig. V.9c), orthogonal with each other

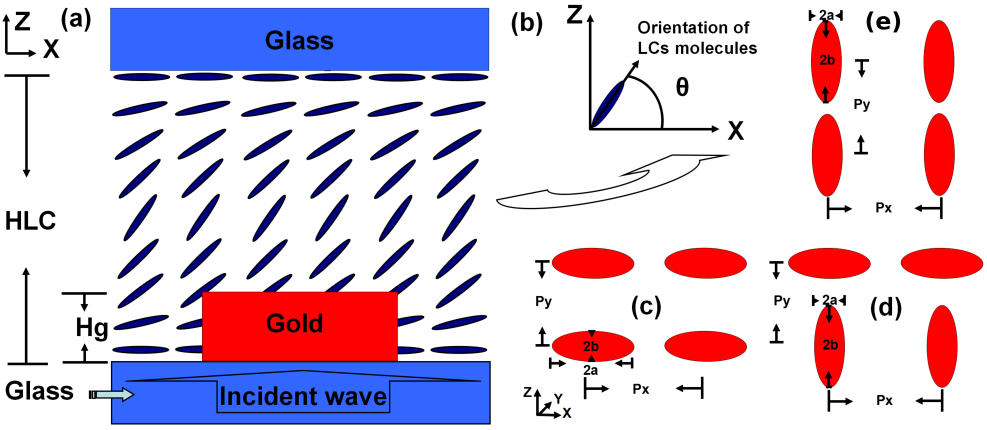

Fig. V.9 – (a) Schematic of the study : gold particle array embedded in a LC cell is sandwiched between two silica substrate. (b) Optical axis orientation of LC molecules. Major axis orientation of gold particle is (c) along x axis, (d) orthogonal with each other, and (e) along y axis.

(see Fig. V.9d) and along y-axis(see Fig. V.9e).

Gold cylinders of elliptical basis with major axis orientation along x-axis are used to get LSPR tunability in section V.3. To improve the tunability, gold cylinders of elliptical basis with orthogonal axis orientation are chosen in section V.4.3, and in this case, double resonant peaks are observed. As a comparative experiment, gold particles with major axis along y-axis are simulated to explain the double resonances in section V.4.4.

V.4.3 Influence of orthogonal major axis orientation of metallic particles on the shift of LSPR

Based on the results mentioned in previous part, in this section, the parameters of nano-structures are chosen as $H_{LC} = 200\,\text{nm}, H_g = 75\,\text{nm}, 2a = 175\,\text{nm}, 2b = 100\,\text{nm}, P_x = 200\,\text{nm}, P_y = 400\,\text{nm}$.

The simulations are made using gold nano cylinder with elliptic basis with orthogonal major axis. The schematic is presented on Fig. V.9 (d). The extinction spectra are plotted on Fig. V.10(a) as a function of the orientation of LC molecules.

The extinction spectra clearly present double resonances on Fig. V.10(a). Resonance wavelength (λ_1) is around 600 nm, the second (λ_2) is around 1200 nm. It is easy to

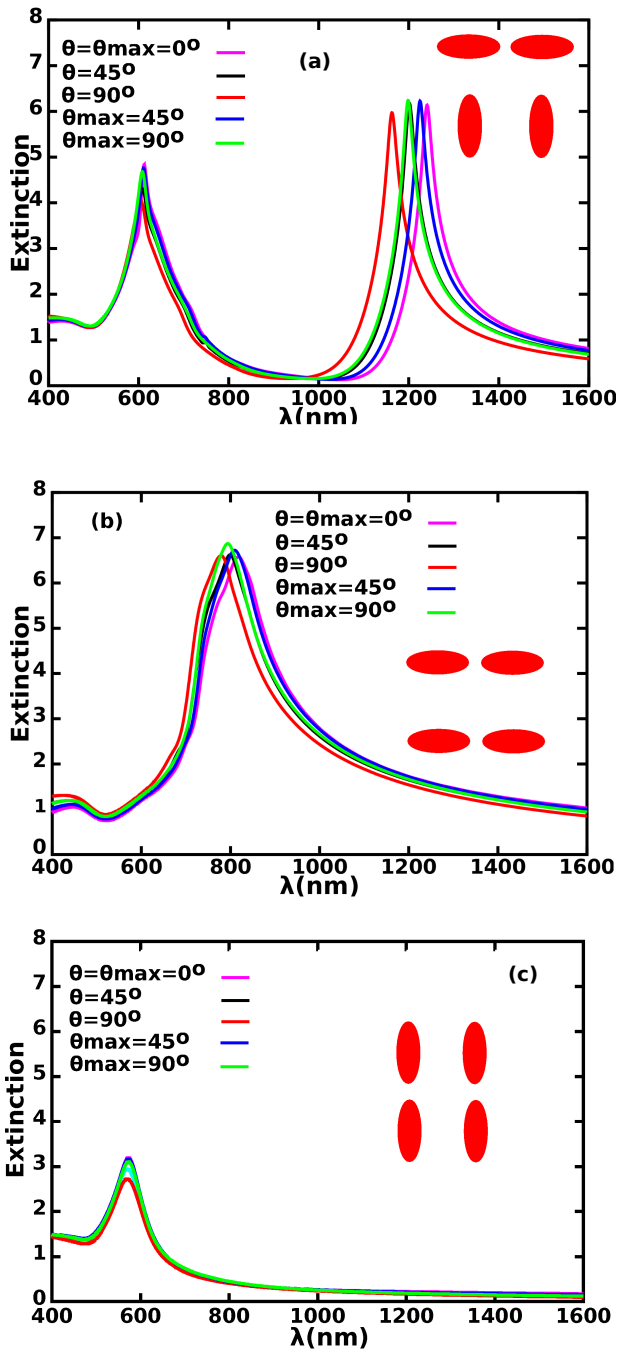

Fig. V.10 – Extinction spectra for different major axis orientation of gold cylinders with elliptic basis (a) orthogonal with each other (b) along x-coordinate and (c) along y-coordinate. The size of gold cylinders with elliptic basis, major axis : $2a = 175\,\mathrm{nm}$, minor axis : $2b = 100\,\mathrm{nm}$, height of gold particles : $H_g = 75\,\mathrm{nm}$.

observe that λ_1 is almost independent of the orientation of LCs. In contrast, λ_2 is shifted up to $\Delta\lambda_\theta = 64.86\,\text{nm}$ for LCs with perfect alignment, while it is decreased to $\Delta\lambda_{\theta_{max}} = 42.55\,\text{nm}$ with anchoring effects considered. These results are better than $\Delta\lambda_{\theta_{max}} = 30.95\,\text{nm}$ in Tab. V.12.

V.4.4 Double LSPR resonance peaks

To analyse the positions of double resonance peaks, as a comparison, gold nanoparticles are chosen with the same size and shape as those we have used except that the major axis orientation of all gold particles are either along x-coordinate(see Fig. V.9 (c)) or along y-coordinate (see Fig. V.9 (e)). The corresponding extinction spectra are given on Fig. V.10(b) and on Fig. V.10(c).

The electric intensity maps (see Fig. V.11) are plotted using the particle array with orthogonal major axis orientation and $\theta_{max} = 90^o$. Electric field intensity distribution are computed for double resonance wavelengths positions $\lambda_1 = 608\,\text{nm}$ and $\lambda_2 = 1198\,\text{nm}$, respectively. We can observe that the field intensity of metallic particle with major axis along y-coordinate is stronger at the resonance wavelength 608 nm. In contrast, at the resonance wavelength 1198 nm, the field intensity is stronger around the metallic particle with major axis along x-coordinate.

By comparing the resonance wavelength positions plotted on Fig. V.10 as well as the electric intensity maps given on Fig. V.11, we can conclude that the left resonance peak(λ_1) results from the coupling effect among the gold particles with major axis along y-coordinate. Correspondingly, the resonance peak(λ_2), appeared on right side due to the coupling effect among the particles with major axis along x-coordinate, is more sensitive to the change of refractive index of the environment. It is as described in previously sections.

V.4.5 Influence of H_g and H_{LC} on the tunability

In order to further improve the tunability of LSPR, a new set of simulations is performed. The height of gold nano-cylinder with elliptic basis is increased from $H_g =$ 75 nm to 150 nm with interval of 25 nm. Other parameters are fixed (height of LC cell

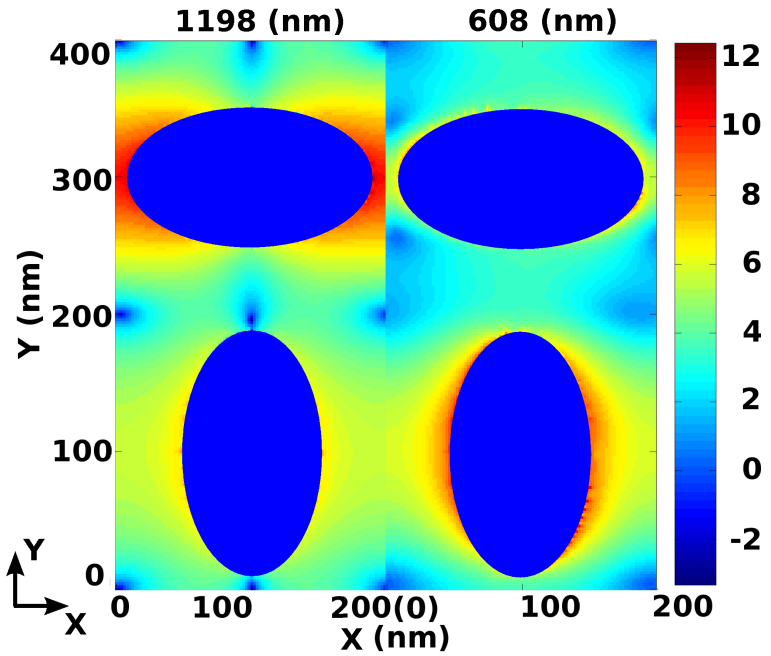

Fig. V.11 – Electric intensity distribution for resonance wavelength 1198 nm and 608 nm, respectively. Herein, major axis $2a = 175$ nm, minor axis $2b = 100$ nm, gold height $H_g = 75$ nm, height of LC cell $H_{LC} = 200$ nm.

Tab. V.14 – Gold nano-cylinders with elliptical basis. Gold height H_g increases from 75 nm to 150 nm. Other parameters are given as : $2a = 175\,\text{nm}, 2b = 100\,\text{nm}, P_x = 200\,\text{nm}, P_y = 400\,\text{nm}$. λ_0 is defined as the resonance wavelength position. $\Delta\lambda_\theta$ is the tunability of LSPR in the case perfect alignment of all LC molecules. $\Delta\lambda_{\theta_{max}}$ stands for the tunability with LCs anchoring effect taken into account.

H_g (nm)		75	100	125	150
$H_{LC} = 200$ nm	λ_0(nm)	1241	1243	1242	1233
	$\Delta\lambda_\theta$(nm)	64.86	78.42	85.85	91.90
	$\Delta\lambda_{\theta_{max}}$(nm)	42.55	55.00	66.12	71.68
$H_{LC} = 2H_g$	λ_0(nm)	1245	1244	1242	1234
	$\Delta\lambda_\theta$(nm)	77.04	85.85	93.26	97.68
	$\Delta\lambda_{\theta_{max}}$(nm)	49.97	55.00	66.23	63.41

H_{LC} : 200 nm, major axis $2a$: 175 nm, minor axis $2b$: 100 nm, periods P_x : 200 nm, P_y : 400 nm). Extinction spectra are computed in both cases of LC molecules under perfect alignment order and LC molecules with anchoring effect taken into account. Results are summarized in the first part of Tab. V.14.

We find that the tunability of LSPR improves with increasing height of gold nanoparticle regardless of LC molecules orientation. But the resonance position remains

Tab. V.15 – Gold nano-cylinders with elliptical basis. Gold height H_g increases from 75 nm to 150 nm. Other parameters are given as : $2a = 175\,\text{nm}, 2b = 50\,\text{nm}, P_x = 200\,\text{nm}, P_y = 400\,\text{nm}$. λ_0 is defined as the resonance wavelength position. $\Delta\lambda_\theta$ is the tunability of LSPR in the case perfect alignment of all LC molecules. $\Delta\lambda_{\theta_{max}}$ stands for the tunability with LCs anchoring effect taken into account.

H_g (nm)		75	100	125	150
H_{LC}=200 nm	λ_0(nm)	1264	1252	1234	1209
	$\Delta\lambda_\theta$(nm)	67.86	73.86	79.52	84.95
	$\Delta\lambda_{\theta_{max}}$(nm)	35.59	47.46	57.49	64.70
$H_{LC} = 2H_g$	λ_0(nm)	1264	1252	1236	1207
	$\Delta\lambda_\theta$(nm)	67.10	73.86	81.62	82.77
	$\Delta\lambda_{\theta_{max}}$(nm)	42.70	47.46	53.64	52.46

around 1240 nm, no matter whatever the gold height is. By comparing the shifts $\Delta\lambda_\theta$ and $\Delta\lambda_{\theta_{max}}$, anchoring effect obviously reduces the sensitivity $S = \frac{d\lambda}{dn}$. Nevertheless, the tunability has been drastically improved up to $\Delta\lambda_{\theta_{max}} = 71.68\,\text{nm}$ compared with our previous work (around 30 nm) [139].

Owing to the positive influence of $H_{LC} = 2H_g$ on the shift of LSPR [139], a further set of simulations is made using the same parameters as described above except of $H_{LC} = 2H_g$. The data are summarized in the second part of Tab. V.14. We can observe that the shift increases when H_g is lower than 125 nm, otherwise, a decrease will be obtained. The same conclusion is achieved by just decreasing the minor axis to 50 nm (see results in Tab. V.15).

In brief, from the comparison of results in Tab. V.14 and in Tab. V.15, resonance wavelength λ_0 is a blue-shifted with increased gold height. The tunability of LSPR has been improved up to 71.68 nm with anchoring effects taken into account, although anchoring effects drastically lower the tunability. Meanwhile, when the thickness of LC cell $H_{LC} = 200\,\text{nm}$, the tunability of LSPR obviously increases both with anchoring effect and perfect alignment cases. In contrast, when the thickness of LC cell H_{LC} is two times that of gold height H_g, a threshold value for gold height exists in 125 nm.

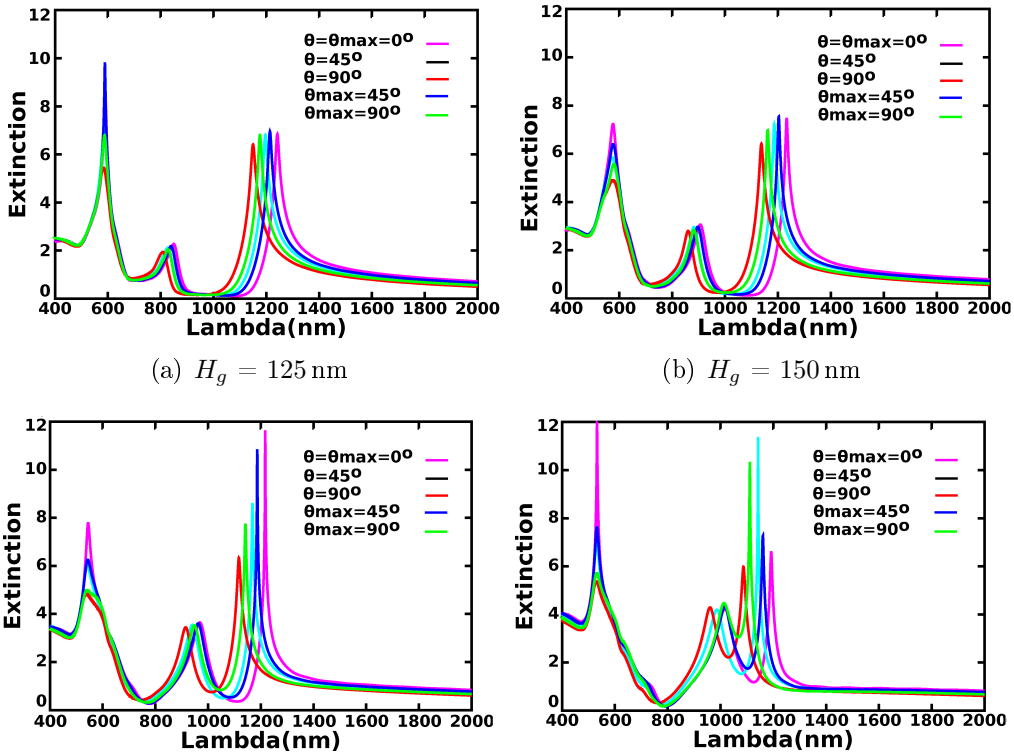

(a) $H_g = 125\,\text{nm}$ (b) $H_g = 150\,\text{nm}$

(c) $H_g = 175\,\text{nm}$ (d) $H_g = 200\,\text{nm}$

Fig. V.12 – Extinction spectra for different gold heights H_g (a) 125 nm, (b) 150 nm, (c) 175 nm, (d) 200 nm. Other parameters are fixed as $P_x = P_y = 200\,\text{nm}$, $2a = 175\,\text{nm}$, $2b = 100\,\text{nm}$ and $H_{LC} = 200\,\text{nm}$

V.4.6 Three resonances observed

The extinction spectra on Fig. V.12 exhibit three resonances for the structures we used. Here, the structure is described on Fig. V.9(d), parameters are the same with those presented in Tab. V.14 besides the gold height. The decreasing shift for $H_g > 125\,\text{nm}$ may be caused by the third resonance that appears at the middle.

The resonance observed at around 600 nm and the other resonance obtained at about 1200 nm almost remain constants when the gold height are increased. The middle resonance shifts greatly.

The middle resonance and the resonance observed at around 1200 nm will be investigated in section V.5. They can be obtained also in isotropic materials if H_g increases(see Fig.V.3(a) - Fig.V.3(d) in section V.2.3).

V.4.7 conclusion

In this section, we investigate the LSPR shift of gold nano-structures embedded in a LC cell as a function of the optical axis orientation of the LC molecules, by taking anchoring effects into account. Results are compared with the case of perfect alignment of LC molecules. It is found that anchoring effects strongly reduce the LSPR tunability, but modifications to the geometrical parameters of nano-structures can efficiently compensate it.

By varying the major axis orientation of gold nano-cylinder with elliptic basis(see Fig. V.9), the maximum tunability of LSPR is achieved up to $\Delta\lambda_{\theta_{max}} = 71\,\text{nm}$ with anchoring effect taken into account. It is more than two times than the LSPR tunability achieved before [139]. For LCs with perfect alignment, the maximum shift is $\Delta\lambda_{\theta} = 98\,\text{nm}$. Herein, double resonances are observed due to the different major axis orientation of gold-cylinders with elliptic basis. The double resonances for $H_g = 75\,\text{nm}$ are analyzed through electric intensity distribution maps. Further geometrical modifications are under consideration in order to achieve a greater LSPR tunability.

V.5 Double resonances structures and SERS application

In this section, the localized surface plasmon double resonance peak positions and the surface-enhanced raman scattering(SERS) gain (G_{SERS}) of an ordered gold nano-cylinders with elliptic basis array, embedded in a nematic liquid crystal (LC) media, are investigated using FDTD method. The influence of the anchoring effects between nematic LC molecules and glass substrate on the shift of the double resonance wavelength is taken into account, and results are compared with the case of a perfect alignment of the LC molecules and the isotropic materials. Finally, using different Raman band and two excitation wavelength at 590 nm and 632.8 nm, G_{SERS} are studied separately in the whole LCs cell.

V.5.1 Introduction

The double resonances of gold nano-particles extinction spectra have attracted some researchers' attentions [135; 140; 141; 142], as higher enhancement are offered than with similar structures with single resonances [143]. In the previous works, the double resonances resulted from the use of mixed dimers : pairs of nano-particles with different shapes [140], asymmetric gold nano-crosses [141], and the hybridization of LSPRs of metal nano-particles array [142].

In this section, we propose a different method to accomplish double resonances : gold nano-cylinders with elliptic basis surrounding different environment sandwiched between two glass substrates. We compare the positions of double resonance wavelength using different isotropic materials (the index varies from n_o=1.53 to n_e=1.74) to those using anisotropic materials (nematic liquid crystals). For the LCs, considering the anchoring effects at the interface of LC molecules and the glass substrates, the extinction spectra are compared with those with a perfect alignment of LC molecules. In addition, the SERS enhancement factors of the structures are estimated using different Raman band(1200 cm^{-1}, 1600 cm^{-1}, 1800 cm^{-1}, 2000 cm^{-1}) and excitation wavelength(590 nm, 632.8 nm).

V.5.2 Structures

The nano-particles we investigated are gold cylinders with elliptical basis, with major axis $2a = 125$ nm (parallel to x-axis), minor axis $2b = 50$ nm (parallel to y-axis), and height $H_g = 200$ nm. Periodicities of the metallic nano-particles array (distance center-center) are $P_x = P_y = 200$ nm. Free space between particles is filled with a nematic liquid crystal. We will use the parameters of the commercially available E7 liquid crystal [125; 124; 119; 144], with ordinary index n_o=1.53, and extraordinary index $n_e = 1.74$ as those used in previous sections.

Two cases will be considered : without anchoring effect, that is all molecules are aligned parallel to an external electric field, and with anchoring effect between the LC molecules and glass substrates. A schematic representation of the structure is presented in Fig. V.13.

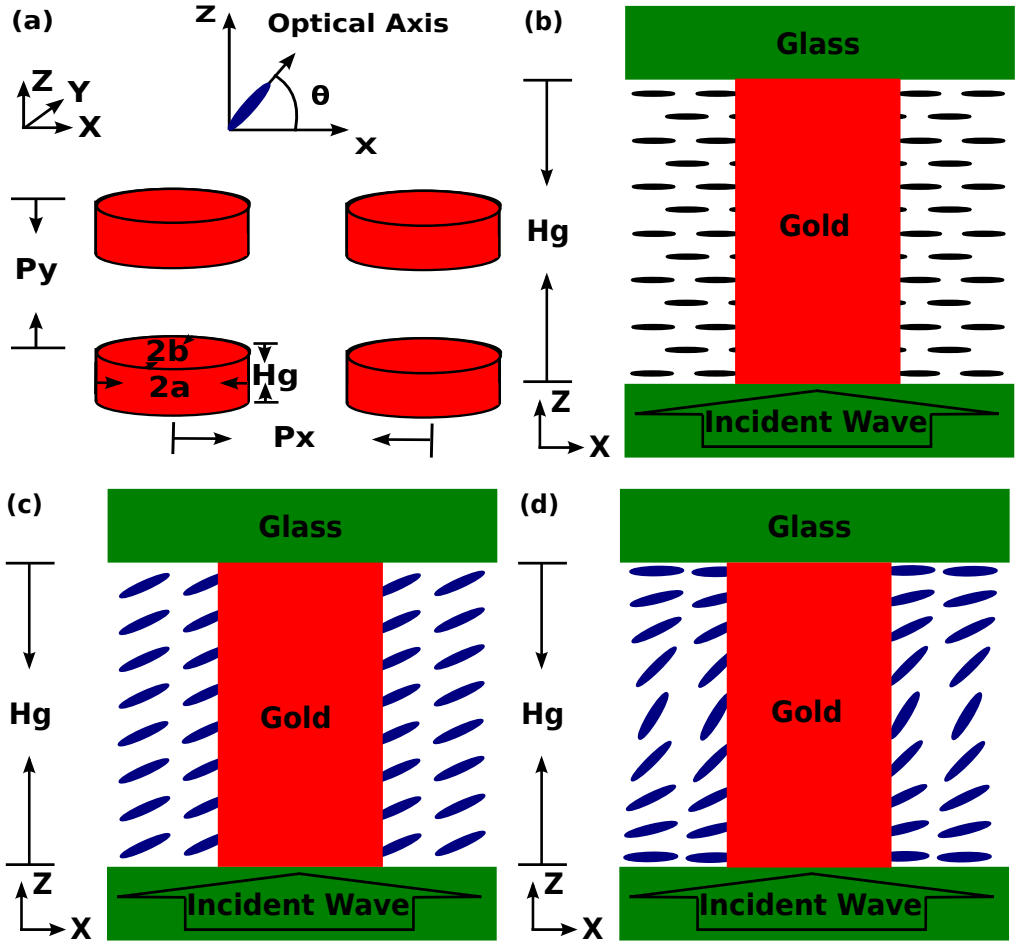

Fig. V.13 – Description of the structures and LC orientation. (a) Orientation of LCs and gold array, (b) gold nano-particles surrounded by isotropic materials, (c) gold nano-particles surrounded by LCs with perfect alignment and (d) gold nano-particles surrounded by LCs with anchoring effect.

V.5.3 Gold particles surrounded by isotropic material

Resonance positions are determined by calculation of extinction spectra. We first consider gold nano-cylinders with elliptic basis sandwiched with glass substrates surrounded by isotropic material. The refractive index corresponding special material are tested, they are n= 1.0(air), n=1.333(water), n=n_o=1.53(ordinary index of LC E7), n=1.60(the mean index of LC) n=n_e=1.74(extraordinary index of LC E7), n=2.01(SiN4). Extinction spectra are described on Fig. V.14

The extinction spectra implies that double resonances firstly become closer and sharper if the index increases and then become one resonance peak if the index increases further.

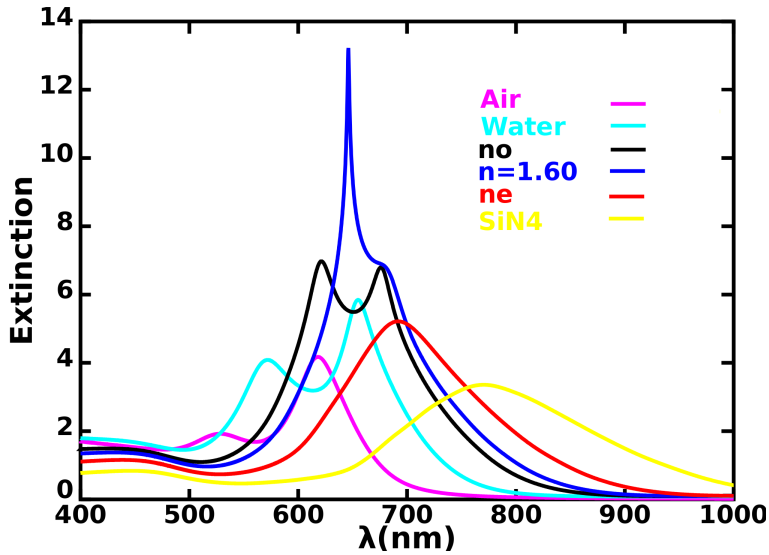

Fig. V.14 – Extinction spectra as a function of wavelength, for the isotropic materials n = 1.0(air), n = 1.333(water), n = n_o = 1.53(ordinary index of LC E7), n = 1.60(the mean index of LC), n = n_e = 1.74(extraordinary index of LC E7), n = 2.01(SiN4).

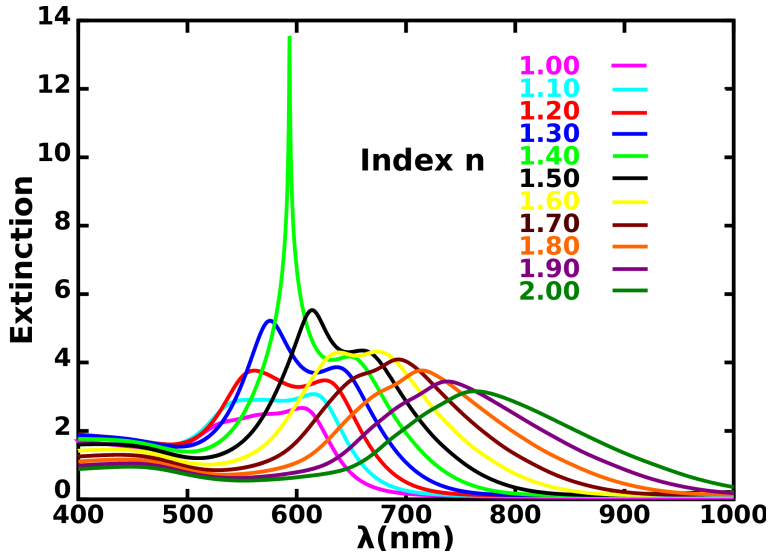

Fig. V.15 – Extinction spectra as a function of wavelength, for the isotropic materials index n=1.00, 1.20, 1.30, 1.40, 1.50, 1.60, 1.70, 1.80, 1.90, 2.00

Subsequently, we do the simulations for gold particles deposited on glass substrate surrounded by isotropic material also, except that the upper glass substrate is canceled. The structure parameters are same as those above. Index of the isotropic material changes from n=1.00 to n=2.00 with the interval of dn=0.10. Extinction spectra are described on Fig. V.15. Here, the double resonances are achieved again. Firstly, they become closer and sharper and then unite also when the index increases.

In fact, the extinction spectra are calculated using isotropic materials surrounding gold nano-particles. The index varies from n=1.00 to n=2.00 with interval dn=0.01 for both with the upper substrate(glass) or without it. the spectra are exhibited partly on Fig. V.14 and Fig. V.15.

In order to investigate the origin of double resonances and the influence of LC on them, isotropic medium, with refractive index varying from n=1.53 to n=1.74 with interval dn=0.03, is chosen as surrounding materials for gold nano-particles. the index is between previously defined values n_o=1.53 and n_e=1.74 for LC.

Results are described on Fig. V.16(a). A double resonance feature can be observed in the spectra. When n = 1.60, the left resonance is sharper than others, which can be related to the fact that the imaginary part of gold nano-particles permittivity reaches its lower value.

In order to study the shift of the two resonances, we fit the spectra using a combination of two lorentzian and one gaussian function, the latter being used for the background description :

$$s(\omega) = a_0 + \frac{a_1}{1 + (\frac{\omega - \omega_1}{c_1})^2} + \frac{a_2}{1 + (\frac{\omega - \omega_2}{c_2})^2} + a_3.e^{-\frac{(\omega - \omega_3)^2}{c_3}}, \qquad \text{(V.2)}$$

with ω_1 and ω_2 the frequencies of the two resonances.

An example is given on Fig. V.17 for $n = 1.54$.

Double resonance peak position described in Fig. V.16(a) are given in Fig. V.16(b). The black curve in Fig. V.16(b) can be explained using the cavity resonance mode (green curve), given by $\frac{\lambda}{2} = h.n$ [145], and the blue curve corresponds to the transverse resonance.

Fitting results for the spectra corresponding Fig. V.14, index with interval of dn=0.01, are plotted on Fig. V.18.

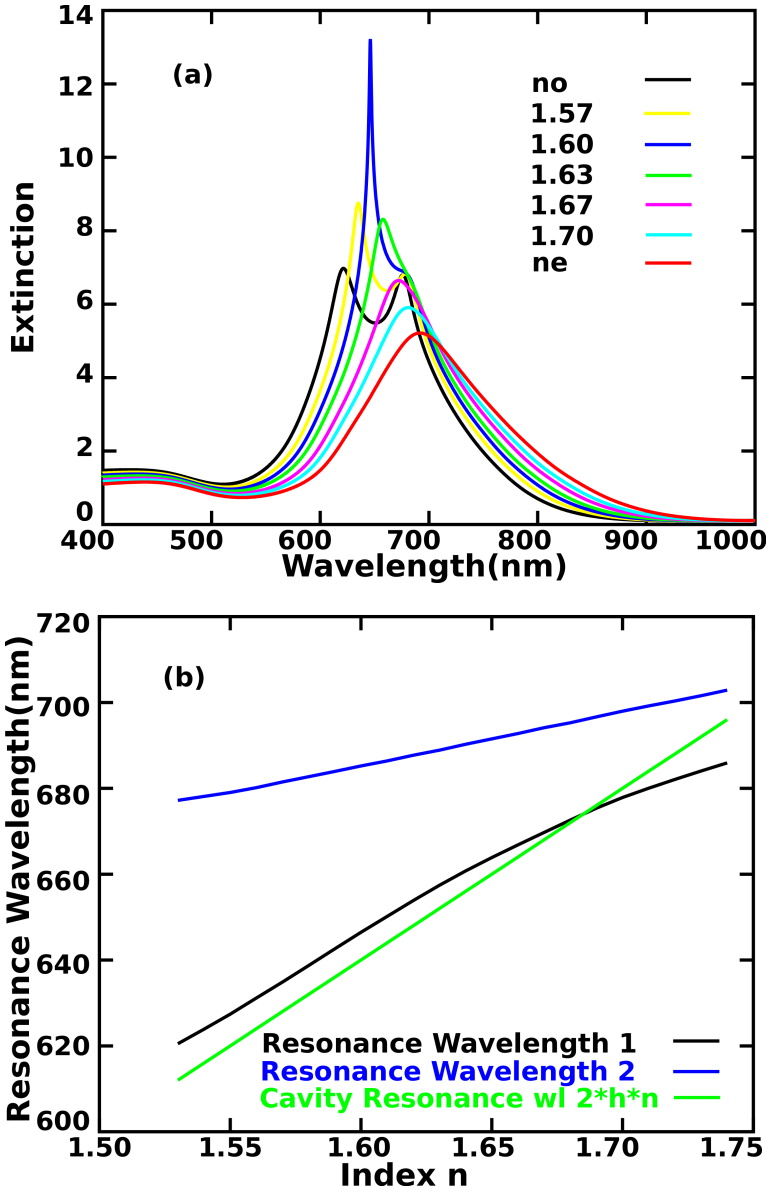

Fig. V.16 – Extinction spectra and resonance positions as a function of index. (a) Extinction spectra of gold nano-particles surrounded by isotropic materials as a function of excitation wavelength, surrounding medium index varies from $n_o = 1.53$ to $n_e = 1.74$; (b) resonance positions for gold nano-particles surrounded by isotropic materials.

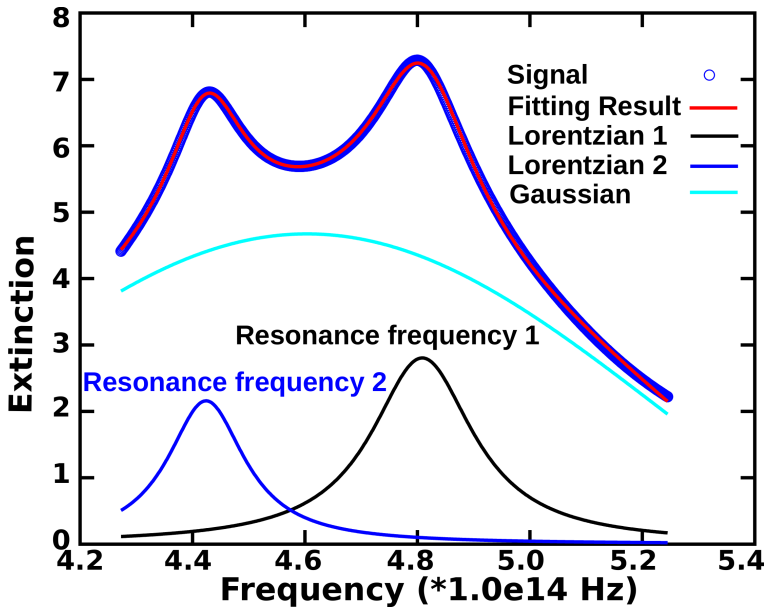

Fig. V.17 – Fitting of extinction spectrum as a function of frequency, n=1.54.

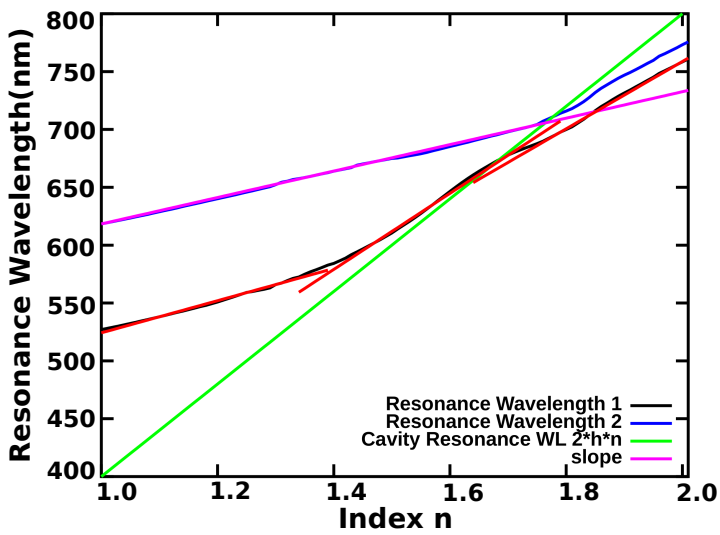

Fig. V.18 – The curve fitting of extinction spectrum as a function of frequency, index from n=1.00 to n=2.00. Using Eq.V.2 to describe the extinction spectrum.

V.5.4 Gold nano-particles surrounded by LC

In order to investigate the extinction spectra of gold nano-particles embedded in LC cell, two series of simulations are performed.

First, perfectly aligned LC molecules surrounding gold nano-particles are simulated using FDTD method, the schematic is described in Fig. V.13(c). Extinction spectra are plotted as the function of the angle θ in Fig. V.19(a). θ can be modified by an external electric field, meanwhile, θ is constant when the external field is fixed. Indeed, the change of orientation of LCs lead to a local variation of the permitivity surrounding nano-particles. Therefore, shifts of resonance peaks can be observed. In our case, the resonances peak positions are described by solid lines in Fig. V.19(c) as a function of the index in the x-direction $n = \frac{n_o n_e}{\sqrt{n_e^2 \sin^2\theta + n_o^2 \cos^2\theta}}$; they are very close to those obtained using isotropic materials as surrounding materials described in Fig. V.16(a).

With anchoring effects taken into account at the interface between the LC molecules and the glass substrates, the spectra are described for various θ_{max} in Fig. V.19(b), where θ_{max} is the maximum tilted angle of LCs, which appear at the middle of the studied LC cell [139; 32]. The schematic is showed in Fig. V.13(d), and the resonance wavelength positions are described by dashed lines in Fig. V.19(c).

Comparing extinction spectra on Fig. V.16(a), Fig. V.19(a) and Fig. V.19(b), and the fitting results on Fig. V.19(c), we observe that nano-particles embedded in LCs (without anchoring effects) behaves optically like the nano-particles in isotropic medium [121]. Both resonances wavelengths exhibit a blue-shift by decreasing the index surrounding gold nano-particles or by decreasing the index in the incident polarization direction by changing the orientation of LC molecules from $\theta = 0^o$ to $\theta = 90^o$ [128; 130].

For gold nano-particles embedded in LCs with anchoring effects, the refractive index at the middle of the structure is slightly smaller than the index near the glass substrate. In this case, the two resonance peaks move in two opposite directions when we tune the orientation of LC molecules using external electric field ; while the cavity mode is weakly affected, the plasmon resonance exhibit an unexpected blue shift as the effective index is increased.

With anchoring effects taken into account at $\theta_{max} = 90^o$, the on-resonance electric

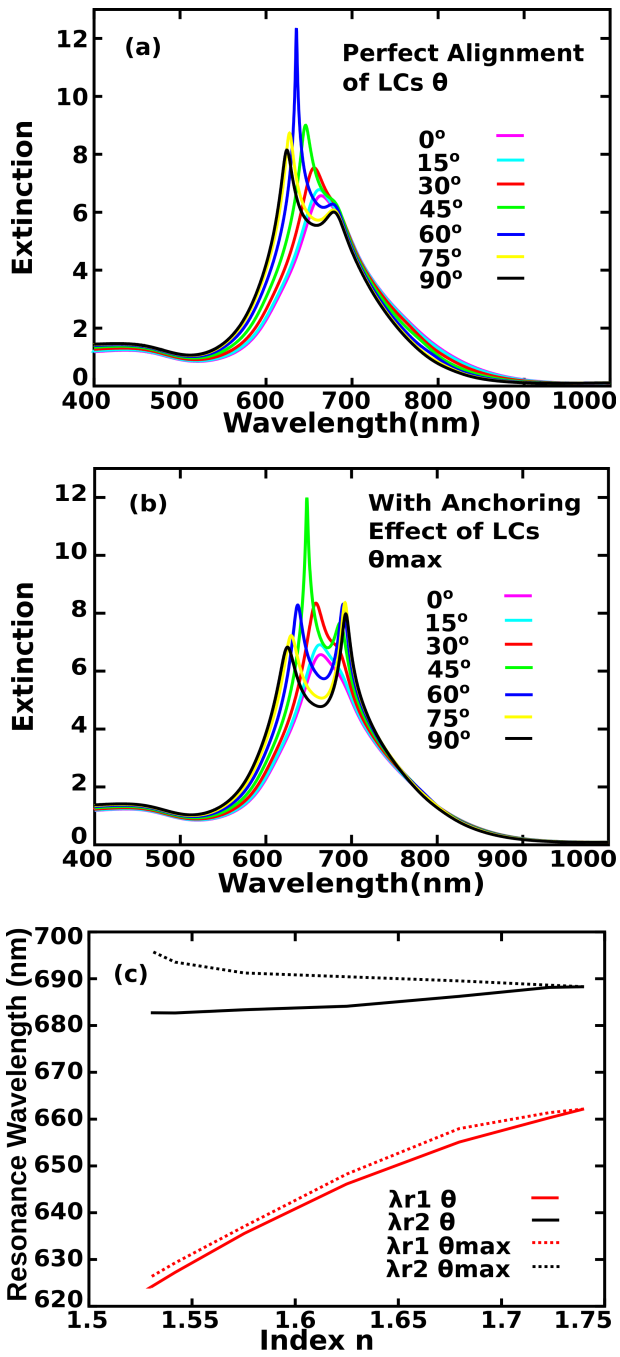

Fig. V.19 – Extinction spectrum of gold nano-particles surrounded by LCs (a) with perfect alignment and (b) with anchoring effects taken into account. (c) Double resonance positions of extinction spectrum : solid lines for LCs with perfect alignment, dashed lines for LCs with anchoring effects taken into account.

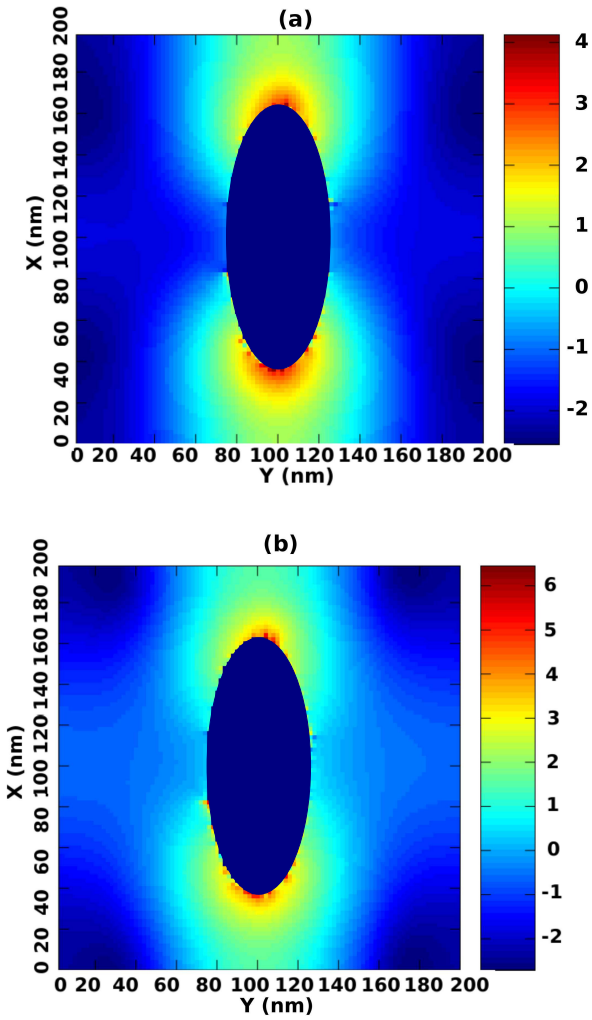

Fig. V.20 – Electromagnetic intensity distribution ($log(|E|^2)$) in xy plane for LCs with anchoring effects taken into account, $\theta_{max} = 90^o$ for instance. Electromagnetic intensity distribution at resonance wavelength : (a) λ_{r1}=624 nm and (b) λ_{r2}=695 nm.

field intensity maps ($log(|E|^2)$), at wavelengths 624 nm and 695 nm, in xy-plane at the middle of the structure are described on Fig. V.20. It can be observed that the electric field intensity is stronger at $\lambda_{r2} = 695$ nm than at $\lambda_{r1} = 624$ nm, which is in agreement with the extinction spectra values for these two wavelengths.

Intensity maps in xz plane and in yz plane at resonance for $\theta_{max} = 0^o$ and $\lambda = 663$ nm are compared with those calculated when the orientation of LCs is described by $\theta_{max} = 90^o$ (and $\lambda_{r1} = 624$ nm, $\lambda_{r2} = 695$ nm) on Fig. V.21. We can again verify that intensities are stronger when extinction spectra values are higher, i.e. in the case $\theta_{max} = 90^o$, and for $\lambda_{r2} = 695$ nm.

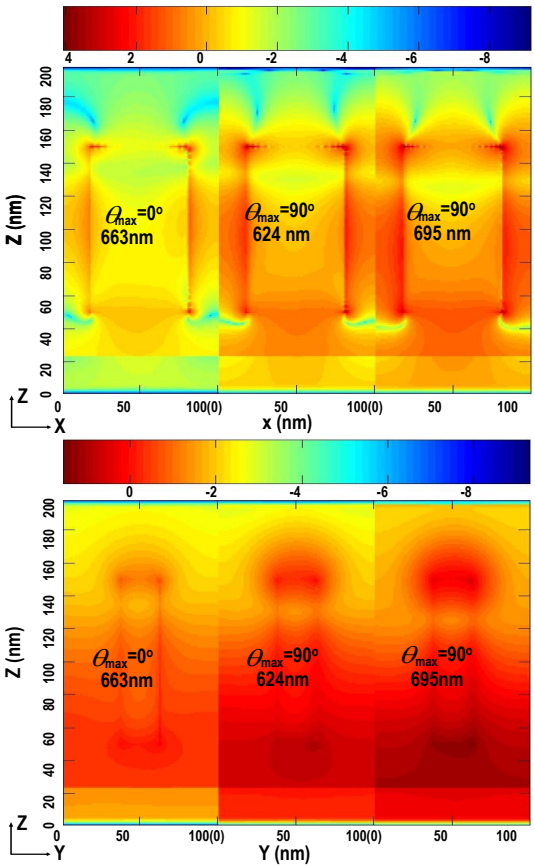

Fig. V.21 – Electromagnetic intensity distribution ($log(|E|^2)$) in xz plane and in yz plane at the middle of the structure, for LC orientation $\theta_{max} = 90^o$, λ_{r1} =624 nm, $\lambda_{r2} = 695$ nm, for the orientation $\theta_{max} = 0^o$, λ_r =663 nm.

V.5.5 SERS gain

To further investigate this structure, the average SERS gain of the local gains over one period of the array in the whole LCs cell [146] are computed. The average SERS gain $\overline{G_{sers}}$ at one plane is proportional to [146; 57] :

$$\overline{G_{sers}} = \frac{1}{N}\sum_{x_i}\sum_{y_i} G_{sers(x_i,\ y_i)} = \frac{1}{N}\sum_{x_i}\sum_{y_i} |\frac{E_{loc}(\lambda_{exc})E_{loc}(\lambda_{Raman})}{E_{inc}(\lambda_{exc})E_{inc}(\lambda_{Raman})}|^2, \tag{V.3}$$

where N is the number of Yee cells in one period of structure, and i, j are coordinates of each cell.

Assuming the molecules are uniformly distributed in the whole LC cell, we collect the values of the electric field on three planes in xy plane(the bottom, the top and the

middle of LCs cell) after each step of calculation. Then the SERS gain(G_{SERS}) at the whole cell is approximated by the average of $\overline{G_{sers}}$ on the three planes.

The Raman bands we considered are 1200 cm^{-1}, 1600 cm^{-1}, 1800 cm^{-1} and 2000 cm^{-1} respectively. The results of the influence of the anchoring effect on the G_{SERS} are compared with those with perfectly aligned LC molecules. Extinction spectra and G_{SERS} are compared in Fig. V.22.

From these series of simulations, we can conclude that G_{SERS} decreases when Raman bands increase from 1200 cm^{-1} to 2000 cm^{-1}, and the orientation of LC molecules and the anchoring effects do not affect this phenomenon.

Meanwhile, the peak of G_{SERS} becomes broader and exhibits a blue shift when the Raman band is increased. Around 670 nm, G_{SERS} exhibits a second peak also. In a analogous fashion, G_{SERS} is enhanced if the Stokes scattering is in resonance with the localized surface plasmons of the metal particles.

This second peak becomes more important and the intensity is stronger than the first peak for Raman bands 1800 cm^{-1} and 2000 cm^{-1} at $\theta = 45^o$ or 90°.

Therefore, we can conclude that by changing the orientation of LCs, the LSPR double resonance peak positions are modified, and the sensitivity of SERS substrate is also modified. We have plotted the SERS gain for different Raman bands on Fig. V.22. We can observe that Raman spectra intensity are stronger when the incident wavelength varies from 580 nm to 680 nm. Meanwhile, SERS enhancement is found between the double resonance peaks and the positions can be controlled.

Furthermore, the Raman enhancement for the excitation wavelength fixed at λ_{exc} = 590 nm and λ_{exc} = 632.8 nm are described as a function of the Raman band in Fig. V.23, where M corresponds to the maximum G_{SERS} value, and B gives the Raman band that corresponds to the maximum SERS gain.

For the Raman bands from 0 cm^{-1} to 4000 cm^{-1}, comparing SERS gain for an incident wavelength equal to 632.8 nm and those when the incident wavelength is 590 nm, we note that, in the first case, G_{SERS} is stronger with or without anchoring effect taken into account. G_{SERS} peak is narrower also. For the incident wavelength at 590 nm, G_{SERS} peak is broad and almost constant when the band varies from 900 cm^{-1} to

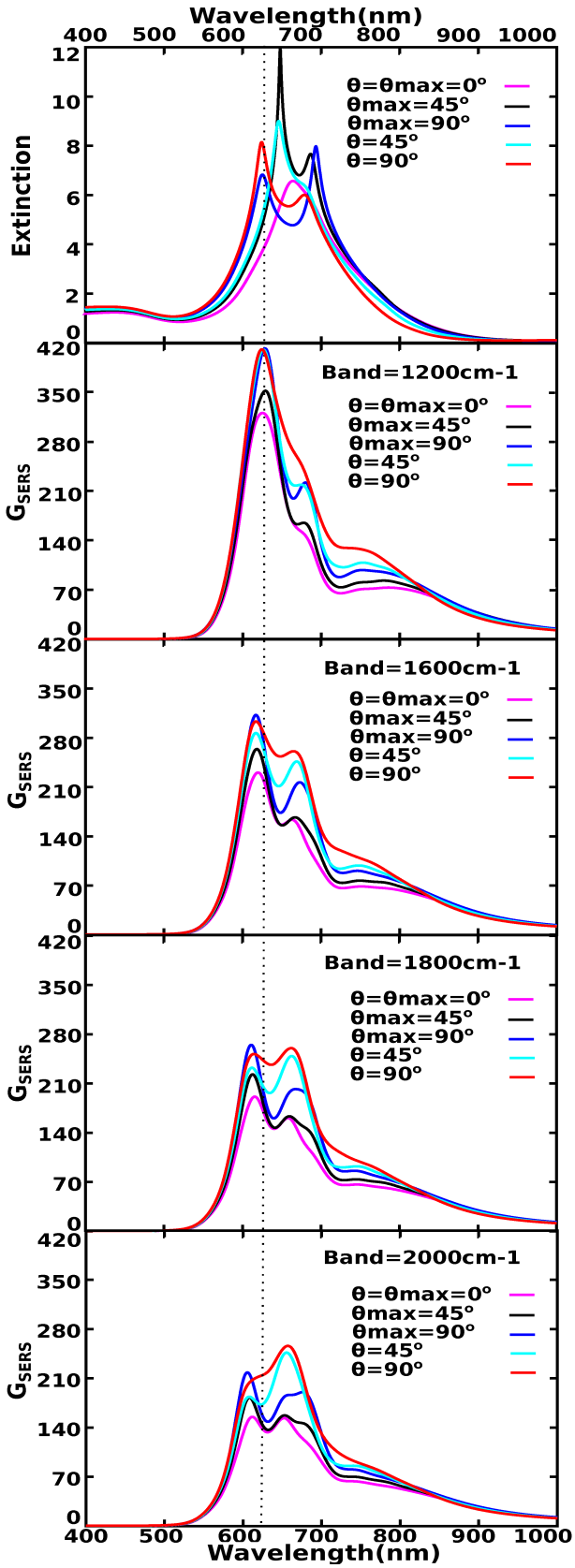

Fig. V.22 – G_{SERS} using Raman band $1200\,\mathrm{cm}^{-1}$, $1600\,\mathrm{cm}^{-1}$, $1800\,\mathrm{cm}^{-1}$, $2000\,\mathrm{cm}^{-1}$ and extinction spectra.

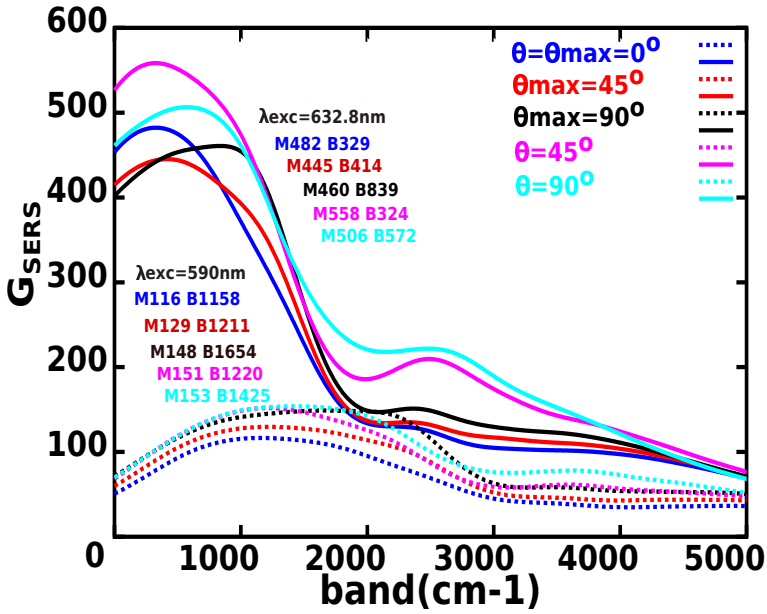

Fig. V.23 – G_{SERS} with excitation wavelength fixed at 590 nm and 632.8 nm. M implies the maximum G_{SERS} value, B gives the Raman band that corresponds to the maximum SERS gain.

2100 cm^{-1}, which implies that different bands of a specific molecule may be easily detected using this wavelength. Further work will be focused on the improvement of G_{SERS} as well as the influence of the orientation of LCs on the SERS gain.

V.5.6 Conclusion

In this work, using an ordered array of gold cylinder with elliptic basis embedded in a nematic liquid crystal (LC), localized surface plasmon and cavity mode resonance peak positions as well as Surface-Enhanced Raman Scattering(SERS) gain (G_{SERS}) were investigated using the FDTD method.

By changing the orientation of the LC molecules, both resonances positions can be tuned. The influence of the anchoring effects between nematic LC molecules and glass substrate on the tuning is studied, and we have found that the shift of the LSPR is modified when anchoring is taken into account, by comparison with the case of an isotropic medium or with LC without anchoring.

Finally, the SERS gain as a function of the incident wavelength is computed in the whole LCs cell using different Raman bands (1200 cm^{-1}, 1600 cm^{-1}, 1800 cm^{-1},

2000 cm^{-1}), which exhibits a double peak also. For two excitation wavelengths (590 nm and 632.8 nm), SERS gains are compared. Due to the SERS gain peak at 590 nm, this wavelength may be more suitable for the detection of many Raman bands at the same time.

We anticipate that this work will offer an aid for the design and the fabrication of SERS substrates. Some future work should focus on the influence of the shape and size of nano-particles with anchoring effects of LCs on the double resonance and the G_{SERS} intensity.

Chapitre VI

Conclusion

Metal nanoparticles have unique optical properties, the control and optimization have a growing interest in fundamental research as same as applied research. A spectacular property of these nanoparticles is the localized surface plasmon resonance (LSPR), which is a consequence of the oscillations of free electrons at the interface between metal and dielectric.

The spectral position of the plasmon resonance is largely dependent on the geometry of the nanoparticles, but also on the dielectric properties of the surrounding medium. It implies that the variation of the index of the medium surrounding the metallic nanostructures can lead to the LSPR resonance. Nematic liquid crystals are a great way to modify and control the plasmon resonance. Indeed, rotation of the liquid crystal molecules can induce a change in refractive index. As an application of LSPR, the surface-enhanced raman scattering (SERS) becomes a hot topic also.

The aim of the thesis is to simulate arrays of gold nanoparticles in a nematic liquid crystal in order to predict the influence of the orientation of the LC molecules on the optical properties of these nanostructures.

Numerical method we used is based on the finite difference time domain (FDTD) method. Herein, Yee grid describes the electromagnetic field components. Constitutional perfectly matched layer (CPML), as an advanced absorbing boundary condition, is chosen due to its complete independence on the host medium. Thus, we do not need to do any modification if we apply CPML to inhomogeneous, anisotropic dispersive, lossy or nonlinear media. Dispersive properties of gold nano-particles, anisotropic properties of LCs and anchoring effects between liquid crystal cell and the substrates, are completed in our programs.

In this work, using an ordered array of gold cylinders embedded in a nematic liquid crystal (LC), localized surface plasmon resonance peak positions [139] and surface-enhanced raman scattering (SERS) gain (G_{SERS}) [147] were investigated. The influence of the anchoring effects between nematic LC molecules and glass substrate on the tuning is studied, and we have found that the shift of the LSPR is decreased when anchoring effect is taken into account, by comparison with the case of an isotropic medium or with LC with perfect alignment. But modifications to the geometrical parameters of nano-structures can efficiently compensate it. The maximum tunability of LSPR is achieved up to $\Delta\lambda_{\theta_{max}} = 71\,\mathrm{nm}$ with anchoring effect taken into account. For LCs with perfect alignment, the maximum shift is $\Delta\lambda_{\theta} = 98\,\mathrm{nm}$. Herein, double resonances and G_{SERS} intensity are studied for special gold-cylinders with elliptic basis.

Topics introduced in this thesis could provide a basic knowledge of liquid crystal, LSPR and FDTD. We anticipate that this work will offer an aid for the design and the fabrication of SERS substrates , even sensors.

Finally, many further work is needed to do in plasmonics. For example, up to now, the FDTD numerical method can only solve classical electromagnetic problems. While the distance among noble nano-particles decreases, the field intensity is enhanced obviously. But this enhancement is not unlimited. When the distance is as small as a few nanometers, the enhanced field becomes weaker. Meanwhile, plasmon resonances become difficult to describe using classical method [148]. Non-linear effects are driven to explain this phenomenon. Some researchers describe this phenomenon as quantum effects [149]. A quantum-corrected model (Drude model) is produced to bridge quantum mechanism and classical framework [150; 151; 152]. But shortcomings of this model exist also. In the future, I will try to find a way to well describe this phenomenona.

Résumé

VI.1 Introduction

Les nanoparticules métalliques ont des proprietés optiques uniques, dont le contrôle et l'optimisation présentent un interêt grandissant tant pour la recherche fondamentale qu'appliquée. Une propriéte bien connue de ces nanoparticules est la résonance plasmon de surface localisée, qui est une conséquence des oscillations des electrons libres à l'interface métal/diélectrique. La position spectrale de la résonance plasmon est largement dépendante de la géométrie des nanoparticules, mais aussi de la constante dieletrique du milieu environnant. Un moyen pour contrôler cette résonance consiste donc à modifier l'indice du milieu qui entoure les nanostructures.
Les cristaux liquides nématiques sont un excellent outil pour modifier et contrôler la résonance plasmon. En effet, par rotation des molécules du cristal liquide on peut induire un changement d'indice. L'objectif de la thèse est de simuler des réseaux de nanoparticules d'or entourées par un cristal liquide nématique et de prédire l'influence de l'orientation du cristal liquide sur les propriétés optiques de ces nanostructures. Le formalisme numérique utilisé est basé sur la méthode des différences finies dans le domaine temporel (FDTD). L'influence de l'ancrage des molécules de cristaux liquides aux interfaces de la cellule est étudiée, et les résultats sont comparés avec le cas d'une orientation parfaite des moléculrs dans toute la cellule.

VI.2 Méthode numérique

La méthode des différences finies dans le domaine temporel (FDTD) fournit une prévision précise de la propagation des ondes électromagnétiques. Nous passerons en revue les développements de la FDTD, puis présenterons les principales techniques que nous avons utilisées dans notre travail, dont les conditions aux limites absorbantes,

les modèles numériques pour la description des matériaux dispersifs et des matériaux anisotropes.

Présentation de la méthode FDTD

La méthode FDTD est une méthode largement établie pour l'étude de l'interaction entre une onde électromagnétique et une structure quelconque [68; 69]. Elle a été proposée pour la première fois par Yee en 1966 [27]. Les dérivés temporelles et spatiales dans les équations de Maxwell sont discrétisées, ce qui permet de déduire les champs électromagnétiques à l'instant $t+1$ à partir des valeurs connues à l'instant t.

Une des difficultés liée à la méthode est l'absorbtion des ondes sortants aux frontières du domaine de calcul. Différentes méthodes plus ou moins satisfaisantes ont été proposées, mais la première véritable avancée a été effectuée par Bérenger grâce à sa Perfectly Matched Layer (PML) en 1994[77], qui permettait une absorption quasi indépendante de l'angle de propagation par raport à la frontière. Par la suite, Gedney [78], Sacks et ses collègues [79] ont introduit un milieu anisotrope (UPML) pour la troncature des fenêtres de calcul. Enfin, la Convolutioanl PML (CPML) a été introduite par Roden en 2000 [80]. L'utilisation de la CPML permet de ne pas avoir à modifier l'algorithme quelque soit l'endroit où l'on se trouve dans la fenêtre de calcul.

Algorithme de Yee

Considéront une région sans charges ($\rho = 0$) et sans courants ($\overrightarrow{J} = 0$), mais avec des matériaux qui absorbent l'énergie du champ électromagnétique.

Pour les matériaux de permittivité relative ε_r et de perméabilité relative μ_r, nous pouvons définir $\overrightarrow{D}$ et $\overrightarrow{E}$, $\overrightarrow{B}$ et $\overrightarrow{H}$ en utilisant

$$\begin{aligned} \overrightarrow{D} &= \varepsilon \overrightarrow{E} = \varepsilon_r \varepsilon_0 \overrightarrow{E} \\ \overrightarrow{B} &= \mu \overrightarrow{E} = \mu_r \mu_0 \overrightarrow{E} \end{aligned} \tag{VI.1}$$

où ε_0 et μ_0 sont la permittivité et la perméabilité dans le vide, respectivement.

Toute fonction u est décrite en un point discret dans le grille de Yee et en un point discret dans le temps comme :

$$u(i\Delta x, j\Delta y, k\Delta z, n\Delta t) = u^n_{i,j,k} \tag{VI.2}$$

Field Components		Space points			Time points
		X axis	Y axis	Z axis	
E	Ex	i+1/2	j	k	n
	Ey	i	j+1/2	k	
	Ez	i	j	k+1/2	
H	Hx	i	j+1/2	k+1/2	n+1/2
	Hy	i+1/2	j	k+1/2	
	Hz	i+1/2	j+1/2	k	

Fig. VI.1 – Positions des composantes des vecteurs champ électrique et magnétique dans la grille de Yee.

où i, j, k, n sont des entiers. $\Delta x, \Delta y$, et Δz sont les discretisations spatiales du système de coordonnées cartésiennes suivant x, y et z. En outre, les positions des composantes du vecteur champ électrique et magnétique sur une maille cubique de l'espace treillis Yee sont présentées sur la Fig. VI.1.

Les conditions initiales pour les champs électriques et magnétiques sont nulles partout dans la grille. En combinant l'équation VI.1 et l'équation VI.2, l'approximation numérique des équations de Maxwell peut être obtenue. Par exemple, la composante E_x peut être écrite comme suit :

$$\frac{\partial E_x}{\partial t} = \frac{1}{\varepsilon}[\frac{\partial H_z}{\partial y} - \frac{\partial H_y}{\partial z} - (J_{sourcex} + \sigma E_x)] \tag{VI.3}$$

où σ est la conductivité électrique du matériau, $J_{sourcex}$ est la composante x de la densité de courant de la source. D'après la Fig. VI.1, on obtient pour $E_x(i+1/2, j, k, n)$:

$$\begin{aligned}\frac{E_x|^{n+1/2}_{i+1/2,j,k} - E_x|^{n-1/2}_{i+1/2,j,k}}{\Delta t} =& \frac{1}{\varepsilon_{i+1/2,j,k}}\{\frac{H_z|^n_{i+1/2,j+1/2,k} - H_z|^n_{i+1/2,j-1/2,k}}{\Delta y} \\ &- \frac{H_y|^n_{i+1/2,j,k+1/2} - H_y|^n_{i+1/2,j,k-1/2}}{\Delta z} \\ &- J_{sourcex}|^n_{i+1/2,j,k} - \sigma_{i+1/2,j,k} E_x|^n_{i+1/2,j,k}\}\end{aligned} \tag{VI.4}$$

Les valeurs E_x au pas de temps n ne sont pas supposées être stockées dans la mémoire de l'ordinateur au cours des simulations, mais les valeurs précédentes de E_x au pas de temps $n-1/2$ le sont. Ensuite, le terme $E_x|^n_{i+1/2,j,k}$ sur le côté droit de l'équation VI.4 doit être modifié en utilisant l'approximation $E_x|^n_{i+1/2,j,k} = \dfrac{E_x|^{n+1/2}_{i+1/2,j,k} + E_x|^{n-1/2}_{i+1/2,j,k}}{2}$.

On obtient des résultats numériquement stables et précis pour des valeurs de σ

allant de zéro à l'infini. Et donc finalement on obtient $E_x|_{i+1/2,j,k}^{n+1/2}$:

$$E_x|_{i+1/2,j,k}^{n+1/2} = \left(\frac{1-\frac{\sigma_{i+1/2,j,k}\Delta t}{2\varepsilon_{i+1/2,j,k}}}{1+\frac{\sigma_{i+1/2,j,k}\Delta t}{2\varepsilon_{i+1/2,j,k}}}\right)E_x|_{i+1/2,j,k}^{n-1/2} + \frac{\frac{\Delta t}{\varepsilon_{i+1/2,j,k}}}{1+\frac{\sigma_{i+1/2,j,k}\Delta t}{2\varepsilon_{i+1/2,j,k}}}\left\{\frac{H_z|_{i+1/2,j+1/2,k}^{n} - H_z|_{i+1/2,j-1/2,k}^{n}}{\Delta y} - \frac{H_y|_{i+1/2,j,k+1/2}^{n} - H_y|_{i+1/2,j,k-1/2}^{n}}{\Delta z} - J_{sourcex}|_{i+1/2,j,k}^{n}\right\} \tag{VI.5}$$

De même, les expressions de E_y, E_z, H_x, H_y, et H_z peuvent être déduites en utilisant l'algorithme Yee.

La condition de stabilité de l'algorithme est :

$$\Delta t < \frac{1}{c\sqrt{\frac{1}{(\Delta x)^2}+\frac{1}{(\Delta y)^2}+\frac{1}{(\Delta z)^2}}}, \tag{VI.6}$$

Si $\Delta x = \Delta y = \Delta z = \Delta$, on a donc $\Delta t < \frac{\Delta}{\sqrt{3}c}$ [83].

Conditions aux limites absorbantes

On présente pour l'exemple la composante x de la loi d'Ampère :

$$\begin{aligned}(\varepsilon\frac{\partial}{\partial t}+\sigma_y)E_{xy} &= \frac{\partial}{\partial y}(H_{zx}+H_{zy})\\ (\varepsilon\frac{\partial}{\partial t}+\sigma_z)E_{xz} &= -\frac{\partial}{\partial z}(H_{yx}+H_{yz})\end{aligned} \tag{VI.7}$$

De même, la loi de Faraday est décrite par

$$\begin{aligned}(\mu\frac{\partial}{\partial t}+\sigma_y^*)H_{xy} &= -\frac{\partial}{\partial y}(E_{zx}+E_{zy})\\ (\mu\frac{\partial}{\partial t}+\sigma_z^*)H_{xz} &= -\frac{\partial}{\partial z}(E_{yx}+E_{yz})\end{aligned} \tag{VI.8}$$

Pour l'onde d'incidence normale(θ =0), en utilisant la méthode de la convolution récursive [86; 87], la quantité auxiliaire ψ est introduite. Ensuite, la mise à jour explicite

pour E_x est déduite, en comparant avec Eq. VI.5 :

$$
\begin{aligned}
E_x|_{i+1/2,j,k}^{n+1/2} =& \left(\frac{1-\dfrac{\sigma_{i+1/2,j,k}\Delta t}{2\varepsilon_{i+1/2,j,k}}}{1+\dfrac{\sigma_{i+1/2,j,k}\Delta t}{2\varepsilon_{i+1/2,j,k}}}\right)E_x|_{i+1/2,j,k}^{n-1/2}+ \\
& \frac{\dfrac{\Delta t}{\varepsilon_{i+1/2,j,k}}}{1+\dfrac{\sigma_{i+1/2,j,k}\Delta t}{2\varepsilon_{i+1/2,j,k}}}\left\{\frac{H_z|_{i+1/2,j+1/2,k}^{n}-H_z|_{i+1/2,j-1/2,k}^{n}}{k_y\Delta y}-\frac{H_y|_{i+1/2,j,k+1/2}^{n}-H_y|_{i+1/2,j,k-1/2}^{n}}{k_z\Delta z}\right. \\
& \left.+\psi_{Exy}|_{i+1/2,j,k}^{n}-\psi_{Exz}|_{i+1/2,j,k}^{n}-J_{sourcex}|_{i+1/2,j,k}^{n}\right\}
\end{aligned}
\tag{VI.9}
$$

où

$$
\begin{aligned}
\psi_{Exy}|_{i+1/2,j,k}^{n} &= b_y\psi_{Exy}|_{i+1/2,j,k}^{n-1}+c_y\left(\frac{H_z|_{i+1/2,j+1/2,k}^{n}-H_z|_{i+1/2,j-1/2,k}^{n}}{\Delta y}\right) \\
\psi_{Exz}|_{i+1/2,j,k}^{n} &= b_z\psi_{Exz}|_{i+1/2,j,k}^{n-1}+c_z\left(\frac{H_y|_{i+1/2,j,k+1/2}^{n}-H_y|_{i+1/2,j,k-1/2}^{n}}{\Delta z}\right) \\
b_w &= e^{-\left(\frac{\sigma_w}{k_w\varepsilon_0}+\frac{\alpha_w}{\varepsilon_0}\right)\Delta t} \\
c_w &= \frac{\sigma_w}{\sigma_w k_w+k_w^2\alpha_w}\left(e^{-\left(\frac{\sigma_w}{k_w\varepsilon_0}+\frac{\alpha_w}{\varepsilon_0}\right)\Delta t}-1.0\right)
\end{aligned}
\tag{VI.10}
$$

Notez que les coefficients discrets b_y et c_y ne sont non nuls que dans les régions PML avec une frontière de normale y. Les autres composantes peuvent être obtenues selon cette méthode.

Matériaux Dispersives

La méthode FDTD était à l'origine prévue pour une permittivité constante ne dépendant pas de la fréquence, de même que la perméabilité et la conductivité. Cependant, pour de nombreux matériaux, ce n'est pas réaliste. Les paramètres ci-dessus varient en fonction de la fréquence. Par la suite, les lois d'analyse de dispersion sont apparues.

Les méthodes de dispersion de matériaux génériques comprennent la méthode de la convolution récursive (RC) [88; 89], la convolution récursive linéaire par morceaux (PLRC) [90], la méthode de la transforée en Z [91], la convolution récursive trapézoïdale méthode [92] et la méthode de l'équation différentielle auxiliaire (ADE) [93], toutes ces méthodes sont présentées pour faire face à l'intégrale de convolution des équations de

Maxwell dans le domaine temporel. Pour une description des matériaux de dispersion, les modèles classiques sont utilisés : le modèle de Drude [70], le modèle de Lorentz [89], le modèle des points critiques [94] et toute combinaison de ces modèles [133; 95].

Dans notre travail, pour décrire les propriétés de dispersion des nano-particules en or, la combinaison de Drude et des points critiques(CP) modèle est utilisée avec l'algorithme FDTD par la méthode de la convolution récursive.

$$\varepsilon_{DCP}(\omega) = \varepsilon_\infty - \frac{\omega_D^2}{\omega^2 + i\gamma\omega} + \sum_m A_m \Omega_m \left(\frac{e^{i\phi_m}}{\Omega_m - \omega - i\Gamma_m} + \frac{e^{-i\phi_m}}{\Omega_m + \omega + i\Gamma_m}\right) \quad \text{(VI.11)}$$

où ε_∞ est la permittivité relative pour une fréquence infinie, ω_D est la fréquence plasma, γ est l'inverse du temps de relaxation. Ω_m est la fréquence de la paire de pôles m (fréquence de résonance non amortie du milieu). Γ_m est le coefficient d'amortissement. A_m est une constante. ϕ_m est une phase.

L'équation de mise à jour pour $\overrightarrow{E}$ peut finalement s'écrire :

$$\begin{aligned}\overrightarrow{E}|^{n+1} =& \frac{\varepsilon_\infty}{\varepsilon_\infty + \chi^0 + \frac{\sigma\Delta t}{\varepsilon_0}} \overrightarrow{E}|^n + \frac{\Delta t}{\varepsilon_0(\varepsilon_\infty + \chi^0 + \frac{\sigma\Delta t}{\varepsilon_0})} \overrightarrow{\nabla} \times \overrightarrow{H}|^{n+1/2} \\ &+ \frac{1}{\varepsilon_\infty + \chi^0 + \frac{\sigma\Delta t}{\varepsilon_0}} (\overrightarrow{\psi}_D|^n + R \sum_m \hat{\overrightarrow{\psi}}_m|^n)\end{aligned} \quad \text{(VI.12)}$$

Selon le matériau à étudier et la gamme de longueurs d'onde d'intérêt , le modèle et le nombre de termes pourront être choisis arbitrairement .

La condition importante à noter dans le but de s'assurer de la convergence de l'algorithme FDTD est

$$\left|\frac{\varepsilon_\infty}{\varepsilon_\infty + \chi^0 + \frac{\sigma\Delta t}{\varepsilon_0}}\right| < 1 \quad \text{(VI.13)}$$

L'équation de Yee pour $\vec{H}$ restera inchangée pour les médias non-magnétiques.

Algorithme FDTD pour les matériaux anisotropes

Jusqu'à présent, nous avons étudié l'algorithme FDTD original et les modifications pour les matériaux dispersifs. Dans cette partie, nous présenterons l'algorithme FDTD que nous avons utilisé pour des matériaux anisotropes.

Nous considérons des cristaux liquides nématiques comme des matériaux non-magnétiques, les propriétés anisotropes peuvent être décrites parle tenseur permittivité $\widetilde{\varepsilon}$. Les relations constitutives peuvent être écrites comme

$$\begin{aligned} \overrightarrow{B} &= \mu_0 \overrightarrow{H} \\ \overrightarrow{D} &= \widetilde{\varepsilon} \overrightarrow{E} \end{aligned} \tag{VI.14}$$

où $\widetilde{\varepsilon}$ est le tenseur de permittivité , qui peut être écrit comme suit

$$\widetilde{\varepsilon} = \begin{bmatrix} \varepsilon_{xx} & \varepsilon_{xy} & \varepsilon_{xz} \\ \varepsilon_{yx} & \varepsilon_{yy} & \varepsilon_{yz} \\ \varepsilon_{zx} & \varepsilon_{zy} & \varepsilon_{zz} \end{bmatrix} \tag{VI.15}$$

Il est commode d'introduire l'inverse du tenseur de permittivité que $\widetilde{\zeta} = \widetilde{\varepsilon}^{-1}$.

Dans ce cas, les équations de Maxwell en rotationnel, en l'absence de charges (ρ= 0) et de courant ($\overrightarrow{J} = 0$) et dans les matériaux anisotropes non-conducteurs, peut être écrite comme [96]

$$\begin{aligned} \bigtriangledown \times \overrightarrow{E} &= -\mu_0 \frac{\partial \overrightarrow{H}}{\partial t} \\ \widetilde{\zeta} \bigtriangledown \times \overrightarrow{H} &= \frac{\partial \overrightarrow{E}}{\partial t} \end{aligned} \tag{VI.16}$$

En utilisant l'algorithme FDTD et compte tenu des conditions aux limites absorbantes pour les matériaux non magnétiques et non-conducteur, σ^* est égal à zéro ainsi que σ.

Ensuite, la composante suivant x du champ électrique E aux points ($i\Delta x$, $j\Delta y$,

$k\Delta z$) et au temps $t = (n + 1/2)\Delta t$ peut être écrite comme suit :

$$
\begin{aligned}
E_x|^{n+1}_{i+1/2,j,k} = {} & E_x|^{n}_{i+1/2,j,k} \\
& + dt\zeta_{xx}\Big(\frac{H_z|^{n+1/2}_{i+1/2,j+1/2,k} - H_z|^{n+1/2}_{i+1/2,j-1/2,k}}{k_y dy} - \frac{H_y|^{n+1/2}_{i+1/2,j,k+1/2} - H_y|^{n+1/2}_{i+1/2,j,k-1/2}}{k_z dz} \\
& + \psi_{E_{xxy}|^{n}_{i+1/2,j,k}} - \psi_{E_{xxz}|^{n}_{i+1/2,j,k}}\Big) \\
& + dt\zeta_{xy}\Big(\frac{H_x|^{n+1/2}_{i+1/2,j,k+1/2} - H_x|^{n+1/2}_{i+1/2,j,k-1/2}}{k_z dz} - \frac{H_z|^{n+1/2}_{i+1,j,k} - H_z|^{n+1/2}_{i,j,k}}{k_x dx} \\
& + \psi_{E_{xyz}|^{n}_{i+1/2,j,k}} - \psi_{E_{xyx}|^{n}_{i+1/2,j,k}}\Big) \\
& + dt\zeta_{xz}\Big(\frac{H_y|^{n+1/2}_{i+1,j,k} - H_y|^{n+1/2}_{i,j,k}}{k_x dx} - \frac{H_x|^{n+1/2}_{i+1/2,j+1/2,k} - H_x|^{n+1/2}_{i+1/2,j-1/2,k}}{k_y dy} \\
& + \psi_{E_{xzx}|^{n}_{i+1/2,j,k}} - \psi_{E_{xzy}|^{n}_{i+1/2,j,k}}\Big)
\end{aligned}
\tag{VI.17}
$$

où

$$
\begin{aligned}
\psi_{E_{xxy}}|^{n}_{i+1/2,j,k} &= b_{y|i+1/2,j,k}\psi_{E_{xxy}}|^{n-1}_{i+1/2,j,k} + c_{y|i+1/2,j,k}\Big(\frac{H_z|^{n+1/2}_{i+1/2,j+1/2,k} - H_z|^{n+1/2}_{i+1/2,j-1/2,k}}{dy}\Big) \\
\psi_{E_{xxz}}|^{n}_{i+1/2,j,k} &= b_{z|i+1/2,j,k}\psi_{E_{xxz}}|^{n-1}_{i+1/2,j,k} + c_{z|i+1/2,j,k}\Big(\frac{H_y|^{n+1/2}_{i+1/2,j,k+1/2} - H_y|^{n+1/2}_{i+1/2,j,k-1/2}}{dz}\Big) \\
\psi_{E_{xyz}}|^{n}_{i+1/2,j,k} &= b_{z|i+1/2,j,k}\psi_{E_{xyz}}|^{n-1}_{i+1/2,j,k} + c_{z|i+1/2,j,k}\Big(\frac{H_x|^{n+1/2}_{i+1/2,j,k+1/2} - H_x|^{n+1/2}_{i+1/2,j,k-1/2}}{dz}\Big) \\
\psi_{E_{xyx}}|^{n}_{i+1/2,j,k} &= b_{x|i+1/2,j,k}\psi_{E_{xyx}}|^{n-1}_{i+1/2,j,k} + c_{x|i+1/2,j,k}\Big(\frac{H_z|^{n+1/2}_{i+1,j,k} - H_z|^{n+1/2}_{i,j,k}}{dx}\Big) \\
\psi_{E_{xzx}}|^{n}_{i+1/2,j,k} &= b_{x|i+1/2,j,k}\psi_{E_{xzx}}|^{n-1}_{i+1/2,j,k} + c_{x|i+1/2,j,k}\Big(\frac{H_y|^{n+1/2}_{i+1,j,k} - H_y|^{n+1/2}_{i,j,k}}{dx}\Big) \\
\psi_{E_{xzy}}|^{n}_{i+1/2,j,k} &= b_{z|i+1/2,j,k}\psi_{E_{xzy}}|^{n-1}_{i+1/2,j,k} + c_{z|i+1/2,j,k}\Big(\frac{H_x|^{n+1/2}_{i+1/2,j+1/2,k} - H_x|^{n+1/2}_{i+1/2,j-1/2,k}}{dy}\Big)
\end{aligned}
\tag{VI.18}
$$

Ici, b_w et c_w, avec $w = x, y, z$ suit la définition de l'équation Eq. VI.10. Ils sont non-nuls que dans les régions PML.

Dans les équations VI.17 et VI.18, seuls les éléments en $i + 1/2$ sont réellement présents dans la grille de Yee (voir Fig. VI.1), mais peuvent être approximés, comme $H_x|^{n+1/2}_{i+1/2,j,k+1/2} = \dfrac{H_x|^{n+1/2}_{i+1,j,k+1/2} + H_x|^{n+1/2}_{i,j,k+1/2}}{2}$, par exemple.

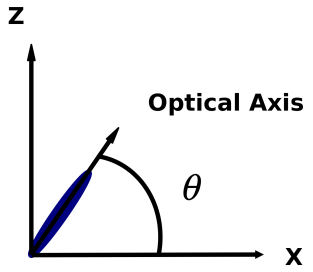

Fig. VI.2 – Orientation des molécules de cristaux liquides

Les autres éléments sont donnés par

$$
\begin{aligned}
H_x|^{n+1/2}_{i+1/2,j,k+1/2} &= \frac{1}{4}(H_x|^{n+1/2}_{i+1,j+1/2,k+1/2} + H_x|^{n+1/2}_{i+1,j-1/2,k+1/2} + H_x|^{n+1/2}_{i,j+1/2,k+1/2} + H_x|^{n+1/2}_{i,j-1/2,k+1/2}) \\
H_x|^{n+1/2}_{i+1/2,j,k-1/2} &= \frac{1}{4}(H_x|^{n+1/2}_{i+1,j+1/2,k-1/2} + H_x|^{n+1/2}_{i+1,j-1/2,k-1/2} + H_x|^{n+1/2}_{i,j+1/2,k-1/2} + H_x|^{n+1/2}_{i,j-1/2,k-1/2}) \\
H_z|^{n+1/2}_{i+1,j,k} &= \frac{1}{4}(H_z|^{n+1/2}_{i+3/2,j+1/2,k} + H_z|^{n+1/2}_{i+3/2,j-1/2,k} + H_z|^{n+1/2}_{i+1/2,j+1/2,k} + H_z|^{n+1/2}_{i+1/2,j-1/2,k}) \\
H_z|^{n+1/2}_{i,j,k} &= \frac{1}{4}(H_x|^{n+1/2}_{i+1/2,j+1/2,k} + H_z|^{n+1/2}_{i+1/2,j-1/2,k} + H_z|^{n+1/2}_{i-1/2,j+1/2,k} + H_z|^{n+1/2}_{i-1/2,j-1/2,k}) \\
H_y|^{n+1/2}_{i+1,j,k} &= \frac{1}{4}(H_y|^{n+1/2}_{i+3/2,j,k+1/2} + H_y|^{n+1/2}_{i+3/2,j,k-1/2} + H_y|^{n+1/2}_{i+1/2,j,k+1/2} + H_y|^{n+1/2}_{i+1/2,j,k-1/2}) \\
H_y|^{n+1/2}_{i,j,k} &= \frac{1}{4}(H_y|^{n+1/2}_{i+1/2,j,k+1/2} + H_y|^{n+1/2}_{i+1/2,j,k-1/2} + H_y|^{n+1/2}_{i-1/2,j,k+1/2} + H_y|^{n+1/2}_{i-1/2,j,k-1/2}) \\
H_x|^{n+1/2}_{i+1/2,j+1/2,k} &= \frac{1}{4}(H_x|^{n+1/2}_{i+1,j+1/2,k+1/2} + H_x|^{n+1/2}_{i+1,j+1/2,k-1/2} + H_x|^{n+1/2}_{i,j+1/2,k+1/2} + H_x|^{n+1/2}_{i,j+1/2,k-1/2}) \\
H_x|^{n+1/2}_{i+1/2,j-1/2,k} &= \frac{1}{4}(H_x|^{n+1/2}_{i+1,j-1/2,k+1/2} + H_x|^{n+1/2}_{i+1,j-1/2,k-1/2} + H_x|^{n+1/2}_{i,j-1/2,k+1/2} + H_x|^{n+1/2}_{i,j-1/2,k-1/2})
\end{aligned}
\tag{VI.19}
$$

De même, les composantes E_y, E_z, H_x, H_y et H_z peuvent être décrites aussi.

Algorithme FDTD dans mon code

Dans le cas particulier d'un axe optique des molécules de cristaux liquides nématiques dans le plan xz, on définit θ comme l'angle entre l'axe optique et la coordonnée x. La Fig. VI.2 décrit l'orientation des molécules de cristaux liquides.

Les éléments du tenseur de permittivité sont donnés par l'équation VI.20

$$\begin{aligned}
\varepsilon_{xx} &= \varepsilon_o(n_o^2 \sin^2\theta + n_e^2 \cos^2\theta) \\
\varepsilon_{yy} &= \varepsilon_o n_o^2 \\
\varepsilon_{zz} &= \varepsilon_o(n_o^2 \cos^2\theta + n_e^2 \sin^2\theta) \\
\varepsilon_{xz} &= \varepsilon_{zx} = \varepsilon_o(n_o^2 - n_e^2)\sin\theta\cos\theta \\
\varepsilon_{xy} &= \varepsilon_{yx} = \varepsilon_{yz} = \varepsilon_{zy} = 0
\end{aligned} \tag{VI.20}$$

En réponse, l'inverse du tenseur de permittivité

$$\begin{aligned}
\zeta_{xx} &= \frac{n_o^2 \cos^2\theta + n_e^2 \sin^2\theta}{\varepsilon_0 n_o^2 n_e^2} \\
\zeta_{yy} &= \frac{1}{\varepsilon_0 n_o^2} \\
\zeta_{zz} &= \frac{n_o^2 \sin^2\theta + n_e^2 \cos^2\theta}{\varepsilon_0 n_o^2 n_e^2} \\
\zeta_{xz} &= \zeta_{zx} = -\frac{(n_o^2 - n_e^2)\sin\theta\cos\theta}{\varepsilon_0 n_o^2 n_e^2} \\
\zeta_{xy} &= \zeta_{yx} = \zeta_{yz} = \zeta_{zy} = 0
\end{aligned} \tag{VI.21}$$

La combinaison des propriétés dispersives des nano-particules et anisotrope des LCs donne pour l'algorithme FDTD et pour la composante x du champ électrique

$$\begin{aligned}
E_x|_{i+1/2,j,k}^{n+1} &= C_1 E_x|_{i+1/2,j,k}^{n} \\
&+ C_2\Big(\frac{H_z|_{i+1/2,j+1/2,k}^{n+1/2} - H_z|_{i+1/2,j-1/2,k}^{n+1/2}}{k_y dy} - \frac{H_y|_{i+1/2,j,k+1/2}^{n+1/2} - H_y|_{i+1/2,j,k-1/2}^{n+1/2}}{k_z dz} \\
&+ \psi_{E_{xxy}|_{i+1/2,j,k}^{n}} - \psi_{E_{xxz}|_{i+1/2,j,k}^{n}}\Big) + C_3 \Psi|^n \\
&+ dt\zeta_{xy}\Big(\frac{H_x|_{i+1/2,j,k+1/2}^{n+1/2} - H_x|_{i+1/2,j,k-1/2}^{n+1/2}}{k_z dz} - \frac{H_z|_{i+1,j,k}^{n+1/2} - H_z|_{i,j,k}^{n+1/2}}{k_x dx} \\
&+ \psi_{E_{xyz}|_{i+1/2,j,k}^{n}} - \psi_{E_{xyx}|_{i+1/2,j,k}^{n}}\Big) \\
&+ dt\zeta_{xz}\Big(\frac{H_y|_{i+1,j,k}^{n+1/2} - H_y|_{i,j,k}^{n+1/2}}{k_x dx} - \frac{H_x|_{i+1/2,j+1/2,k}^{n+1/2} - H_x|_{i+1/2,j-1/2,k}^{n+1/2}}{k_y dy} \\
&+ \psi_{E_{xzx}|_{i+1/2,j,k}^{n}} - \psi_{E_{xzy}|_{i+1/2,j,k}^{n}}\Big)
\end{aligned} \tag{VI.22}$$

où les coefficients C_1, C_2, C_3 dépendent des matériaux.

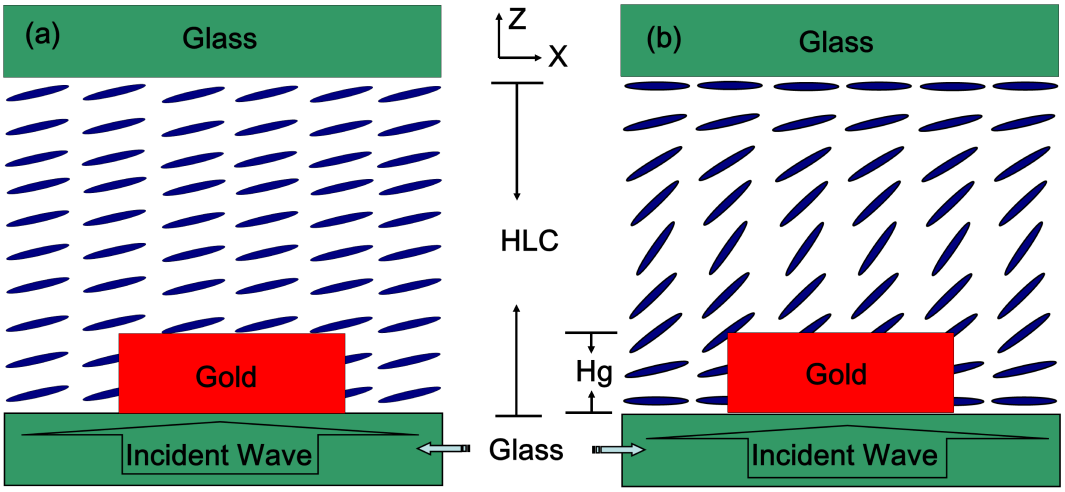

Fig. VI.3 – Schéma de l'étude : nanostructures d'or dans la cellule LC, prise en sandwich entre deux couches de silice. Ancrage faible (à gauche) et ancrage forg (à droite)

Ici, l'équation VI.18 et l'équation Eq. VI.19 sont appropriées pour ce cas également. La description numérique pour d'autres éléments électromagnétiques peut être obtenue de façon similaire par cette méthode.

VI.3 Résultats et analyse

Les positions des réonances plasmon localisées (LSPR pour Localized Surface Plasmon Resonance) et du gain Raman (G_{SERS}) d'un ensemble ordonné de nanocylindres en or, entouré de cristal liquide nématique (LC), sont étudiées à l'aide de la méthode FDTD. Les structures sont conçues de sorte que l' accordabilité maximale de LSPR est atteint. Deux résonances se produisent pour certaines structures. L'influence des effets d'ancrage, entre les molécules de cristaux liquides nématiques et les substrats de verre, sur le décalage de longueurs d'onde de résonance, ainsi que le gain Raman sont étudiées et les résultats sont comparés avec le cas d'un alignement parfait des molécules de cristal liquide et un matériau isotrope.

Un schéma de la configuration est représentée sur la Fig. VI.3.

Les positions des résonances sont trouvées théoriquement grâce au calcul des spectres d'extinction. Les propriétés d'anisotropie du LC sont incluses dans le code FDTD en utilisant un procédé qui a été présenté dans la partie précédente .

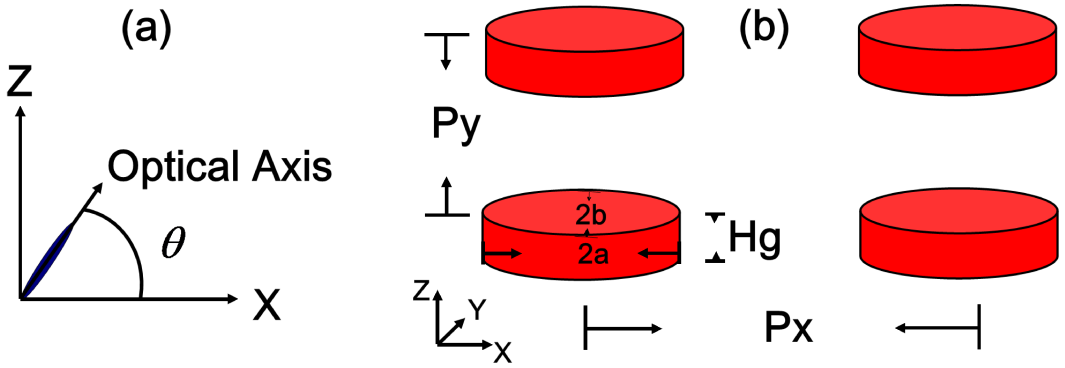

Fig. VI.4 – (a) Orientation de l'axe optique de la molécule LC, (b) Tableau de paramètres.

Les discrétisations spatiales et temporelle sont choisies comme $\Delta x = \Delta y = \Delta z = 2\,\text{nm}$, et $\Delta t = \Delta z/(2c)$ avec c la vitesse de la lumière dans le vide. La lumière incidente se propage à partir du bas de la structure, avec une polarisation linéaire le long de l'axe x.

Dans les simulations, nous supposons que l'axe optique des LC tourne autour de l'axe y dans le plan xz, et θ est défini comme l'angle entre l'axe optique et l'axe x (Fig. VI.4) (a).

Le calcul de l'orientation de la molécule LC est obtenu par la minimisation de énergie libre sous l'influence d'un champ électrique statique externe, et l'alignement des molécules de cristaux liquides sur le substrat dépend de l'énergie d'ancrage .

Les molécules de cristaux liquides, au milieu de la cellule, réagissent fortement au champ extérieur pour la raison qu'ils sont loin du substrat de verre, de sorte que le couple d'ancrage les affecte moins. L'angle incliné au maximum apparaÎt au milieu de la couche LC et est défini comme θ_{max}. Par conséquent, afin de décrire la variation de l'orientation de l'axe optique des molécules de cristaux liquides suivant la direction z, nous allons utiliser la fonction [32] :

$$\theta(z) = \theta_{max} \sin(\frac{\pi}{H_{LC}} z), \tag{VI.23}$$

où H_{LC} est l'épaisseur LC .

L'angle θ_{max} peut être variée en changeant le champ électrique externe . Les indices de réfraction ordinaire et extraordinaire sont respectivement $n_o = 1.53$ et $n_e = 1.74$ [128].

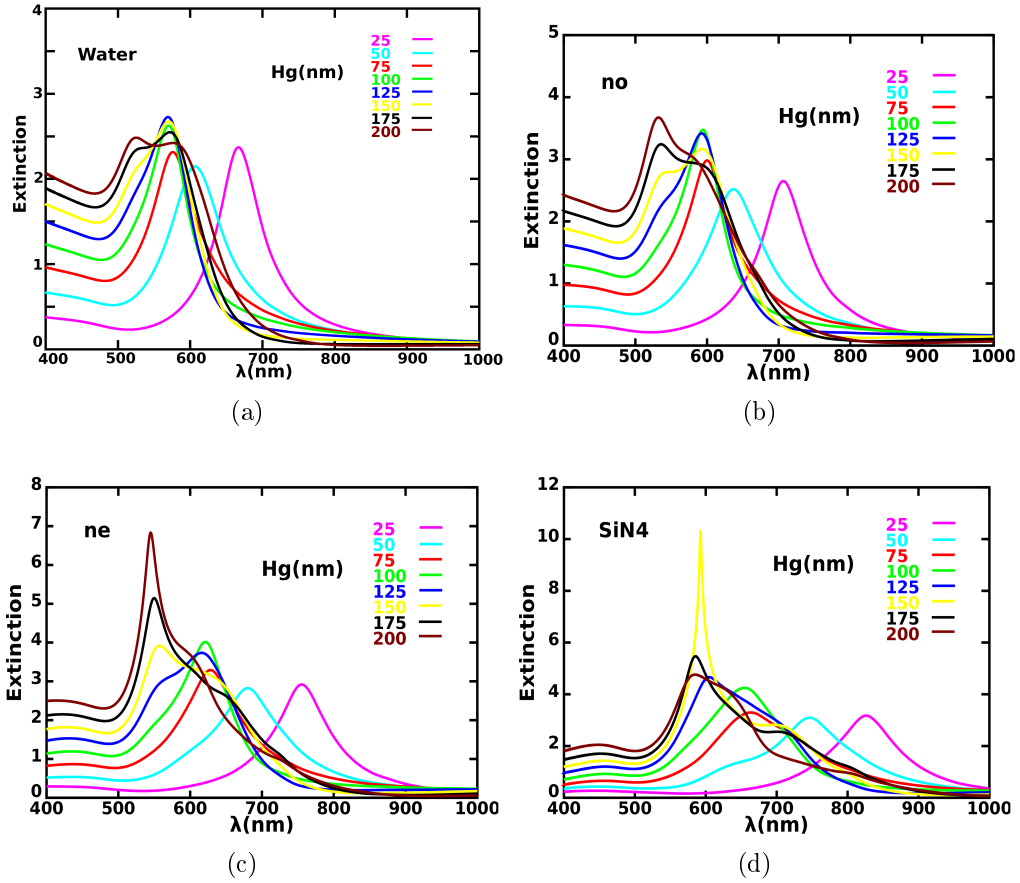

Fig. VI.5 – Spectres d'extinction pour différents matériaux isotropes environnants.

Les epectres d'extinction, en utilisant les nano-cylindres avec base circulaire, sont décrits en fonction de la longueur d'onde sur la figure Fig. VI.5(a) pour l'eau (index n=1.333), sur la Fig. VI.5(b), n_o (indice n = 1,53), sur la Fig. VI.5(c) pour n_e (indice n = 1,74) et sur la figure VI.5(d) pour SiN4 (indice n = 2,01). Le diamètre est de $2a = 2b = 100nm$, voir le schéma de la Fig. VI.4. Les périodes sont de $P_x = P_y = 200nm$, la hauteur d'or varie de $25nm$ à $200nm$.

Les spectres montres un décalage de la résonance vers le bleu avec l' augmentation de la hauteur des nano-particules [134]. Parfois, le pic de résonance est dédoublé par exemple sur la Fig. VI.5(d). Ces doubles résonances doubles seront expliquées plus tard.

Afin d'obtenir un décalage de LSPR sans faire varier la hauteur de l'or ou changer les matériaux environnants les nanoparticules d'or, un matériau anisotrope peut être utilisé.

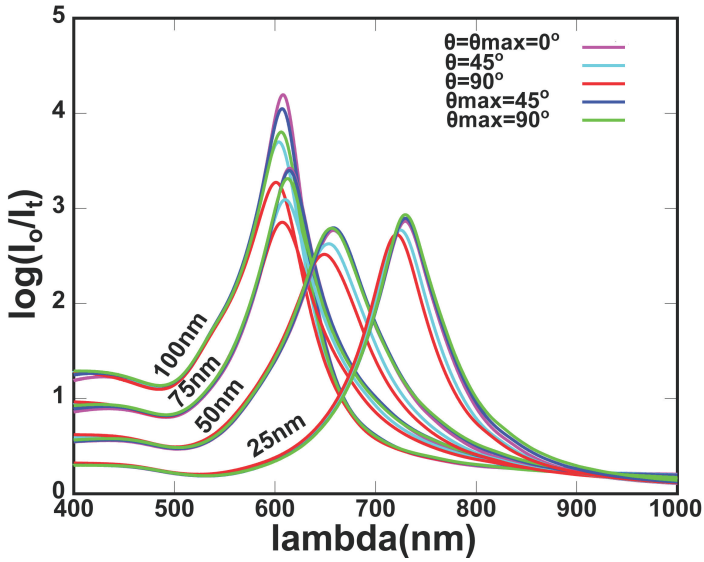

Fig. VI.6 – Spectres d'extinction en fonction de θ et θ_{max} pour différentes hauteurs de structures d'or.

Dans la première série de calculs , les nano-particules métalliques sont des cylindres d'or avec base circulaire (see Fig. VI.3), Le diamètre est $2a = 2b = 100\,\text{nm}$, les périodes du réseau sont $P_x = P_y 200\,\text{nm}$, et l'épaisseur de la couche LC est de H_{LC} =200 nm. Pour comprendre facilement, ici , nous nous concentrons uniquement sur des nano-particules avec des hauteurs variant de 25 nm à 100 nm. Les spectres d'extinction sont décrites sur la figure VI.6 en fonction de l'orientation des molécules de cristaux liquides.

L'influence de l'ancrage des molécules de cristaux liquides sur la position des résonances peut être observée sur la Fig. VI.6, les spectres d' extinction sont en fonction de θ (LCs avec un alignement parfait) et θ_{max} (LC avec ancraget) pour différentes hauteurs $(25\,\text{nm} - 100\,\text{nm})$.

Le principal changement est dû à la modification de la hauteur qui induit un décalage vers le bleu [134], quelle que soit l'orientation des molécules de cristaux liquides, comme il est souligné sur la figure VI.7(a).

La variation de la LSPR pour une hauteur fixe est mieux visible sur la Fig. VI.7(b), avec $H_g = 50\,\text{nm}$.

La courbe bleue décrit la LSPR pour θ constant et correspond au comportement décrit précédemment [128]. La courbe rouge montre le décalage de la résonance en fonction de θ_{max}, c'est à dire avec des effets d'ancrage pris en compte. Il est clair ici

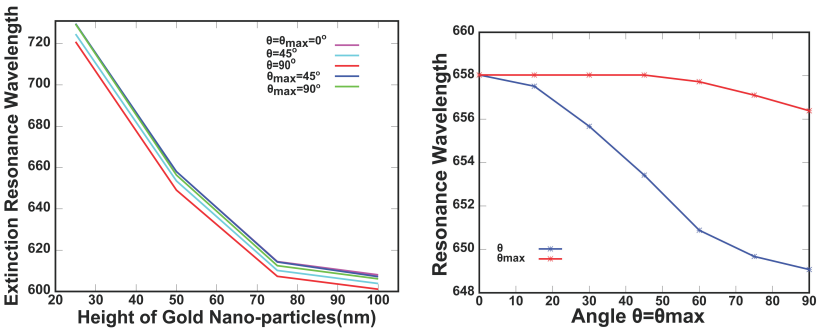

(a) (b)

Fig. VI.7 – (a) Changement de LSPR en fonction de la hauteur des structures d'or pour différentes orientations de LC. (b) Décalage LSPR en fonction de θ (courbe bleue) ou θ_{Max} (ligne rouge) pour $H_g = 50\,\text{nm}$.

Tab. VI.1 – Or nano-tubes avec base circulaire. $2a = 2b = 100\,\text{nm}$, $P_x = P_y = 200\,\text{nm}$.

H_g (nm)	25	50	75	100
λ_0(nm)	729.7	657.8	614.6	607.9
$\Delta\lambda_\theta$(nm)	8.53	8.96	7.11	6.97
$\Delta\lambda_{\theta_{max}}$(nm)	0	1.65	1.97	1.93

que la capacité de réglage de la résonance est fortement affectée.

Ainsi, nous pouvons conclure que la sensibilité $S = \dfrac{d\lambda}{dn}$ [130] sera également fortement réduite.

Nous pouvons vérifier comment la sensibilité dépend de la hauteur de cylindres d'or pour $H_g = 25\,\text{nm}$, $50\,\text{nm}$, $75\,\text{nm}$, $100\,\text{nm}$. Tous les autres paramètres sont les mêmes que dans la première série de calculs.

Les déplacements calculés $\Delta\lambda_\theta$ et and $\Delta\lambda_{\theta_{max}}$ sont donnés dans le tableau Tab. VI.1. Sans l'effet d'ancrage, la plus haute valeur de $\Delta\lambda_\theta$ est atteinte pour 50 nm. D'autre part, pour $\Delta\lambda_{\theta_{max}}$ la valeur maximale est atteinte for 75 nm, mais la fonction de la hauteur de la structure est très faible. Pour la plus petite hauteur $H_g = 25\,\text{nm}$, aucun changement de la position de résonance n'a pu être observée. Cela peut s'expliquer par le fait que le sommet de la structure se trouve dans une position où la rotation des molécules de cristaux liquides est vraiment faible, alors qu'il est légèrement plus grand pour d'autres hauteurs. Néanmoins, les variations calculées sont toutes très petites. Le plus grand changement $\Delta\lambda_{\theta_{max}}$ apparaît à H_g= 75 nm.

Pour améliorer la capacité de réglage de LSPR, la modification de la période dans la direction P_x du 150 nm à 300 nm avec l'intervalle de $50nm$ sont simulées. Les autres paramètres sont les mêmes que ceux ci-dessus.

En comparant les résultats avec P_x modifiés, le décalage de LSPR est amélioré autour de $\Delta\lambda_{\theta_{max}} = 6$ nm quand H_g= 75 nm , $2a = 2b = 100$ nm, $P_y = 200$ nm et P_x = 150 nm, ce qui semble faible, bien que trois fois plus élevé que le résultat dans le tableau Tab. VI.1.

Par la suite, les simulations sont effectuées avec la variation non seulement des périodes, mais aussi de la taille des particules métalliques.

En fait, ces études ont montré que la position de la résonance LSPR peut être modifiée à travers un large spectre en faisant varier la taille de la nanoparticule métallique [135; 136].

Comme il a déjà été suggéré précédemment, la position de la partie supérieure de la structure de l'or a une influence sur les possibilités de changement de LSPR. Par conséquent, dans ce qui suit, nous allons utiliser les mêmes structures que ci-dessus à l'exception de la hauteur LC $H_{LC} = 2H_g$, ce qui implique que la partie supérieure de la structure sera toujours à la position de la rotation maximale de la axe LC. Les résultats seront comparés à $H_{LC} = 200$ nm.

Par une étude systématique en utilisant différents paramètres de périodicité et de formes variées de nano- particules, un changement $\Delta\lambda_{\theta_{max}}$ jusqu'à 31 nm a été atteint, ce qui est environ 16 fois plus élevé que la valeur obtenue dans Tab. VI.1.

Lorsque la distance des nano-particules dans la direction x est égale à 25 nm, avec l'augmentation de l'axe principal de 175 nm et en utilisant $2b50$ nm, $P_x = P_y = 200$ nm, $H_g = 75$ nm quand $H_{LC} = 2H_g$, les calculs sont effectués et les résultats sont présentés dans la Tab. VI.2.

On voit que $\Delta\lambda_{\theta_{max}}$ et $\Delta\lambda_\theta$ sont toujours plus granse dans le cas $H_{LC} = 2H_g$ que dans le cas $H_{LC} = 200$ nm, ce qui confirme l'hypothèse que la position de la partie supérieure de nanoparticules par rapport à la rotation maximale des molécules de cristaux liquides a une influence sur le décalage de LSPR.

Tab. VI.2 – Nano-cylindres à base elliptique. $2a = 175\,\text{nm}$, $2b = 50\,\text{nm}$, $P_x = P_y = 200\,\text{nm}$.

H_g (nm)		25	50	75	100
H_{LC}=200nm	λ_0(nm)	1251.28	1119.08	1030.04	893.55
	$\Delta\lambda_\theta$(nm)	32.72	45.82	47.31	33.35
	$\Delta\lambda_{\theta_{max}}$(nm)	1.49	13.57	24.69	13.50
$H_{LC} = 2H_g$	λ_0(nm)	1248.31	1118.48	1030.54	893.55
	$\Delta\lambda_\theta$(nm)	36.08	45.77	48.27	33.35
	$\Delta\lambda_{\theta_{max}}$(nm)	21.18	27.92	30.95	13.50

La position de pic de résonance λ_0 ne dépend que faiblement sur H_{LC}, alors $\Delta\lambda_{\theta_{max}}$ est plus fortement modifié.

En conclusion, nous avons étudié l'évolution de la résonance plasmon de nanostructures d'or dans une cellule LC en fonction de l'orientation de l'axe optique des molécules de cristaux liquides en prenant en compte les effets d'ancrage. Nous avons montré que ces effets réduisent fortement la capacité de réglage de LSPR, mais que des modifications de la forme des nanostructures ou la hauteur LC pourraient efficacement compenser cela.

Résonances doubles

Dans cette partie, nous étudions les résonances doubles.

Les nano-particules que nous avons étudiés sont des cylindres d'or avec base elliptique, avec grand axe $2a = 125\,\text{nm}$ (parallèle à l'axe x), petit axe $2b = 50\,\text{nm}$ (parallèle à l'axe y), et la hauteur $H_g = 200\,\text{nm}$. Les périodicités des nano-particules métalliques (distance centre au centre) sont $P_x = P_y = 200\,\text{nm}$. L'espace libre entre les particules est rempli d'un cristal liquide nématique.

Les positions des résonance sont déterminées par le calcul de spectres d'extinction. Nous considérons d'abord un milieu isotrope. L'indice de réfraction de ce milieu varie de $n = 1,53$ à $n = 1,74$, qui est entre les valeurs définies précédemment n_o=1,53 et n_e=1,74. Les résultats sont décrits sur la Fig. VI.8(a). Une caractéristique de double résonance peut être observée dans les spectres. Lorsque $n = 1,60$, la résonance gauche est plus forte que les autres, ce qui peut être liés au fait que la partie imaginaire de la permittivité de l'oratteint sa valeur la plus faible.

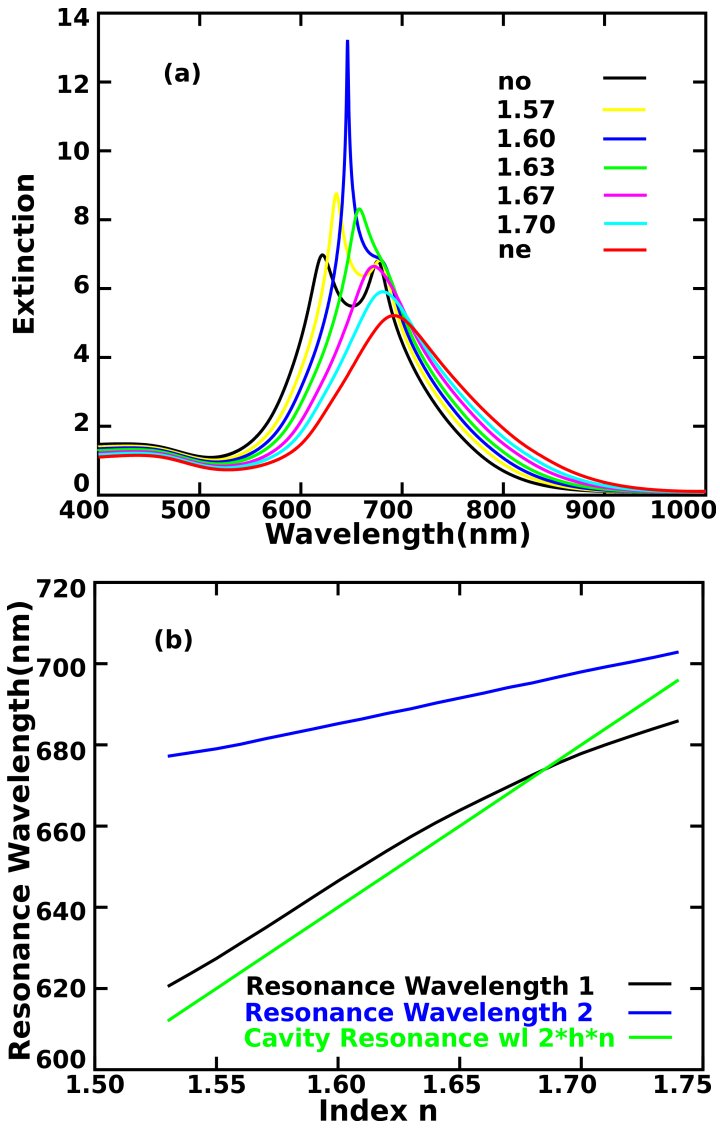

Fig. VI.8 – Spectres d'extinction et positions des résonance en fonction de l'indice. (a) environnement isotrope, indice variant de $n_o = 1.53$ à $n_e = 1.74$, (b) positions des résonances.

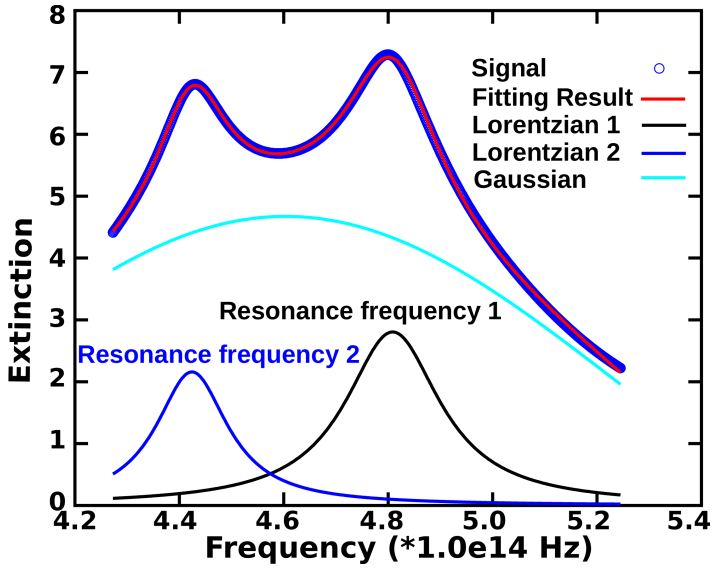

Fig. VI.9 – Description des spectres d'extinction en fonction de la fréquence, n = 1,54.

Afin d'étudier le déplacement des deux résonances, nous ajustons les spectres en utilisant une combinaison de deux lorentzienne et une gaussienne, cette dernière étant utilisée pour la description du signal de base :

$$s(\omega) = a_0 + \frac{a_1}{1 + (\frac{\omega - \omega_1}{c_1})^2} + \frac{a_2}{1 + (\frac{\omega - \omega_2}{c_2})^2} + a_3.e^{-\frac{(\omega - \omega_3)^2}{c_3}}, \qquad \text{(VI.24)}$$

avec ω_1 et ω_2 les fréquences des deux résonances.

Un exemple est donné sur la Fig. VI.9 pour $n = 1.54$.

Les résultats pour les spectres de la Fig. VI.8(a) sont donnés sur la Fig. VI.8(b). La courbe noire de la Fig VI.8(b) peut être décrite en utilisant le mode de résonance de cavité (courbe verte), donné par $\frac{\lambda}{2} = h.n$ [145], et la courbe bleue correspondes à la résonance plasmon. Afin d'étudier les spectres d'extinction des nano-particules dans la cellule LC, deux séries de simulations sont effectuées.

Tout d'abord, on considère des molécules de cristaux liquides parfaitement alignées autour de nano-particules d'or. Les spectres d'extinction sont tracés en fonction de l'angle θ sur la Fig. VI.10(a), les résonances sont décrites par des traits pleins sur la Fig. VI.10(c), en fonction de l'indice dans la direction$x$: $n = \frac{n_o n_e}{\sqrt{n_e^2 \sin^2\theta + n_o^2 \cos^2\theta}}$. Ils sont très proches de ceux obtenus en utilisant des matériaux isotropes comme matériaux environnants décrits sur la Fig. VI.8(b).

Avec l'effet d'ancrage pris en compte, les spectres sont décrits pour différentes valeurs θ_{max} sur la Fig. VI.10(b) [139; 32].

Les positions des résonances sont décrites par des lignes pointillées sur la Fig VI.10(c).

En comparant les spectres d' extinction sur la Fig VI.8(a), Fig VI.10(a) et Fig VI.10(b), et les résultats ajustés, les nano-particules en présence de LCS (sans ancrage) se comportent optiquement comme les nano-particules dans un milieu isotrope [121]. Les deux résonances présentent un décalage vers le bleu en diminuant l'indice entourant lesnano-particules ou en diminuant l'indice dans la direction de polarisation incidente en changeant l'orientation des molécules de cristaux liquide [128; 130].

Si on tient compte des effets d'ancrage, l'indice de réfraction au centre de la structure est un peu plus petit que l'indice à proximité du substrat en verre. Dans ce cas, les deux pics de résonance se déplacent dans deux directions opposées quand nous réglons l'orientation des molécules de cristaux liquides en utilisant un champ électrique externe. Tandis que le mode de cavité est faiblement affecté, la résonance plasmon présente un décalage vers le bleu inattendu alors que l'indice effectif est augmenté.

VI.4 Conclusion

Dans ce travail, nous avons étudié l'évolution des résonances de nano-structures en or dans une cellule LC en fonction de l'orientation de l' axe optique des molécules de cristaux liquides en prenant en compte les effets d'ancrage. Nous avons montré que ces effets réduisent fortement la capacité de réglage des résonances. L'accordabilité maximum vaut $\Delta\lambda_{\theta_{max}} = 71.68\,\text{nm}$ dans ce cas. Pour les LCs avec un alignement parfait, le décalage maximal est de $\Delta\lambda_{\theta} = 98\,\text{nm}$.

Des résonances doubles sont observées, et en changeant l'orientation des molécules de cristaux liquides(LCs), les deux positions de résonances peuvent être réglées. L'influence des effets d'ancrage entre les molécules de cristaux liquides nématiques et le substrat de verre sur l'accordabilité est étudiée.

Nous prévoyons que ce travail offrira une aide pour la conception et la fabrication de

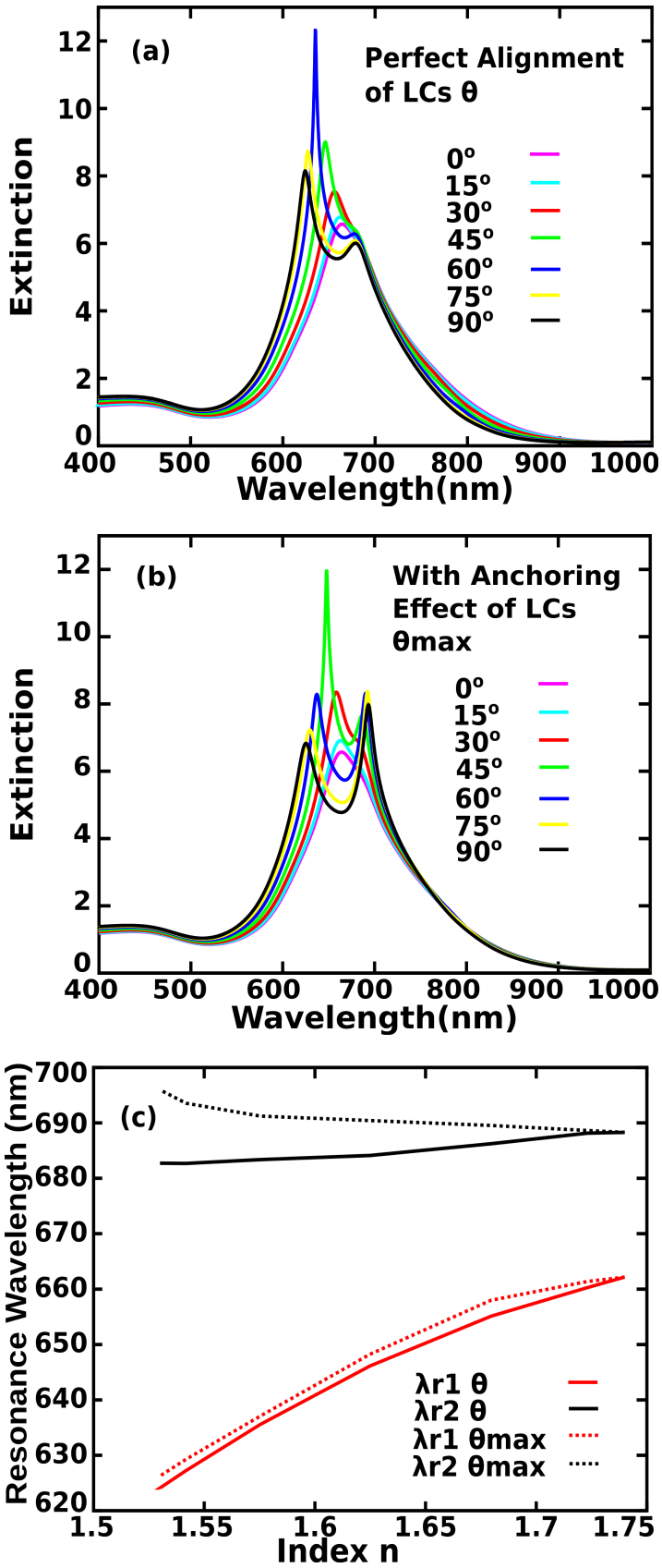

Fig. VI.10 – Spectre d' extinction des nano-particules entourées par des LCs (a) avec un alignement parfait et (b) avec les effets d'ancrage pris en compte. (c) Positions des résonances du spectre d'extinction : lignes solides pour LCs avec un alignement parfait, lignes pointillées pour LCs avec ancrage effets pris en compte.

substrats SERS. Néanmoins, d'autres travaux sont encore nécessaires pour optimiser au maximum la configuration afin d'obtenir une plus grande capacité de réglage des résonances.

BIBLIOGRAPHY

[1] E. Abbe. Beitr̆age zur theorie des mikroskops und der mikroskopischen wahrnehmung. *Archiv f. Miroskop. Anat.*, 9 :413, 1873.

[2] L. Rayleigh. Investigations in optics, with special reference to the spectroscope. *Phil. Mag.*, 8 :261–274/403–411/477–486, 1879.

[3] L. Novotny and B. Hecht. *Principles of Nano-Optics.* Cambridge, 2012.

[4] R. H. Ritchie. Plasma losses by fast electrons in thin films. *Phys. Rev.*, 106 :874–881, 1957.

[5] W. L. Barnes, A. Dereux, and T. W. Ebbesen. Surface plasmon subwavelength optics. *nature*, 424 :825, 2003.

[6] A. D. Boardman. *Electromagnetic Surface Modes.* John Wiley & Sons, New York, 1982.

[7] U. Kreibig and M. Vollmer. *Optical Properties of Metal Clusters.* Springer, Berlin, 1995.

[8] A. V. Zayats, I. I. Smolyaninov, and A. A. Maradudin. Nano-optics of surface plasmon polaritons. *Phys. Rep.*, 408 :131–314, 2005.

[9] Martin Moskovits. Surface-enhanced spectroscopy. *Rev. Mod. Phys.*, 57 :783–826, 1985.

[10] D. L. Jeanmaire and R. P. Van Duyne. Surface raman electrochemistry part i. heterocyclic, aromatic and aliphatic amines adsorbed on the anodized silver electrode. *J. Electroanal. Chem.*, 1 :84, 1977.

[11] S. Ushioda, Y. Uehara, and M. Kuwahara. STM light emission spectroscopy of Au film. *Appl. Surf. Sci.*, 60 :448–453, 1992.

[12] A. V. Zayats and V. Sandoghdar. Apertureless scanning near-field second-harmonic microscopy. *Opt. Commun.*, 178 :245–249, 2000.

[13] I. I. Smolyaninov, A. V. Zayats, and C. C. Davis. Near-field second harmonic generation from a rough metal surface. *Phys. Rev. B*, 56 :9290–9293, 1997.

[14] A. V. Zayats and I. I. Smolyaninov. Near-field photonics : surface plasmon polaritons and localized surface plasmons. *J. Opt. A : Pure Appl. Opt.*, 5 :S16, 2003.

[15] G. C. Schatz and R. P. Van Duyne. In handbook of vibrational spectroscopy. *Wiley, New York,*, 1 :759–774, 2002.

[16] A. D. McFarland and R. P. Van Duyne. Single silver nanoparticles as real-time optical sensors with zeptomole sensitivity. *Nano Lett.*, 3 :1057–1062, 2003.

[17] C. Noguez. Surface plasmons on metal nanoparticles :the influence of shape and physical environment. *J. Phys. Chem. C*, 111 :3806–3819, 2007.

[18] K. S. Lee and M. A. El-Sayed. Gold and silver nanoparticles in sensing and imaging : sensitivity of plasmon response to size, shape, and metal composition. *J. Phys. Chem. B*, 110 :19220–5, 2006.

[19] A. J. Haes, S. l. Zou, G. C. Schatz, and R. P. Van Duyne. Nanoscale optical biosensor Short range distance dependence of the localized surface plasmon resonance of noble metal nanoparticles. *J. Phys. Chem. B*, 108 :6961–6968, 2004.

[20] A. Y. G. Fuh, C. Y. Lin, M. S. Li, and H. C. Lin. Optical kerr constant of liquid crystals with gold-nanoparticle-doped alignment films. *J. Phys. D : Appl. Phys.*, 45 :445104, 2012.

[21] J. Xie, X. M. Zhang, Z. H. Peng, Z. H. Wang, T. Q. Wang, S. J. Zhu, Z. Y. Wang, L. Zhang, J. H. Zhang, and B. Yang. Low electric field intensity and thermotropic tuning surface plasmon band shift of gold island film by liquid crystals. *J. Phys. Chem. C*, 116 :2720–2727, 2012.

[22] D. Coursault, J. Grand, B. Zappone, H. Ayeb, G. Lévi, N. Félidj, and E. Lacaze. Linear self-assembly of nanoparticles within liquid crystal defect arrays. *Adv. Mater.*, 24 :1461–1465, 2012.

[23] S. Umadeviand, X. Feng, and T. Hegmann. Large area self-assembly of nematic liquid-crystal-functionalized gold nanorods. *Adv. Funct. Mater.*, 23 :1393–1403, 2013.

[24] S. Umadevi, X. Feng, and T. Hegmann. Bent-core and nematic liquid crystal functionalized gold nanorods, ferroelectrics. *Ferroelectrics*, 431 :164–175, 2012.

[25] G. M. Koenig, B. T. Gettelfinger, J. J. de Pablo, and N. L. Abbott. Using localized surface plasmon resonances to probe the nanoscopic origins of adsorbate-driven ordering transitions of liquid crystals in contact with chemically functionalized gold nanodots. *Nano Lett.*, 8 :2362–2368, 2008.

[26] I. Abdulhalim. Liquid crystal active nanophotonics and plasmonics : from science to devices. *J. Nanophotonics*, 6(1) :061001–1–061001–27, 2012.

[27] K. Yee. Numerical solution of initial boundary value problems involving maxwell's equations in isotropic media. *Antennas and Propagation, IEEE Transactions on*, 14 :302–307, 1966.

[28] J. Beeckman, K. Neyts, and P. J. M. Vanbrabant. Liquid-crystal photonic applications. *Opt. Eng.*, 50 :08120217, 2011.

[29] A. Miniewicz, A. Gniewek, and J. Parka. Liquid crystals for photonic applications. *Opt. Mater.*, 21 :605–610, 2003.

[30] A. D. Ford, S. M. Morris, and H. J. Coles. Photonics and lasing in liquid crystals. *Mater. Today*, 9 :36–42, 2006.

[31] E. F. Johnson. Thermodynamics and its applications. *AIChE J.*, 21(1) :203–204, 1975.

[32] Lev M. Blinov. *Structure and Properties of Liquid Crystals.* Springer, 2011.

[33] K. Akagi. Asymmetric polymerization in a chiral liquid crystal reaction field. *Mater. Matters*, 5 :25, 2010.

[34] I. W. Stewart. *The Static and Dynamic Continuum Theory of Liquid Crystals,*. Taylor and Francis, London, 2004.

[35] H. Yokoyama. Surface anchoring of nematic liquid crystals. *Mol. Cryst. Liq. Cryst.*, 165 :265–316, 1988.

[36] A. Nakajima. Design of hydrophobic surfaces for liquid droplet control. *NPG Asia Mater.*, 3 :49–56, 2011.

[37] Introduction to liquid crystals. http://www-g.eng.cam.ac.uk/CMMPE/lcintro2.html, 2007.

[38] A. Yariv. *Quantum Electronics.* 3rd edition. J. Wiley & Sons, NY, 1989.

[39] A. P. Zhao, J. Juntunen, and A. V. Raisanen. An efficient FDTD algorithm for the analysis of microstrip patch antennas printed on a general anisotropic dielectric substrate. *IEEE Trans. Microwave Theory Tech.*, 47 :1142–1146, 1999.

[40] John D. Jackson. *Classical Electrodynamics.* John Wiley & Sons, Inc., 1999.

[41] Stefan Alexandre Maier. *Plasmonics Fundamentals and Applications.* Springer, 2006.

[42] Crai F. Bohren and Donald R. Huffman. *Absorption and scattering of light by small particles.* John Wiley & Sons, Inc., 1983.

[43] Dror Sarid and William Challener. *Modern Introduction to Surface Plasmons Theory, Mathematica Modelling, and Application.* Cambridge University Press, 2011.

[44] P. F. Liao and A. Wokaun. Lightning rod effect in surface enhanced raman scattering. *J. Chem. Phys.*, 76 :751, 1982.

[45] C. Sönnichsen, T. Franzl, T. Wilk, G. von Plessen, J. Feldmann, O. Wilson, and P. Mulvaney. Drastic reduction of plasmon damping in gold nanorods. *Phys. Rev. Lett.*, 88 :077402, 2002.

[46] M. Perner, P. Bost, U. Lemmer, G. von Plessen, J. Feldmann, U. Becker, M. Mennig, M. Schmitt, and H. Schmidt. Optically induced damping of the surface plasmon resonance in gold colloids. *Phys. Rev. Lett.*, 78 :2192–2195, Mar 1997.

[47] T. Kokkinakis and K. Alexopoulos. Observation of radiative decay of surface plasmons in small silver particles. *Phys. Rev. Lett.*, 28 :1632–1634, 1972.

[48] A. Wokaun, J. P. Gordon, and P. F. Liao. Radiation damping in surface-enhanced raman scattering. *Phys. Rev. Lett.*, 48 :957–960, 1982.

[49] E. J. Heilweil and R. M. Hochstrasser. Nonlinear spectroscopy and picosecond transient grating study of colloidal gold. *J. Chem. Phys.*, 82 :4762, 1985.

[50] S. Link and M. A. El-Sayed. Shape and size dependence of radiative, nonradiative and photothermal properties of gold nanocrystals. *Int. Reviews in Phys. Chem.*, 19 :409–453, 2000.

[51] S. Link and M. A. El-Sayed. Spectral properties and relaxation dynamics of surface plasmon electronic oscillations in gold and silver nanodots and nanorods. *J. Phys. Chem. B*, 103 :8410–8426, 1999.

[52] M. Fleischmann, P. J. Hendra, and A. J. McQuillan. Raman spectra of pyridine adsorbed at a silver electrode. *Chem. Phys. Lett.*, 26 :163, 1974.

[53] M. Moskovits. Surface roughness and the enhanced intensity of raman scattering by molecules adsorbed on metals. *J. Chem. Phys.*, 69 :4159, 1978.

[54] J. Gersten and A. Nitzan. Electromagnetic theory of enhanced raman scattering by molecules adsorbed on rough surfaces. *J. Chem. Phys.*, 73 :3023, 1980.

[55] M. Kerker, D. S. Wang, and H. Chew. Surface enhanced raman scattering (sers) by molecules adsorbed at spherical particles. *Appl. Opt.*, 19 :3373–3388, 1980.

[56] P. F. Liao and M. B. Stern. Surface-enhanced raman scattering on gold and aluminum particle arrays. *Opt. Lett.*, 7 :483–485, 1982.

[57] N. Félidj, J. Aubard, and G. Lévi. Controlling the optical response of regular arrays of gold particles for surface-enhanced raman scattering. *Phys. Rev. B*, 65 :075419, 2002.

[58] G. C. Schatz. Theoretical studies of surface enhanced raman scattering. *Acc. Chem. Res.*, 17 :370–376, 1984.

[59] M. Hu, C. Novo, A. Funston, H. N. Wang, H. Staleva, S. L. Zou, P. Mulvaney, Y. N. Xia, and G. V. Hartland. Dark-field microscopy studies of single metal nanoparticles : understanding the factors that influence the linewidth of the localized surface plasmon resonance. *J. Mater. Chem.*, 18 :1949–1960, 2008.

[60] M. A. Kats, N. F. Yu, P. Genevet, Z. Gaburro, and F. Capasso. Effect of radiation damping on the spectral response of plasmonic components. *Opt. Express*, 19 :2148, 2011.

[61] Y. Li, K. Zhao, H. Sobhani, K. Bao, and P. Nordlander. Geometric dependence of the line width of localized surface plasmon resonances. *J. Phys. Chem. Lett.*, 4 :1352–135, 2013.

[62] C. S. Cheng, Y. Q. Chen, and C. J. Lu. Organic vapour sensing using localized surface plasmon resonance spectrum of metallic nanoparticles self assemble monolayer. *Talanta*, 73 :358–365, 2007.

[63] N. H. Mack, J. W. Wackerly, V. Malyarchuk, J. A. Rogers, J. S. Moore, and R. G. Nuzzo. Optical transduction of chemical forces. *Nano Lett.*, 7 :733–737, 2007.

[64] Y. Choi, Y. Park, T. Kang, and L. P. Lee. Selective and sensitive detection of metal ions by plasmonic resonance energy transfer-based nanospectroscopy. *Nature Nanotech.*, 4 :472, 2009.

[65] S. A. Maier, M. L. Brongersma, P. G. Kik, S. Meltzer, A. A. G. Requicha, and H. A. Atwater. Plasmonics : A route to nanoscale optical devices. *Adv. Mater.*, 13 :1501–1505, 2001.

[66] E. Hutter and J. H. Fendler. Exploitation of localized surface plasmon resonance. *Adv. Mater.*, 16 :1685–1706, 2004.

[67] L. Novotny and B. Hecht. *Principles of Nano-Optics.* Cambridge University Press, 2006.

[68] A. Taflove. Review of the formulation and applications of the finite-difference time-domain method for numerical modeling of electromagnetic wave interactions with arbitrary structures. *Wave Motion*, 10 :547 – 582, 1988.

[69] A. Taflove and S. C. Hagness. *Computational Electrodynamics : The Finite-Difference Time Domain Method.* Artech House, Boston, 3rd edition, 2005.

[70] R. Luebbers, F. P. Hunsberger, K. S. Kunz, R. B. Standler, and M. Schneider. A frequency-dependent finite-difference time-domain formulation for dispersive materials. *IEEE Trans. Electromagn. Compat.*, 32 :222–227, 1990.

[71] R. J. Luebbers, F. Hunsberger, and K. S. Kunz. A frequency-dependent finite-difference time-domain formulation for transient propagation in plasma. *IEEE Trans. Antennas Propag.*, 39(1) :29–34, 1991.

[72] R. M. Joseph, S. C. Hagness, and A. Taflove. Direct time integration of maxwell's equations in linear dispersive media with absorption for scattering and propagation of femtosecond electromagnetic pulses. *Opt. Lett.*, 16 :1412–1414, 1991.

[73] L. J. Nickisch and P. M. Franke. Finite-difference time-domain solution of maxwell's equations for the dispersive ionosphere. *IEEE Trans. Antennas Propag.*, 34 :33–39, 1992.

[74] M. A. Strickel and A. Taflove. Time-domain synthesis of broad-band absorptive coatings for two-dimensional conducting targets. *IEEE Trans. Antennas Propag.*, 38 :1084–1091, 1990.

[75] B. Beker, K. R. Umashankar, and A. Taflove. Numerical analysis and validation of the combined field surface integral equations for electromagnetic scattering by arbitrary shaped two-dimensional anisotropic objects. *IEEE Trans. Antennas Propag.*, 37(12) :1573–1581, 1989.

[76] G. Mur. Absorbing boundary conditions for the finite-difference approximation of the time-domain electromagnetic-field equations. *IEEE Trans. Electromagn. Compat.*, EMC-23 :377–382, 1981.

[77] J. P. Bérenger. A perfectly matched layer for the absorption of electromagnetic waves. *J. Comput. Phys.*, 114 :185–200, 1994.

[78] S. D. Gedney. An anisotropic perfectly matched layer-absorbing medium for the truncation of FDTD lattices. *IEEE Trans. Antennas Propag.*, 44 :1630–1639, 1996.

[79] Z. S. Sacks, D. M. Kingsland, R. Lee, and J. F. Lee. A perfectly matched anisotropic absorber for use as an absorbing boundary condition. *IEEE Trans. Antennas Propag.*, 43 :1460–1463, 1995.

[80] J. A. Roden and S. D. Gedney. Convolution PML (CPML) : An efficient FDTD implementation of the CFS-PML for arbitrary media. *Microwave Opt. Technol. Lett.*, 27 :334–339, 2000.

[81] A. P. Zhao and A. V. Raisanen. Application of a simple and efficient source excitation technique to the fdtd analysis of waveguide and microstrip circuits. *IEEE Trans. Microwave Theory Tech.*, 44 :1535–1539, 1996.

[82] J. A. Pereda, L. A. Vielva, M. A. Solano, A. Vegas, and A. Prieto. Fdtd analysis of magnetized ferrites : Application to the calculation of dispersion characteristics of ferrite-loaded waveguides. *IEEE Trans. Microwave Theory Tech.*, 43 :350–357, 1995.

[83] A. Taflove and M. E. Brodwin. Numerical solution of steady-state electromagnetic scattering problems using the time-dependent maxwell's equations. *Microwave Theory and Techniques, IEEE Transactions on*, 23 :623–630, 1975.

[84] W. C. Chew and W. H. Weedon. A 3D perfectly matched medium from modified Maxwell's equations with stretched coordinates. *Microwave Opt. Technol. Lett.*, 7 :599–604, 1994.

[85] M. Kuzuoglu and R. Mittra. Frequency dependence of the constitutive parameters of causal perfectly matched anisotropic absorbers. *IEEE Microwave Guided Wave Lett.*, 6 :447–449, 1996.

[86] H. Schwefel. *Evolution and optimum seeking.* Wiley, 1995.

[87] T. Back. *Evolutionary algorithms in theory and practice.* Oxford University Press, 1996.

[88] R. Luebbers, D. Steich, and K. Kunz. FDTD calculation of scattering from frequency-dependent materials. *IEEE Trans. Antennas Propag.*, 41 :1249–1257, 1993.

[89] R. J. Luebbers and F. Hunsberger. FDTD for nth-order dispersive media. *IEEE Trans. Antennas Propag.*, 40 :1297–1301, 1992.

[90] D. F. Kelley and R. J. Luebbers. Piecewise linear recursive convolution for dispersive media using FDTD. *IEEE Trans. Antennas Propag.*, 44 :792–797, 1996.

[91] D. M. Sullivan. Frequency-dependent FDTD methods using Z transforms. *IEEE Trans. Antennas Propag.*, 40 :1223–1230, 1992.

[92] R. Siushansian and J. LoVetri. A comparison of numerical techniques for modeling electromagnetic dispersive media. *IEEE Microwave Guided Wave Lett.*, 5 :426–428, 1995.

[93] T. O. Körner and W. Fichtner. Auxiliary differential equation : efficient implementation in the finite-difference time-domain method. *Opt. Lett.*, 22 :1586–1588, Nov 1997.

[94] P. G. Etchegoin, E. C. Le Ru, and M. Meyer. An analytic model for the optical properties of gold. *J. Chem. Phys.*, 125 :164705, 2006.

[95] A. Vial and T. Laroche. Description of dispersion properties of metals by means of the critical points model and application to the study of resonant structures using the fdtd method. *J. Phys. D : Appl. Phys.*, 40 :7152, 2007.

[96] S. G. Garcia, T. M. Hung-Bao, R. G. Martin, and B. G. Olmedo. On the application of finite methods in time domain to anisotropic dielectric waveguides. *IEEE Trans. Microwave Theory Tech.*, 44 :2195–2206, 1996.

[97] K. A. Willets and R. P. Van Duyne. Localized surface plasmon resonance spectroscopy and sensing. *Annu. Rev. Phys. Chem.*, 58 :267–297, 2007.

[98] M. I. Stockman. Nanoplasmonics : past, present, and glimpse into future. *Opt. Express*, 19 :151468, 2011.

[99] M. G. Albrecht and J. A. Creighton. Anomalously intense raman spectra of pyridine at a silver electrode. *J. Am. Chem. Soc.*, 99 :5215, 1977.

[100] A. Wokaun. *Solid State Physics.* 38, 223, 1984.

[101] W. H. Park and Z. H. Kim. Charge transfer enhancement in the sers of a single molecule. *Nano Lett.*, 10 :4040–4048, 2010.

[102] J. Ando, K. Fujita, N. I. Smith, and S. Kawata. Dynamic SERS imaging of cellular transport pathways with endocytosed gold nanoparticles. *Nano. Lett.*, 11 :5344–5348, 2011.

[103] S. Nie and S. R. Emory. Probing single molecules and single nanoparticles by surface-enhanced raman scattering. *Science*, 275 :1102, 1997.

[104] D. van Lierop, I. A. Larmour, K. Faulds, and D. Graham. SERS primers and their mode of action for pathogen DNA detection. *Anal. Chem.*, 85 :1408–1414, 2013.

[105] E. J. Titus, M. L. Weber, S. M. Stranahan, and K. A. Willets. Super-resolution SERS imaging beyond the single-molecule limit : An isotope-edited approach. *Nano Lett.*, 12 :5103–5110, 2012.

[106] George C. Schatz and Richard P. Van Duyne. *Electromagnetic Mechanism of Surface-Enhanced Spectroscopy.* John Wiley & Sons Ltd, 2002.

[107] G. C. Schatz, M. A. Young, and R. P. Van Duyne. Electromagnetic mechanism of sers. In *Surface-Enhanced Raman Scattering*, volume 103 of *Topics in Applied Physics*, pages 19–45. Springer, 2006.

[108] N. Valley, N. Greeneltch, R. P. Van Duyne, and G. C. Schatz. A look at the origin and magnitude of the chemical contribution to the enhancement mechanism of surface-enhanced raman spectroscopy(sers) : Theory and experiment. *J. Phy. Chem. Lett.*, 4 :2599–2604, 2013.

[109] T. Y. Jeon, S. G. Park, S. Y. Lee, H. C. Jeon, and S. M. Yang. Shape control of Ag nanostructures for practical SERS substrates. *ACS Appl. Mater. Interfaces*, 5 :243–248, 2013.

[110] N. G. Greeneltch, M. G. Blaber, A. I. Henry, G. C. Schatz, and R. P. Van Duyne. Immobilized nanorod assemblies : Fabrication and understanding of large area surface-enhanced raman spectroscopy substrates. *Anal. Chem.*, 85 :2297–2303, 2013.

[111] B. Yan, A. Thubagere, W. R. Premasiri, L. D. Ziegler, L. Dal Negro, and B. M. Reinhard. Engineered SERS substrates with multiscale signal enhancement : Nanoparticle cluster arrays. *ACS Nano*, 3 :1190–1202, 2009.

[112] J. Ye, F. F Wen, H. Sobhani, J. B. Lassiter, P. Van Dorpe, P. Nordlander, and N. J. Halas. Plasmonic nanoclusters : Near field properties of the fano resonance interrogated with SERS. *Nano Lett.*, 12 :1660–1667, 2012.

[113] P. K. Jain, K. S. Lee, I. H. El-Sayed, and M. A. El-Sayed. Calculated absorption and scattering properties of gold nanoparticles of different size shape and composition : applications in biological imaging and biomedicine. *J. Phys. Chem. B*, 110 :7238–48, 2006.

[114] C. Langhammer, Z. Yuan, I. Zorić, and B. Kasemo. Plasmonic properties of supported Pt and Pd nanostructures. *Nano Lett.*, 6 :833–838, 2006.

[115] P. K. Jain and M. A. El-Sayed. Noble metal nanoparticle pairs : effect of medium for enhanced nanosensing. *Nano Lett.*, 8 :4347–4352, 2008.

[116] A. J. Haes and R. P. Van Duyne. A nanoscale optical biosensor : sensitivity and selectivity of an approach based on the localized surface plasmon resonance spectroscopy of triangular silver nanoparticles. *J. Am. Chem. Soc.*, 124 :10596–10604, 2002.

[117] Y. J. Liu, E. S. P. Leong, B. Wang, and J. H. Teng. Optical transmission enhancement and tuning by overlaying liquid crystals on a gold film with patterned nanoholes. *Plasmonics*, 6 :659–664, 2011.

[118] T. J. Kim, T. Thio, T. W. Ebbesen, D. E. Grupp, and H. J. Lezec. Control of optical transmission through metals perforated with subwavelength hole arrays. *Opt. Lett.*, 24 :256–258, 1999.

[119] W. Dickson, G. A. Wurtz, P. R. Evans, R. J. Pollard, and A. V. Zayats. Electronically controlled surface plasmon dispersion and optical transmission through metallic hole arrays using liquid crystal. *Nano Lett.*, 8 :281–286, 2008.

[120] Y. J. Liu, Y. B. Zheng, J. Liou, I. K. Chiang, I. C. Khoo, and T. J. Huang. All-optical modulation of localized surface plasmon coupling in a hybrid system composed of photoswitchable gratings and Au nanodisk arrays. *J. Phys. Chem. C*, 115 :7717–7722, 2011.

[121] J. Müller, C. Sönnichsen, H. von Poschinger, G. von Plessen, T. A. Klar, and J. Feldmann. Electrically controlled light scattering with single metal nanoparticles. *Appl. Phys. Lett.*, 81 :171–173, 2002.

[122] M. Ojima, N. Numata, Y. Ogawa, K. Murata, H. Kubo, A. Fujii, and M. Ozaki. Electric field tuning of plasmonic absorption of metallic grating with twisted nematic liquid crystal. *Appl. Phys. Express*, 2 :086001, 2009.

[123] K. C. Chu, C. Y. Chao, Y. F. Chen, Y. C. Wu, and C. C. Chen. Electrically controlled surface plasmon resonance frequency of gold nanorods. *Appl. Phys. Lett.*, 89 :103107, 2006.

[124] P. R. Evans, G. A. Wurtz, W. R. Hendren, R. Atkinson, W. Dickson, A. V. Zayats, and R. J. Pollard. Electrically switchable nonreciprocal transmission of plasmonic nanorods with liquid crystal. *Appl. Phys. Lett.*, 91 :043101, 2007.

[125] P. A. Kossyrev, A. J. Yin, S. G. Cloutier, D. A. Cardimona, D. H Huang, P. M. Alsing, and J. M. Xu. Electric field tuning of plasmonic response of nanodot array in liquid crystal matrix. *Nano lett.*, 5 :1978–1981, 2005.

[126] V. K. S. Hsiao, Y. B. Zheng, B. K. Juluri, and T. J. Huang. Light-driven plasmonic switches based on au nanodisk arrays and photoresponsive liquid crystals. *Adv. Mater.*, 20 :3528–3532, 2008.

[127] J. Berthelot, A. Bouhelier, C. J. Huang, J. Margueritat, G. Colas-des Francs, E. Finot, J. C. Weeber, A. Dereux, S. Kostcheev, H. I. E. Ahrach, A. L. Baudrion, J. Plain, R. Bachelot, P. Royer, and G. P. Wiederrecht. Tuning of an optical dimer nanoantenna by electrically controlling its load impedance. *Nano lett.*, 9 :3914–3921, 2009.

[128] M. Dridi and A. Vial. Modeling of metallic nanostructures embedded in liquid crystals : application to the tuning of their plasmon resonance. *Opt. Lett.*, 34 :2652–2654, 2009.

[129] M. Dridi and A. Vial. FDTD modelling of gold nanoparticle pairs in a nematic liquid crystal cell. *J. Phys. D : Appl. Phys.*, 43 :415102, 2010.

[130] M. Dridi and A. Vial. FDTD modeling of gold nanoparticles in a nematic liquid crystal : Quantitative and qualitative analysis of the spectral tunability. *J. Phys. Chem. C*, 114(21) :9541–9545, 2010.

[131] J. Li, Y. Ma, Y. Gu, I. C. Khoo, and Q. H. Gong. Large spectral tunability of narrow geometric resonances of periodic arrays of metallic nanoparticles in a nematic liquid crystal. *Appl. Phys. Lett.*, 98 :213101, 2011.

[132] E. Spinozzi and A. Ciattoni. Ultrathin optical switch based on a liquid crystal/silver nanoparticles mixture as a tunable indefinite medium. *Opt. Mater. Express*, 1 :732–741, 2011.

[133] A. Vial. Implementation of the critical points model in the recursive convolution method for dispersive media modeling with the FDTD methods. *J. Opt. A : Pure Appl. Opt.*, 9 :745–748, 2007.

[134] T. Rindzevicius, Y. Alaverdyan, and M. Kall. Long-range refractive index sensing using plasmonic nanostructures. *J. Phys. Chem. C*, 111 :11806–11810, 2007.

[135] L. J. Sherry, S. H. Chang, G. C. Schatz, R. P. Van Duyne, B. J. Wiley, and Y. N. Xia. Localized surface plasmon resonance spectroscopy of single silver nanocubes. *Nano Lett.*, 5 :2034–2038, 2005.

[136] T. R. Jensen, M. D. Malinsky, C. L. Haynes, and R. P. Van Duyne. Nanosphere lithography : Tunable localized surface plasmon resonance spectra of silver nanoparticles. *Phys. Chem. B*, 104 :10549–10556, 2000.

[137] R. C. Jin, Y. W. Cao, C. A. Mirkin, K. L. Kelly, G. C. Schatz, and J. G. Zheng. Photoinduced conversion of silver nanospheres to nanoprisms. *Science*, 294 :1901–1903, 2001.

[138] N. J. Halas, S. Lal, S. Link, W. S. Chang, D. Natelson, J. H. Hafner, and P. Nordlander. A plethora of plasmonics from the laboratory for nanophotonics at rice university. *Adv. Mater.*, 24 :4842–4877, 2012.

[139] H. Wang and A. Vial. Theoretical study of the anchoring influence on plasmonic resonance tunability of metallic nanoparticles embedded in a liquid crystal cell. *Plasmonics*, 8 :1335–1339, 2013.

[140] M. G. Banaee and K. B. Crozier. Mixed dimer double-resonance substrates for surface-enhanced raman spectroscopy. *ACS Nano*, 5 :307–314, 2011.

[141] J. Ye and P. Van Dorpe. Nanocrosses with highly tunable double resonances for near-infrared surface-enhanced raman scattering. *international journal of optics*, 2012 :745982, 2012.

[142] Y. Chu and K. B. Crozier. Experimental study of the interaction between localized and propagating surface plasmons. *Opt. Lett.*, 34 :244–246, 2009.

[143] Y. Chu, M. G. Banaee, and K. B. Crozier. Double-resonance plasmon substrates for surface-enhanced raman scattering with enhancement at excitation and stokes frequencies. *ACS Nano*, 4 :2804–2810, 2010.

[144] I. Abdulhalim. Surface plasmon te and tm waves at the anisotropic film-metal interface. *J. Opt. A : Pure Appl. Opt.*, 11 :015002, 2009.

[145] Jin Au Kong. *Electromagnetic wave theory.* EMW Publishing Cambridge, Massachusetts, USA, 2008.

[146] A. S. Grimault, A. Vial, and M. Lamy de la Chapelle. Modeling of regular gold nanostructures arrays for sers applications using a 3D FDTD method. *Appl. Phys. B-Lasers Opt.*, 84 :111–115, 2006.

[147] H. Wang and A. Vial. Plasmonic resonance tunability and surface-enhanced raman scattering gain of metallic nanoparticles embedded in a liquid crystal cell. *J. Phys. Chem. C*, 117 :24537–24542, 2013.

[148] T. V. Teperik, P. Nordlander, J. Aizpurua, and A. G. Borisov. Quantum effects and nonlocality in strongly coupled plasmonic nanowire dimers. *Opt. Express*, 21 :27306–27325, 2013.

[149] J. Zuloaga, E. Prodan, and P. Nordlander. Quantum description of the plasmon resonances of a nanoparticle dimer. *Nano Lett.*, 9 :887–891, 2009. PMID : 19159319.

[150] R. Esteban, A. G. Borisov, P. Nordlander, and J. Aizpurua. Bridging quantum and classical plasmonics with a quantum-corrected model. *Nat. Commun.*, 3 :825, 2012.

[151] S. Thongrattanasiri, A. Manjavacas, P. Nordlander, and F. Javier García de Abajo. Quantum junction plasmons in graphene dimers. *Laser Photonics Rev.*, 7 :297, 2013.

[152] V. Kulkarni, E. Prodan, and P. Nordlander. Quantum plasmonics : Optical properties of a nanomatryushka. *Nano Lett.*

Huan WANG

Doctorat : Optique et Nanotechnologies

Année 2014

Modélisation de l'accordabilité de la résonance plasmon de particules métalliques par des cristaux liquides

Les nanoparticules métalliques ont des propriétés optiques uniques, dont le contrôle et l'optimisation ont un intérêt grandissant tant pour la recherche fondamentale qu'appliquée. Une propriété spectaculaire de ces nanoparticules est la résonance plasmon de surface localisé, qui est une conséquence des oscillations des électrons libres à l'interface métal/diélectrique.
La position spectrale de la résonance plasmon est largement dépendante de la géométrie des nanoparticules, mais aussi de la constante diélectrique du milieu environnant. Un moyen pour contrôler cette résonance consiste donc à faire varier l'indice du milieu qui entoure les nanostructures. Les cristaux liquides nématiques sont un excellent moyen pour modifier et contrôler la résonance plasmon. En effet, par rotation des molécules du cristal liquide on peut induire un changement d'indice qui se traduit par un changement de la réponse optique des nanostructures. L'objectif de la thèse est de simuler des réseaux de nanoparticules d'or, dans un cristal liquide nématique afin de prédire l'influence de l'orientation du CL sur les propriétés optiques de ces nanostructures. Le formalisme numérique utilisé est basé sur la méthode des différences finies dans le domaine temporel (FDTD). Nous avons pris en compte les phénomènes d'ancrage des molécules aux interfaces avec la cellule contenant les cristaux liquides et les structures métalliques, et comparé les résultats avec le cas d'une orientation uniforme des molécules dans la cellule. La possibilité d'avoir une double résonance a été étudiée, ainsi que les gain SERS associés à ces structures spécifiques.

Mots clés : cristaux liquides - différences finies - nanoparticules - plasmons.

Modeling of the Plasmon Resonance of Metallic Nanopaticles Embedded in Liquid Crystal

Metal nanoparticles have unique optical properties, the control and optimization have a growing interest in fundamental research as same as applied research. A spectacular property of these nanoparticles is the localized surface plasmon resonance (LSPR), which is a consequence of the oscillations of free electrons at the interface between metal and dielectric.
The spectral position of the plasmon resonance is largely dependent on the geometry of the nanoparticles, but also on the dielectric properties of the surrounding medium. It implies that the variation of the index of the medium surrounding the metallic nanostructures can control the LSPR resonance. Nematic liquid crystals are a great way to modify and control the plasmon resonance. Indeed, rotation of the liquid crystal molecules can induce a change in refractive index which results in a change in the optical response of the nanostructures. The aim of the thesis is to simulate arrays of gold nanoparticles in a nematic liquid crystal in order to predict the influence of the orientation of the LC molcules on the optical properties of these nanostructures. Numerical method we used is based on the finite difference time domain (FDTD) method. We have considered anchoring effects of molecules at the interfaces between the cell containing the liquid crystal and the substrates. And the results are compared with the case of uniform orientation of the LC molecules in the cell. The possibility of having double resonances was studied as well as the Surface Enhanced Raman Scattering (SERS) gain associated with these specific structures.

Keywords: liquid crystals - finite differences - nanoparticles – plasmons (physics).

Thèse réalisée en partenariat entre :

utt
université de technologie
Troyes

Ecole Doctorale "Sciences et Technologies"